THE PROPERTIES OF STAR-FORMING GALAXIES IN THE PROTO-CLUSTER ENVIRONMENT AT $Z \sim 2$

A Dissertation

by

LEO YVONNE ALCORN

Submitted to the Office of Graduate and Professional Studies of
Texas A&M University
in partial fulfillment of the requirements for the degree of

DOCTOR OF PHILOSOPHY

Chair of Committee,	Kim-Vy Tran
Committee Members,	Casey Papovich
	Louis Strigari
	Jianhua Huang
Head of Department,	Grigory Rogachev

May 2019

Major Subject: Astronomy

ABSTRACT

Galaxy clusters are regions of the universe which host extreme gas physics, and allow us to probe fundamental physical properties such as dark matter, structure formation, and baryonic properties. In the local universe, galaxy clusters host a population of galaxies distinct from isolated galaxies. They tend to consist of galaxies with quenched or low star formation, older stellar populations, low gas fractions, higher levels of velocity dispersion, and elliptical shapes. In less dense areas of the universe, the fraction of galaxies with ordered rotation, higher star formation, disky morphology, and high gas fractions increases. At $z \sim 2$, galaxies in clusters and proto-clusters are still at a stage of rapid star formation and are not yet quenched. We observe two galaxy proto-clusters at $z = 1.62$ and $z = 2.095$ to measure the kinematic and nebular gas properties of galaxies in these forming clusters.

We perform a kinematic and morphological analysis of star-forming galaxies at $z \sim 2$ in the COSMOS legacy field using near-infrared spectroscopy from Keck/MOSFIRE and F160W imaging from CANDELS/3D-HST. Our sample consists of cluster and field galaxies from $2.0 < z < 2.5$ with K band multi- object slit spectroscopic measurements of their Hα emission lines. We measure Hα emission-line integrated velocity dispersions (σ_{int}) from $50 - 230$ km s^{-1}, and from these data we estimate virial, stellar, and gas masses and derive correlations between these properties for cluster and field galaxies at $z \sim 2$. We find evidence that baryons (gas and stars) dominate the mass within the central effective radius. However, we find no statistically significant differences between the cluster and the field, and conclude that the kinematics of star-forming galaxies at $z \sim 2$ are not significantly different between the cluster and field environments. Hα rotational velocities and gas velocity dispersions are measured using the Heidelberg Emission Line Algorithm (HELA), which compares directly to simulated 3D data-cubes. We examine the role of regular and irregular morphology in the stellar mass kinematic scaling relations, deriving the kinematic measurement S$_{0.5}$, and finding log(S$_{0.5}$) = (0.38 ± 0.07) $\log$(M$_\star$/M$_\odot$- 10) + (2.04 ± 0.03) with no significant offset between morphological populations and similar levels of scatter (~ 0.16 dex). We estimate the specific angular momenta (j_{disk}) of these galaxies and find a slope of 0.36 ± 0.12, shallower than predicted without mass-dependent disk growth, but this result is possibly due to measurement uncertainty at $M_{\star} < 9.5$. However, through a K-S test we find irregular galaxies to have marginally higher j_{disk} values than regular galaxies, and high scatter at low masses in both populations.

We measure the properties of ionized regions in galaxies in the UDS and COSMOS proto-clusters by measuring fluxes from emission lines Hβ 4861Å, [O III] 5007Å, Hα 6563Å, [N II] 6585Å, and [S II] 6716,6731Å. We measure gas-phase metallicity of both proto-clusters using two metallicity indicators, including an indicator independent of ionization parameter and electron density, finding that cluster and field galaxies in both UDS and COSMOS lie on the same Mass-Metallicity Relation. We find tentative evidence ($\sim 2\sigma$) that galaxies in clusters have lower [O III]/Hβ ratios (~ 0.2 dex) relative to the field. However, we are limited by small numbers in the clusters and contamination by sky lines in measuring Hβ. Results indicate that galaxies in proto-clusters have lower ionization parameter than field galaxies at similar redshift and stellar mass, possibly due to the development of the hot intracluster medium.

DEDICATION

This work is dedicated to the many who have helped me along the way, the giants whose shoulders I stand upon.

So mysterious is your world
Concealed beyond the stars
Far away from the earth
It flows one with time and dark as the night
Million shapes and colours
Are storming inside your mind
Creating endless dimensions
Forming universes without walls

Excerpt from ***Starchild*** by Wintersun, self-titled

You're like a fart on the high wind, and nobody's sniffin'. - Colin Witucki,
On Mankind's Place in the Universe, December 29th, 2018.

ACKNOWLEDGMENTS

I would like to thank my family. My parents, Mark Alcorn and Karen Luke, my friend Samuel Seydel, and my grandparents, who are directly responsible for the fortunate circumstances I was given. And my cousin, Prof. Wes Petersen, who encouraged me in physics when I was young.

There were many who helped me as a young scientist. J. Anthony Tyson, Pat Boeshaar, David Wittman, Chris Fassnacht, and Lori Lubin educated me at U.C. Davis and gave me my first tastes of research and opened many doors for me.

At Texas A&M, I would like to thank all the astronomy faculty and staff, who as a team built me into a greater scientist. Thank you to Casey Papovich, Nick Suntzeff, Jonelle Walsh, Louis Strigari, Lucas Macri, Darren Depoy, Jennifer Marshall, Lifan Wang, Kevin Krisciunas, and Don Carona.

My great thanks to my collaborators in ZFIRE, ZFOURGE, and the W. M. Keck Observatory, particularly Karl Glazebrook, Glenn Kaczprak, Tiantian Yuan, Caroline Straatman, Josh Walawender, Luca Rizzi, and Greg Doppman. Above all, I have great gratitude for my PhD supervisor, Prof. Kim-Vy Tran, who challenged me and built me up. You have supported me at every step, pushed me to face my fears, and made me into something I never thought I could be.

The graduate students and postdoctoral researchers of Texas A&M have been a loving and supportive group. To Jimmy, Brett, Adam, Heath, Ryan O., Mike, Yi, Nancy, Ting, Ryan Q., Andrew Q., Wenlong, Steven, Dan, Ben, Katelyn, Peachy, Vince, Fergie, Sarah, John, Taylor, Sijie, Andrew P., Tarini, Jaqueline, Lexi, Jaiwen, Lauren, Yaswant, Claire, Terese, Peter, and Ben B., I thank you. I would like to acknowledge the camaraderie of the LSST Data Science Fellowship instructors (Adam Miller and Lucianne Walkowicz) and fellows. The LSSTC DSFP taught me valuable data science skills I have used in my research, and will use and teach for the rest of my life.

Thank you to my friends in Bryan, the Dirtbag punks at Revolution. You helped me maintain balance and welcomed me as one of your own for these six years. Thank you to my partners James and Ian for your love, patience, and support.

When things were hard, my cats Eris, Vega, and Andromeda have helped me through it. I will love you forever. I would also like to thank the bands Wintersun, Behemoth, Mastodon, Kylesa, Black Sabbath, Gloryhammer, Anaal Nathrakh, Ghost, ASS, and Pyreship for being my power tunes at my best and worst times.

I thank the indigenous and resident people of Hawaii, my gracious hosts for the observations which have provided the data used in this thesis. Additionally, I thank Mauna Kea herself for serving as site for the Keck Observatory. I thank the old gods and spirits of the natural world for being my original inspiration to study the Universe.

The data reduction performed to obtain our results was done on the Brazos cluster at Texas A&M university. I would especially like to thank the Mitchell family for their continuing support and in particular the late George P. Mitchell whose vision and commitment to science and astronomy leaves a lasting legacy.

CONTRIBUTORS AND FUNDING SOURCES

Contributors

This work was supported by a dissertation committee consisting of Professor Kim-Vy Tran, Professor Casey Papovich, and Professor Louis Strigari of the Department of Physics and Astronomy and Professor Jianhua Huang of the Department of Statistics.

The data analyzed for Chapters 2, 3, and 4 was provided by CANDELS, ZFOURGE, ZFIRE, and 3D-HST.

All other work conducted for the thesis (or) dissertation was completed by the student independently.

Funding Sources

Graduate study was supported by a grant from the National Science Foundation and the George and Cynthia Mitchell Institute.

NOMENCLATURE

SFG	Star-Forming Galaxy
ICM	Intra-Cluster Medium
”	Arcsecond
Å	Angstroms
AGN	Active Galactic Nucleus/Nuclei
BCG	Brightest Cluster Galaxy
ΛCDM	Dark Energy and Cold Dark Matter
BPT	Baldwin, Phillips, Terlevich Diagram
HI	Neutral Hydrogen
HII	Ionized Hydrogen
ISM	Interstellar Medium
MCMC	Monte Carlo Markov Chain
HELA	Heidelberg Emission-Line Algorithm
FWHM	Full Width at Half Maximum
PSF	Point-Spread Function
HST	Hubble Space Telescope
IFU	Integral Field Unit
TFR	Tully-Fisher Relation
NIR	Near-InfraRed
CMB	Cosmic Microwave Background
MZR	Mass-Metallicity Relation

TABLE OF CONTENTS

LIST OF FIGURES

FIGURE Page

LIST OF TABLES

1. INTRODUCTION AND LITERATURE REVIEW

1.1 The Cosmological Context and ΛCDM

The current cosmological paradigm is Λ Cold Dark Matter, or ΛCDM. This model of our universe states that vacuum energy, represented Λ in cosmological equations of state, is the dominant energy in the local universe. According to recent Planck observations, Λ is estimated to make up 73% of the universe (Planck Collaboration et al., 2018). The dominant form of matter is Cold Dark Matter, cold meaning non-relativistic. Dark matter, which interacts gravitationally with itself and baryonic (atomic) matter but not electromagnetically, has been observed indirectly in multiple contexts, but no dark matter particle has been identified. Dark matter is likely to be non-relativistic based on simulations of cold, warm, and hot dark matter, which predicted that cold dark matter would form the structure of the Cosmic Web similar to what astronomers observe. Matter is estimated to make up 27% of the universe, but baryonic matter is estimated to make up only 4% of the universe. Baryonic matter is the only form of matter that can be directly observed by astronomers given current instrumentation. While this work concerns itself with baryonic matter and baryonic physical processes, our observations add important constraints on the fundamental properties of the rest of the universe.

The universe is currently estimated to be 13.7 billion years old. The Cosmic Microwave Background (CMB) is observational evidence of a period of rapid universal expansion, known colloquially (and originally, disparagingly) as the "Big Bang Theory". While the universe expanded over a period of $\sim$380,000 years, the universe was an opaque hydrogen plasma, where the mean free path of a photon was so small that we are unable to observe photons from this period. As the universe expanded, the temperature dropped, and at this 380,000 year mark (called the *epoch of recombination*), neutral hydrogen could form. The neutral hydrogen could not absorb these photons, and the universe became transparent. The

CMB is the surface of last scattering of primordial photons, and can be used to map temperature and density of the universe at this time.

The CMB is remarkably *homogeneous* (the average density is the same at all places) and *isotropic* (there is no preferred orientation). Temperature differences are on the order of 10^{-6} Kelvin (from the average temperature of 2.7 Kelvin), but these small deviations in temperature provide the first observations of the seeds of cosmic structure (See Figure 1.1). Denser regions of neutral hydrogen, which appear in the CMB, gravitationally accrete more matter. Dark matter and baryonic matter collapse onto these denser regions and form the first stars, galaxies, and galaxy clusters.

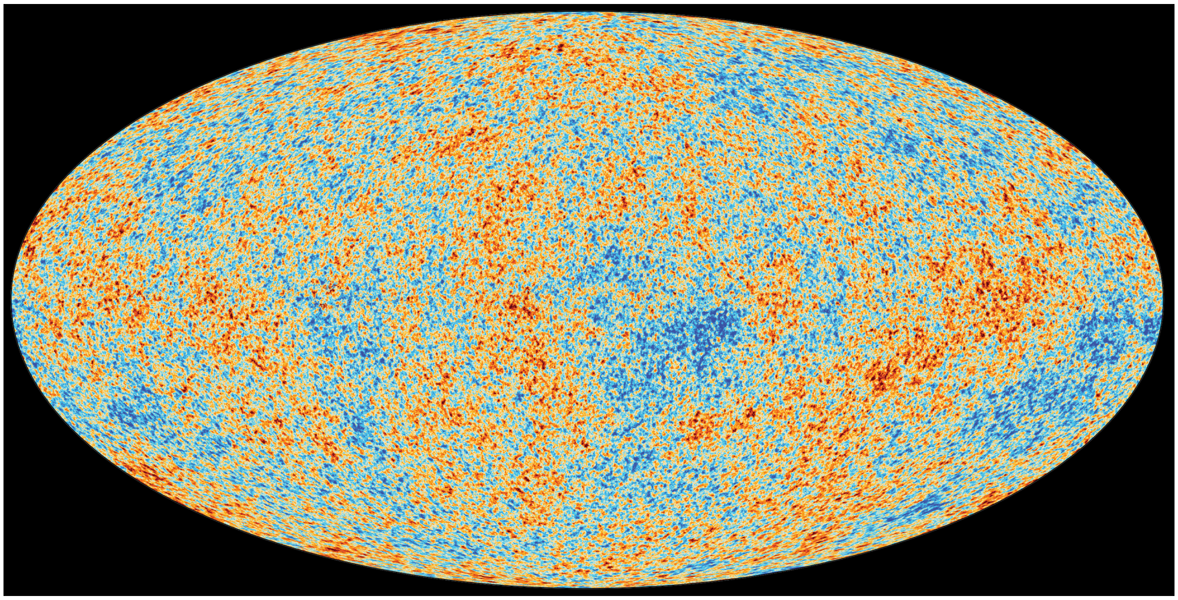

Figure 1.1: The Cosmic Microwave Background as observed by the Planck satellite. Despite the appearance in this image, the CMB is remarkably consistent, and the temperature difference is only on the scale of 10^{-6} Kelvin. The temperature variations are indications of density variations in the early universe. Image by Planck/ESA.

As galaxies form, they re-ionize the hydrogen gas in the universe (the methods by which are still a very active area of research, but will not be the subject of this work). This results in the epoch of $reionization$, and one method of causing this ionization is from the high flux of ionizing photons produced by rapid star formation. Star formation continues to increase globally until the star-formation rate density peaks at $z \sim 2$ (Madau and Dickinson, 2014).

1.2 A History of Galaxy Properties Over Cosmic Time

Here we introduce the subjects of this thesis: galaxies. Galaxies are defined as collections of stars, gas, dust, and dark matter. What differentiates them from stellar clusters (open or globular) is the significant presence of dark matter. Galaxies form in a variety of morphologies, merger and star formation histories, and environments. The history of individual galaxies, as such, are varied and there is no one preferred mode of galaxy evolution. Even galaxies of similar morphologies and physical properties can be formed from a variety of evolutionary paths (Wellons et al., 2016).

In order to determine the dominant factors in galaxy evolution and the particular situations they apply to, there are two major modes of study. First is to simulate galaxies given our current knowledge of physics. This method's strength is in its ability to track precise and specific evolutionary paths of individual galaxies, galaxy clusters, and galaxy properties. Simulations can vary from dark matter only simulations (for cosmological structure formation, like Aquarius) to hydrodynamical simulations (IllustrisTNG, EAGLE, FIRE). Some challenges of this method are due to the vast amount of computing time and power necessary in these projects, and issues involving sub-grid models of stellar, active galactic nuclei (AGN), and supernovae feedback (as these processes are still not well understood). The second method (and the method used in this thesis) is by observing a variety of galaxies and their physical properties, over cosmic time (from local galaxies to the current search for the first galaxies). Then, we compare galaxy properties to local galaxies and infer evolutionary paths. The individual evolutionary paths of galaxies cannot be measured outside of simulations, but overall trends and scaling relations can be observed and matched to different stages in the universe.

Here, we review galaxy and galaxy cluster properties in the local universe, and introduce the properties of their higher-redshift progenitors.

1.2.1 Local Galaxies and Galaxy Clusters

Galaxies in the local universe show diverse characteristics, indicating a variety of formation and evolution mechanisms. The earliest classification of galaxy characteristics was the Hubble Tuning Fork, a proposed explanation for the variety of galaxy morphologies (Hubble, 1927). The fork consists of elliptical and lenticular galaxies at its base, and spiral galaxies with and without barred centers on its tines. Irregular galaxies that do not fit into either category are outside this model. It was originally predicted through this model that elliptical and lenticular galaxies (deemed "early-type" galaxies) evolved into the more complex spiral galaxies (termed "late-type" galaxies). However, current observations and simulations do not confirm this model. Instead, elliptical galaxies are the oldest and most evolved population of galaxies.

Recent observations instead show a more complex set of physical phenomena in these galaxies that provides clues to their evolutionary paths. Elliptical galaxies have spherical morphologies, dispersion-dominated dynamics, older stellar populations, and lower gas content. They also display lower star-formation rates (SFRs) in the local universe. These properties indicate earlier epochs of star formation. Spiral and lenticular galaxies (referred to as disk galaxies in this work) have flattened structures, more ordered rotation support and low levels of dispersion. These galaxies typically have higher gas fractions, younger stellar populations, and higher ongoing star-formation.

A fundamental physical property of galaxies are their internal kinematics. Kinematics can include rotation (often seen as v or V in texts), or ordered motion, and velocity dispersion (seen as σ in literature), or random motions. Kinematics are used as tracers of gravitational potential or mass internal to orbit using the Virial Theorem. One example of this is the Tully-Fisher Relation (TFR) (Tully and Fisher, 1977), which was a relationship between the HI rotation curve of a galaxy and its absolute magnitude. It was originally used as a distance measurement, but more recently it is a tracer of dynamical mass in its form as the stellar-mass Tully-Fisher Relation. This modification instead is a relationship between rotational velocity and stellar mass. Additionally the rotational velocity can often be measured using the bright Hα emission line, which is emitted from the birth clouds that surround young O-type stars. In star-forming galaxies, the Hα flux can be used to estimate the instantaneous star-formation rate (Kennicutt, 1998).

The Cosmic Web is a poetic name for the large scale structure of the universe, consisting of galaxy clusters, filaments, and voids. Galaxy clusters are the hubs of the Cosmic Web, formed from gravitationally bound groups of galaxies connected by filaments of gas and small galaxy groups (of 2 - 6 members). The Milky Way and Andromeda are not members of galaxy clusters, but are in a small galaxy group called "The Local Group". Galaxy clusters are giant physics laboratories, allowing astronomers to probe extreme processes involving gas interactions, dark matter physics, and hierarchical formation. In the local universe, the dense environments of galaxy clusters have distinct galaxy populations characterized by environmental effects on their evolution. A hot blanket of ionized hydrogen gas (the Intracluster Medium, or ICM) enfolds galaxies and glows with X-ray light, composed of gas stripped from in-falling galaxies (Reiprich and Böhringer, 2002).

In the local universe, the properties of galaxies such as their star formation rate (Lewis et al., 2002; Grootes et al., 2017; Jarrett et al., 2017), metal content (Cooper et al., 2008; Ellison et al., 2009), morphology (Houghton, 2015), stellar mass function (Papovich et al., 2012), and internal dynamics (Cappellari et al., 2011) are correlated with their environmental density. Galaxies in the cluster environment contain older stellar populations, as the gas that forms new stars has been stripped from them (Muzzin et al., 2014; Ebeling et al., 2014) or the accretion of gas from the surrounding environment has been cut off (van de Voort et al., 2017). Cluster galaxies can become massive due to the increased number of interactions between them (Lotz et al., 2013), merging together to form huge galaxies with chaotic internal motions (Cappellari et al., 2011).

Because local galaxy clusters contain members with older stellar populations and lower SFRs, it is difficult to directly compare the properties of their constituent galaxies with isolated galaxies. The spectra of rapidly star-forming galaxies (SFGs) contains nebular emission lines. These emission lines are emitted from the ionized Hydrogen gas that surrounds young O-type stars, which live for a period of only 10 million years. Thus, galaxies without ongoing star formation do not show strong emission lines, making it difficult to use these lines to directly compare internal dynamics and ionized gas properties.

1.2.2 High z Galaxies and Proto-Clusters

As astronomers observe more distant galaxies, the light emitted from them takes more time to reach our instruments. Thus, when we observe distant galaxies, we look into the history of the universe. Due to the expansion of the universe, the light emitted from distant galaxies is redshifted, or, the wavelength of the light is lengthened. Redshift, or z, is then a shorthand way to refer to the age of the universe. Redshift zero or $z = 0$, is the local universe, or the universe at 13.8 billion years old. However, of particular interest to this work, and to astronomers in galaxy evolution studies, are $1 < z < 4$ or the universe from $1.56 - 5.9$ billion years old, which is a period of rapid star formation in all galaxy populations.

The peak of cosmic star formation was at $z \sim 2$, the universe at ~3 billion years old (Madau and Dickinson, 2014). Galaxies in proto-clusters, even the brightest cluster galaxies which are typically quiescent in the local universe, were forming stars at rates similar to isolated galaxies (Tran et al., 2010). However, these dense environments were not dynamically relaxed, and instead were still in the process of merging groups. Hence we refer to dense environments as over-densities or proto-clusters, because galaxy clusters are dynamically relaxed systems with an X-ray emission component. The star formation seen in proto-clusters conveniently allows astronomers to perform direct comparisons between cluster and isolated galaxies at this redshift, unlike at local redshifts where cluster galaxies are unlikely to have nebular emission lines.

Galaxy properties at the epoch of rapid star formation had different physical properties from local galaxies. See Figure 1.2 for a visual example of the physical differences between local and high redshift galaxies. In particular, galaxies tended to have smaller effective radii

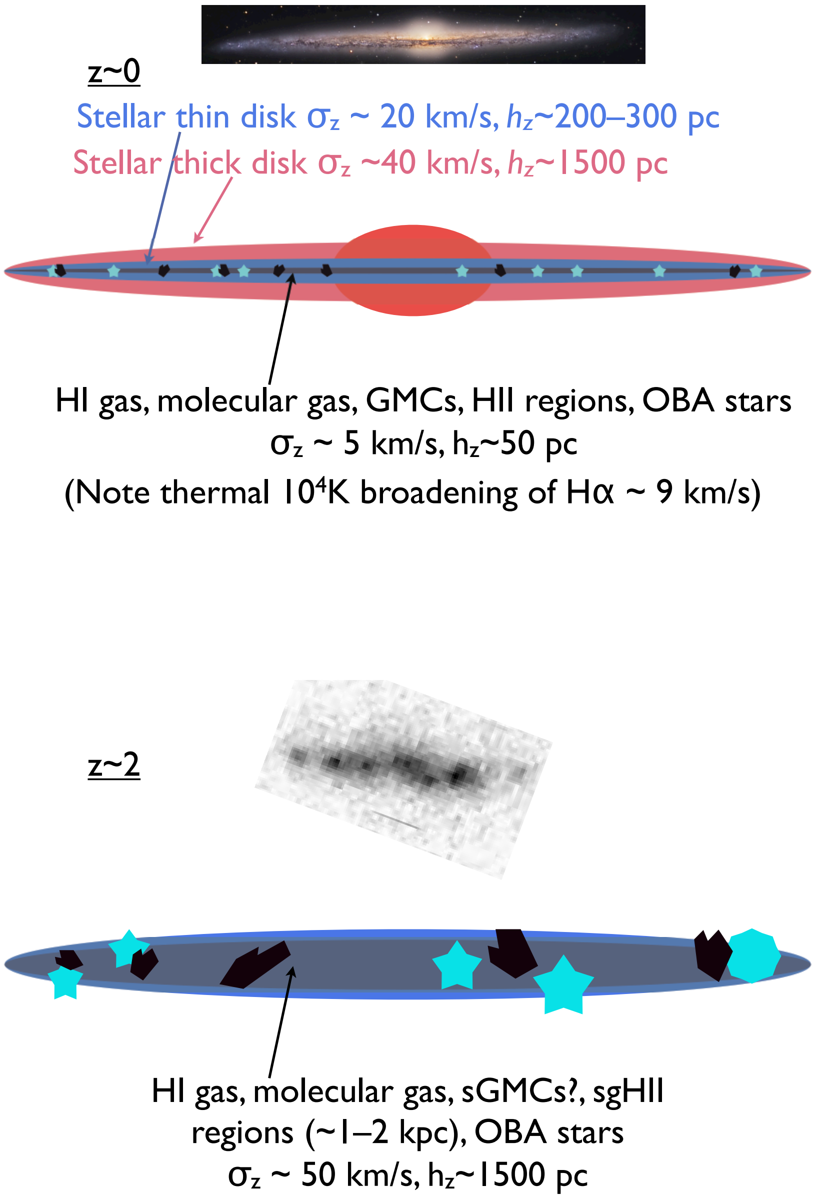

Figure 1.2: The varying properties of low and high redshift star-forming galaxies. Top: We see that local galaxies tend to have smooth, disky morphologies, low levels of random motions, and thin disks. Bottom: Comparatively, high-z galaxies have clumps of gas on the order of 1-2 kiloparsecs, thick disks, and high levels of random motions. Above each model, an example image of each type of galaxy is seen. Image from Glazebrook (2013). Reproduced by permission of K. Glazebrook and Publications of the Astronomical Society of Australia.

(van der Wel et al., 2012), higher gas fractions (Tacconi et al., 2013), higher SFRs (Erb et al., 2006), more irregular morphology (such as gas-rich clumps), and more turbulent internal kinematics (Simons et al., 2017). Due to increased levels of random motions, the TFR has high scatter at higher redshift (Kassin et al., 2007). By including a component of velocity dispersion in measurements of overall kinematics, this scatter tightens considerably (Weiner et al., 2006; Kassin et al., 2007).

1.3 The FourStar Galaxy Evolution Survey, ZFOURGE

Observations of higher-z galaxies have historically been limited by instrumentation. At $z \sim 2$ the diagnostic optical nebular emission lines are shifted to the near-infrared. New infrared instrumentation, in this case the FourStar instrument on the Magellan telescope, has allowed astronomers to push their observations to observe highly redshifted galaxies. Additionally, new infrared instruments are attached to space telescopes such as Spitzer, the Hubble Space Telescope, and (hopefully soon) the James Webb Space Telescope, and large ground-based telescopes such as Keck, the Very Large Telescope, and Magellan. Both large ground-based telescopes and space-based telescopes provide the angular resolution to observe high-redshift galaxy sizes, although the resolving of individual stellar populations or color and metallicity gradients remains impossible.

The ZFOURGE survey (Straatman et al., 2016) used the FourStar instrument to measure precise photometric redshifts using medium-band near-infrared filters. Medium-band filters allow a precise measurement of spectral features such as the 4000Å break without need for a spectrograph due to increased sampling. It was a large, deep survey of three HST legacy fields (CDFS, COSMOS, and UDS) which provided a reference of ∼60,000 galaxies at $z > 1$. The photometric redshifts provided were accurate to spectroscopic redshifts within $1 - 2\%$. The work of the ZFOURGE team created a reference for galaxy properties from $1 < z < 6$, notably scaling relations and mass and luminosity functions for galaxies up to $z = 4$ (Tomczak et al., 2014; Straatman et al., 2014; Spitler et al., 2014; Kawinwanichakij et al., 2014; Allen et al., 2015; Straatman et al., 2015; Kawinwanichakij et al., 2016; Papovich et al., 2015; Cowley et al., 2016; Tomczak et al., 2016; Forrest et al., 2016).

The ZFOURGE collaboration explored the effect of environment and mass on galaxy quenching mechanisms and stellar mass functions (Spitler et al., 2012; Kawinwanichakij et al., 2014, 2016; Forrest et al., 2017; Kawinwanichakij et al., 2017; Papovich et al., 2018). During this work, they identified over-dense regions at $z > 1.5$, most notably the COSMOS proto-cluster at $z = 2.095$, prominently featured in this work. Due to the precise photometric measurements determined by ZFOURGE, the cluster was identified using density mapping (Spitler et al., 2012), and they did not detect X-ray emission, indicating the young age of the cluster. Spectroscopic follow-up would later confirm the cluster and provide observations for this work.

1.4 ZFIRE: A Survey of Proto-Clusters at $z = 1.62$ and $z = 2.09$

The ZFIRE survey (Nanayakkara et al., 2016) was a spectroscopic follow-up to two clusters at the peak of cosmic star-formation history. The goal of this survey was to study the formation of galaxies in cluster, and observe the physical properties of the interstellar medium (ISM), and study the cycle of baryons between stars and gas. Observations were taken from the MOSFIRE near-infrared (NIR) multi-object spectrograph on Keck I. The ZFIRE observations were over a period of four years, with 12 nights awarded (7 of which were lost due to poor weather).

Despite observational difficulties, ZFIRE spectroscopically confirmed the COSMOS proto-cluster at $z = 2.095$ and derived a cluster velocity dispersion of 552 ± 52 km s^{-1} (Yuan et al., 2014). Galaxies associated with the cluster, as well as observations of field galaxies at $1.7 < z < 2.5$, were analyzed extensively by the ZFIRE team. The confirmed cluster members and relative density of galaxies from the mean density of the field are shown in Figure 1.3. The gas-phase metallicity (Kacprzak et al., 2015), SFR (Tran et al., 2017), and nebular gas properties (Kewley et al., 2015) were shown not to correlate with environment. In this work, we present the kinematic scaling relations and a re-analysis of the gas-phase metallicity and nebular gas properties of the COSMOS cluster.

The other cluster observed by ZFIRE was originally identified by Papovich et al. (2010); Tanaka et al. (2010). This cluster was identified from Spitzer imaging, an X-ray signal, had

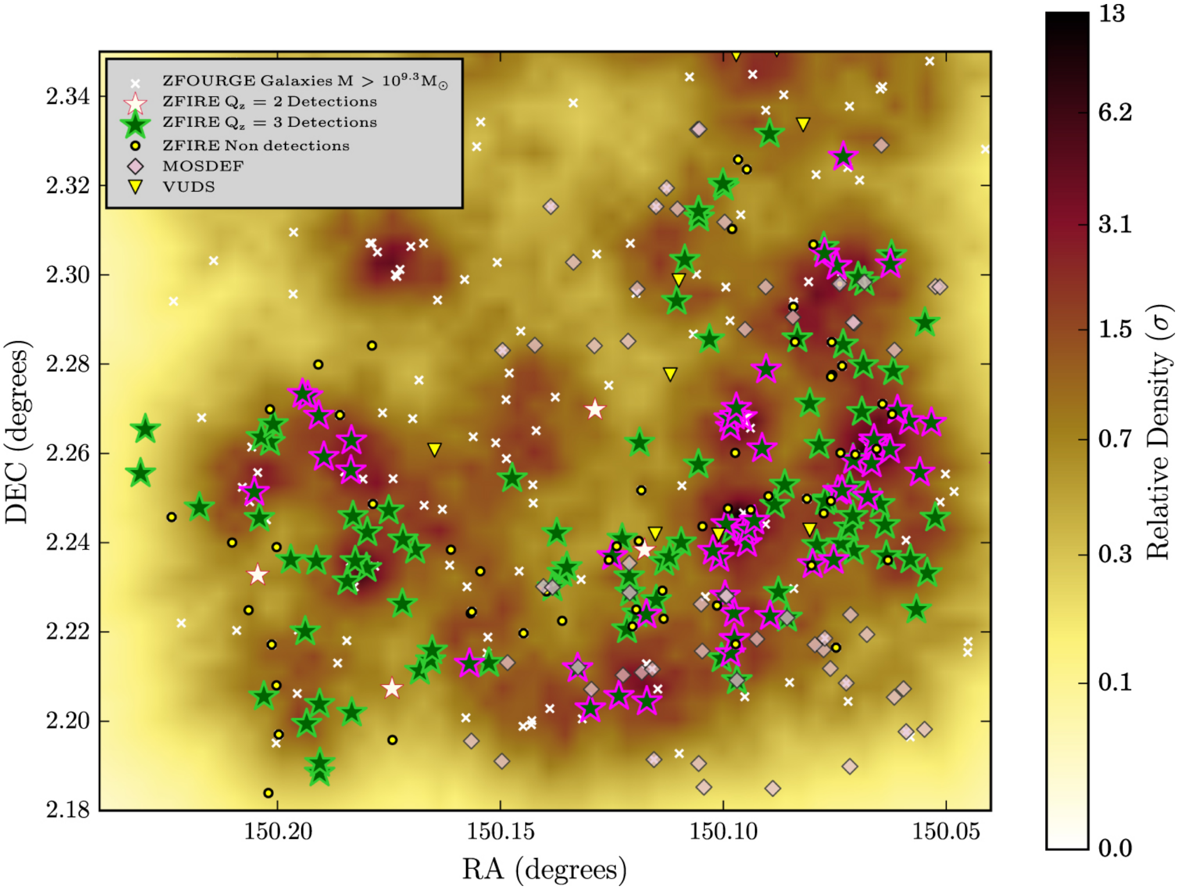

Figure 1.3: A proto-cluster at $z \sim 2$ from the ZFIRE survey. This particular proto-cluster consists of four merging groups. This image shows detections in the proto cluster, and the relative deviation in density compared to the field. Image credit: Nanayakkara et al. (2016). Reproduced by permission of the AAS.

a prominent red sequence, and was spectroscopically confirmed at $z = 1.62$. The cluster masses derived from cluster velocity dispersion (254 ± 50 km s^{-1}) and X-ray luminosity were consistent. The gas-phase metallicity was shown not to have any offsets from the field (Tran et al., 2015). In this work, we present a re-analysis of gas-phase metallicity and a BPT analysis of the nebular gas of the UDS cluster.

1.5 Outline

We begin our work by studying the integrated (overall) kinematics of cluster and field galaxies in COSMOS. When this work was published, it was the farthest direct measurement of the relationship between kinematics and environment. We used the bright Hα emission line to measure line widths, which measure the overall kinematics (the integrated velocity dispersion, or $\sigma_{\rm int}$). Since the kinematics trace the gravitational potential of the galaxy, through the virial theorem we can obtain an estimate of the dynamical mass of a galaxy (that is, the total mass of dark and baryonic matter). Additionally, because we are measuring our kinematics from the Hα line, we can also extract the Hα flux, and apply the Kennicutt-Schmidt Law to estimate a gas mass, and add this to the stellar mass to obtain an estimate for baryonic mass. These measurements will be used to compare the kinematics, dynamical masses, and baryonic masses of galaxies in the COSMOS $z = 2.095$ cluster and field galaxies. Additionally, we provide a measurement of the baryon fraction within the inner effective radius ($\sim$1-2 kiloparsecs).

We continue our analysis of galaxy kinematics at $z \sim 2$ by modeling the separation of the kinematic parameters $V_{2.2}$ (the rotational velocity of a galaxy at $2.2r_e$, where the disk theoretically reaches its peak velocity (Freeman, 1970)) and σ_g (the gas velocity dispersion). We separate the COSMOS sample into two morphological bins. From HST imaging, we fit the galaxy with a Sérsic index profile, and categorize galaxies with poor fits (clumpy morphology) into a "irregular" category, and galaxies with good fits to a "regular" category. Because our analysis constraints on galaxy orientations, our sample of cluster galaxies was too small to perform a reliable analysis of environment. Instead, we attempt to determine the origin of clumpy morphology in a mixed sample by measuring the velocity, velocity dispersion, and angular momentum. We measure these quantities using an algorithm HELA (Heidelberg Emission Line Algorithm). HELA performs an interactive MCMC fit of a slit-based emission line by generating 3D data cube based kinematic models. We tested HELA's ability to recover input galaxy kinematics in Appendices A and B.

Our study of galaxy properties in proto-clusters concludes with an analysis of galaxy metallicity using a new strong line gas phase metallicity indicator (Dopita et al., 2016), and by measuring the properties of the nebular gas. We measure both individual galaxies in the COSMOS ($z = 2.095$) and UDS ($z = 1.62$) proto-clusters, and stacked populations binned by environment and stellar mass. By applying a new metallicity indicator, we can disentangle the effects of ionization parameter and electron density which this indicator is not sensitive to. Additionally, we can measure the ionization parameter and metallicity for our populations, and use this to determine the ionization properties of both COSMOS and UDS populations, and the effects of environment.

2. ZFIRE: THE KINEMATICS OF STAR-FORMING GALAXIES AS A FUNCTION OF ENVIRONMENT AT $Z \sim 2$

2.1 Introduction

At $z > 1$, cluster galaxies have significant ongoing star formation (Rettura et al., 2010; Tran et al., 2010; Brodwin et al., 2013; Santos et al., 2014). The presence of emission lines in cluster galaxies at $z > 1.5$ provides an opportunity to investigate the effect of environment on emission line scaling relations. Galaxy properties in the local universe depend strongly on environment, e.g. stellar mass, gas fraction, morphology, and star formation rate (SFR) (Dressler, 1980). However, at $z \sim 2$ little evidence for environmental effects on SFR and the Mass-Metallicity Relation (Tran et al., 2010; Kacprzak et al., 2015) and minor effects on size (Allen et al., 2015) have been observed. Kinematics and dynamical masses, which probe more fundamental properties of galaxies, so far have not been tested in cluster environments at $z > 1.5$.

Kinematic scaling relations track how mass and luminosity are correlated and can be interpreted in terms of stellar mass and dynamical (total) mass. Studies of local emission line scaling relations, like the Tully-Fisher relation (TFR) (Tully and Fisher, 1977), find that cluster and field populations follow the same trends (Mocz et al., 2012; Bösch et al., 2013). It is unknown if environment is correlated with kinematics at higher redshifts, as few clusters have been confirmed at $z > 1.5$.

Observations of field galaxies show that stellar-mass scaling relations stay relatively consistent with local measurements until $z \sim 1.7$ (Kassin et al., 2007; Miller et al., 2011; Di Teodoro et al., 2016). Some observations also suggest that these relations evolve at $z > 2$

Reprinted with permission from "ZFIRE: The Kinematics of Star-Forming Galaxies as a Function of Environment at $z \sim 2$" by Alcorn, L., et al., 2016, *The Astrophysical Journal Letters*, Volume 825, Letter 2, Copyright 2016 American Astronomical Society.

(Cresci et al., 2009; Gnerucci et al., 2011; Straatman et al., 2017). This is possibly because gas fractions are higher at these redshifts, as supported by recent observations (Daddi et al., 2010; Tacconi et al., 2013) and predicted by simulations (Dutton et al., 2011). It is unclear whether cluster galaxies follow the same trends as the field, or if they evolve at higher redshift. As such, offsets in kinematics between cluster and field galaxies could indicate different evolutionary states in denser environments, e.g. the increasing fraction with redshift of post-starburst galaxies in clusters that span a range of velocity dispersions (Tran et al., 2003).

Observations have shown that kinematics for both resolved and unresolved objects can be tracked using integrated velocity dispersion, σ_{int}, measured with emission lines such as Hα (for a review of kinematic surveys using this technique, see Glazebrook (2013)). Here we present the most distant study yet to compare Hα kinematics of individual cluster galaxies and field galaxies. Our data consists of objects measured by the ZFIRE survey (Nanayakkara et al., 2016), including the $z = 2.095$ overdense region in the COSMOS field (Spitler et al., 2012; Yuan et al., 2014).

ZFIRE targets galaxy clusters at $z \sim 2$ to explore galaxy evolution as a function of environment. ZFIRE combines deep multi-wavelength imaging with spectroscopy obtained from Keck/MOSFIRE (McLean et al., 2012) to measure galaxy properties including sizes, stellar masses, star formation rates, gas-phase metallicities, and the interstellar medium (Kacprzak et al., 2015; Kewley et al., 2015; Tran et al., 2015; Nanayakkara et al., 2016).

In this work, we assume a flat ΛCDM cosmology with Ω_M=0.3, Ω_Λ =0.7, and H$_0$=70. At the cluster redshift, $z = 2.09$, one arcsecond corresponds to an angular scale of 8.33 kpc.

2.2 Data

2.2.1 HST Imaging

Our morphological measurements are from Cosmic Assembly Near-Infrared Deep Extragalactic Survey (CANDELS) imaging (Koekemoer et al., 2011; Grogin et al., 2011) processed by the 3D-HST team (v4.1 data release). For details on the reduction of CANDELS imaging, see Skelton et al. (2014). We use GALFIT software (Peng et al., 2010) to measure galaxy sizes from the F160W imaging. Examples of CANDELS/3D-HST imaging of galaxies in our sample can be seen in Figure 2.1.

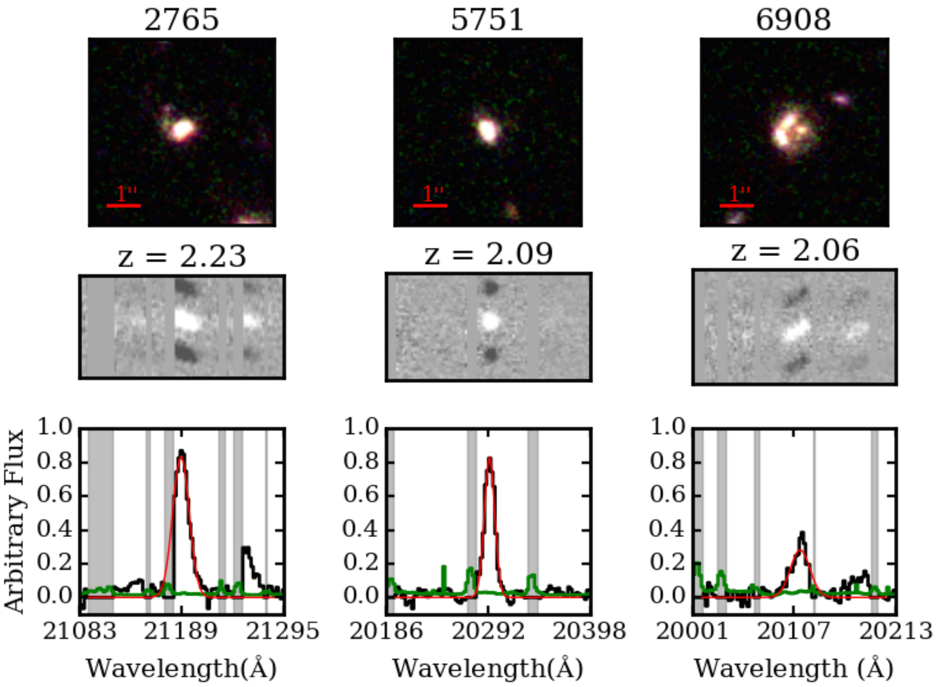

Figure 2.1: Top: RGB images of three galaxies in the ZFIRE sample. ID numbers are object IDs listed in the ZFIRE catalog (Nanayakkara et al., 2016). RGB colors are from CANDELS/3D-HST imaging in F160W (Red), F140W (Green), and F125W (Blue). Middle: Example flux and telluric corrected spectra from the ZFIRE pipeline corresponding to the images in the top row. Here we see the Hα and [N II] emission lines. Bottom: 1D summed spectra in black, and the error spectrum in green. We plot the Gaussian fit to the data in red. Masked sky regions are in grey. Reproduced by permission of the AAS.

We generate a custom pipeline to fit the 161 COSMOS galaxies in ZFIRE with F160W imaging using initial measurements of size, axis ratio (q), position angle (PA), and magnitude from SExtractor (Bertin and Arnouts, 1996). Our constraints are adopted from the constraints in van der Wel et al. (2014), and our point-spread function is constructed by 3D-HST. Objects within 2" of a target galaxy are simultaneously fit with the central object. Residual images are visually inspected to determine the best possible fits for each galaxy. Galaxies with poor residuals are refit using a different set of initial parameters, and rejected if a satisfactory solution can not be obtained. Our results are consistent within 2σ to van der Wel et al. (2012).

Errors for our GALFIT measurements are obtained by adding sky noise to the GALFIT model, and rerunning GALFIT 200 times per object. The range of the error is obtained from the 1σ confidence intervals.

The size of the galaxy is obtained using q and the effective radius, r_e, from GALFIT. We convert this to a circularized effective radius using $R_e = r_e\sqrt{q}$. The properties of our overall population show no significant size dependence on environment. This is in conflict with Allen et al. (2015) who find evidence that star-forming galaxies in the cluster are larger than in the field. However, we stress that this is likely because our analysis is limited to the smaller set of H$\alpha-$detected galaxies.

2.2.2 ZFOURGE Photometry

The COSMOS cluster was initially identified by Spitler et al. (2012) using photometric redshifts from ZFOURGE (Straatman et al., 2016) and subsequently confirmed with spectroscopic redshifts from MOSFIRE (Yuan et al., 2014). ZFOURGE combines broad-band imaging in K and the medium-band J$_1$, J$_2$, J$_3$, H$_s$, and H$_l$ filters to select objects using Ks-band images with a 5σ limit of 25.3 AB magnitudes.

ZFOURGE uses FAST (Kriek et al., 2009) to fit stellar population synthesis models to the galaxy spectral energy distributions to estimate observed galaxy properties. We assume a Chabrier (2003) initial mass function with constant solar metallicity and an exponentially declining star formation rate, and a Calzetti et al. (2000) dust law.

2.2.3 MOSFIRE NIR Spectroscopy

Observations were taken in December 2013 and February 2014 in the K-band filter covering 1.93-2.45 μm, the wavelength range we would expect to see Hα and [N II] at the cluster redshift. Targets were star-forming galaxies (SFGs) selected from rest frame UVJ colors. Seeing varied from $\sim 0.4''$ to $\sim 0.7''$ over the course of our observations.

The spectra are flat-fielded, wavelength calibrated, and sky subtracted using the MOSFIRE data reduction pipeline (DRP)[*]. We use a custom ZFIRE pipeline to correct for telluric absorption and perform a spectrophotometric flux calibration using a type A0V standard star. We flux calibrate our objects to the continuum of the standard star, and use ZFOURGE photometry to correct offsets between photometric and spectroscopic magnitudes. The final result of the DRP are flux-calibrated 2D spectra (see examples in Figure 2.1) and 2D 1σ images used for error analysis, with a bootstrapped flux calibration error of $< 10\%$ (~0.08 magnitudes). For more information on ZFIRE spectroscopic data reduction, see Nanayakkara et al. (2016).

We extract 1D spectra from an aperture the width of the one Gaussian sigma (1σ) boundaries of the spatial Hα emission-line profile. Varying the aperture width does not affect our results. The 1D Hα line width is determined by fitting a Gaussian profile to the Hα emission line. We subtract the measured instrumental broadening in quadrature from the line width, and convert the corrected line width to σ_{int} using the best-fit redshift from Nanayakkara et al. (2016). Errors are calculated by adding sky noise to the observed spectrum, and refitting 1000 times.

We test if slit misalignment affects our results. After rejecting objects with $\Delta\alpha > 40°$, where $\Delta\alpha$ is the difference between the GALFIT-measured PA and the angle of the slit, our sample decreases to 26 objects overall, 7 in the cluster. However, our results do not significantly change, so we conclude the slit misalignment does not significantly affect our final results for our scaling relations or virial mass measurements and do not include galaxy PA corrections or restrictions in our analysis.

All Gaussian line fits are visually inspected. Emission lines with sky contamination are given a lower quality flag than emission lines without contamination, but are included in our

---

[*] http://www2.keck.hawaii.edu/inst/mosfire/drp.html

sample (Figure 2.2). Measurements with signatures of AGN as detected in Cowley et al. (2016), objects completely obscured by sky emission, or objects too faint to detect manually are excluded from our analysis. After our rejection criteria, the sample contains 75 COSMOS galaxies, 28 of which are associated with the $z \sim 2$ cluster.

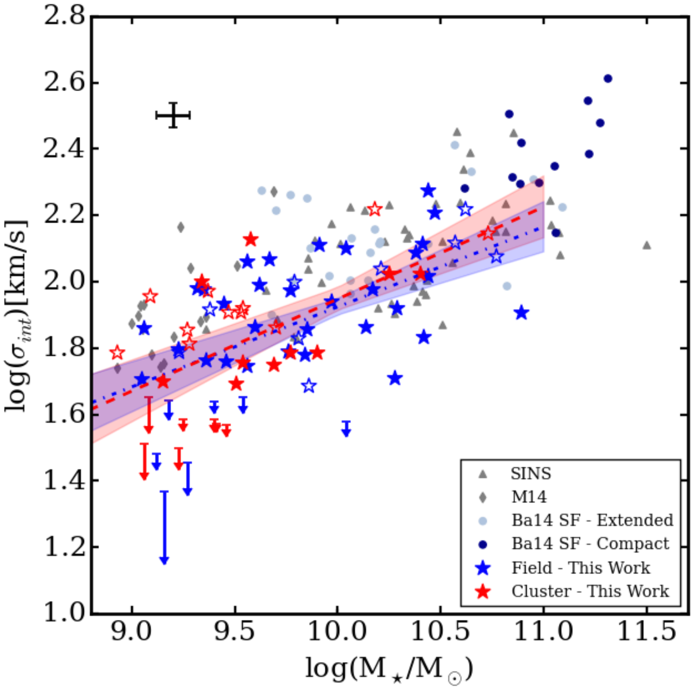

Figure 2.2: Stellar mass vs σ_{int} of the ZFIRE galaxies. Size and color of the points refers to the quality of the spectroscopic measurement: filled points for confirmed line widths, outlined points for faint emission lines or emission lines partially obscured by sky interference. Blue stars are field galaxies, and red stars are galaxies in the $z \sim 2.09$ cluster identified in Spitler et al. (2012). Characteristic errorbars are located in the upper left, in black. We compare the ZFIRE COSMOS sample with emission-line $z \sim 2$ field galaxies from Barro et al. (2014) (written as Ba14), Förster Schreiber et al. (2009) (written as (SINS), and Masters et al. (2014) (written as M14). Objects with line width less than instrumental resolution are displayed as upper limits. The bootstrapped 1σ confidence intervals of the least-squares linear fits are shown as translucent boxes around the best fit lines. We see no significant difference between the best-fit relations for cluster and field. Reproduced by permission of the AAS.

The cluster objects are defined as objects identified with three strongly over-dense regions of the COSMOS field. In Spitler et al. (2012), these overdensities are found by computing surface density maps. In Yuan et al. (2014), these objects are spectroscopically confirmed and concentrated at $z_c = 2.095$, and are consistent with a Gaussian distribution with $\sigma_z = 0.005$. The redshift range for the cluster is defined to be $z_c \pm 3\sigma_z$. The COSMOS overdensity velocity dispersion is measured to be $\sigma_{v1D} = 552 \pm 52$ km s^{-1}, and has 57 spectroscopically confirmed members. It consists of four major groups that cover a total projected size of 3.7×5 Mpc^2 (7.4×10 Mpc^2 comoving). The cluster is most likely to evolve into a Virgo-like cluster at $z \sim 0$ (Yuan et al., 2014). Field objects are defined as targeted objects not within the cluster redshift range or associated spatially with the cluster.

2.3 Results

2.3.1 Hα Emission-Line Widths at $z \sim 2$

By measuring kinematics from the Hα line width, we assume that the broadening is caused by the gravitational potential of the galaxy acting on the gas. We also use $\sigma_{\rm int}$ since it can be measured for all galaxies, even those with unresolved rotation, and is robust against PSF effects. $\sigma_{\rm int}$ could trace rotation, velocity dispersion, or a combination of both quantities (Glazebrook, 2013; Barro et al., 2014; Masters et al., 2014). Hα integrated velocity dispersions of ZFIRE COSMOS galaxies range from ~50-230 km s^{-1}, an expected distribution of values for extended (rather than compact) SFGs (Figure 2.2). The median $\sigma_{\rm int}$ is 72.8 km s^{-1}.

We determine a linear least-squares fit to the cluster, field, and total ZFIRE samples (Table 2.1) normalized at log(M$_\star$)=10. The least-square linear fits relation is of the form log(y) = A(log(x)-10) + B. The best-fit relation is bootstrapped 1000 times to determine 1σ confidence intervals of the linear fit. The best-fit log(M$_\star$)-log($\sigma_{\rm int}$) relations for cluster ($A = 0.28 \pm 0.06$, $B = 1.95 \pm 0.03$) and field ($A = 0.24 \pm 0.05$, $B = 1.92 \pm 0.03$) are consistent within 1σ (Table 2.1), indicating no evidence of environmental influence on kinematics. The median residual of the points around each best-fit line is ~ 0.12 dex, and cluster and field relations overlap within this scatter. Our results do not depend on whether or not we apply weighting from our errors on $\sigma_{\rm int}$.

x	y	Environment	A	B	N	Residual
$M_\star$	$\sigma_{\rm int}$	Cluster	0.28±0.06	1.95±0.03	28	0.12
		Field	0.24±0.05	1.92±0.03	47	0.13
		Total	0.25±0.04	1.93±0.02	75	0.11
$M_\star$	$M_{\rm vir}$	Cluster	0.86±0.16	10.23±0.08	28	0.30
		Field	0.79±0.13	10.26±0.06	47	0.21
		Total	0.82±0.10	10.25±0.05	75	0.24
$M_{\rm baryon}$	$M_{\rm vir}$	Cluster	0.92±0.17	9.98±0.07	28	0.32
		Field	0.87±0.12	10.04±0.05	47	0.23
		Total	0.90±0.11	10.02±0.04	75	0.25

Table 2.1: The least-square linear fits relation is of the form log(y) = A(log(x)-10) + B. Errors are determined by bootstrapping the data 1000 times, and determining the 1σ confidence intervals of the bootstrapped results. N is the number of objects used for the linear fit. The residual quoted is the median residual value from the best fit line. $\sigma_{\rm int}$ is in units of km s^{-1}. We do not apply a weight to these fits. Reproduced by permission of the AAS.

To quantify our ability to recover 1D line widths, we use a set of 2D emission-line models with exponential disks, an arctangent rotation profile, and known v_{rot} and gas σ. We add sky noise (as measured from our data) to the modeled galaxies, and collapse each emission line (simulated and with sky noise) to 1D line widths. We find that the simulated emission lines with noise differ by only ~0.01% compared to the input models.

We confirm that our results on cluster versus field do not depend on inclination corrections. To correct for inclination, Straatman et al. (2017) and Price et al. (2016) assume that the intrinsic axis ratio is $q_0 = 0.19$. When we apply this correction, the scatter of our points around our best-fit values decreases by ~ 0.01 dex and the values are offset from the uncorrected values by 0.05 dex. If we do not correct for inclination, we tend to underestimate the input virial mass of our modeled galaxies by ~ 0.25 dex. However, this assumes that the models accurately represent the true galaxy kinematics. Because an inclination correction does require assuming an intrinsic axis ratio and applying an inclination correction does not change our overall results, we use uncorrected $\sigma_{\rm int}$ values so that we can compare directly to recent results by Barro et al. (2014); Masters et al. (2014). We will explore the effects of inclination corrections in future work.

In the right panel of Figure 2.2 we compare the ZFIRE sample to the 1D field objects of Barro et al. (2014), the 1D field objects of Masters et al. (2014), and the 2D Integral Field Unit (IFU) field objects of the Spectroscopic Imaging survey in the NIR with SINFONI sample (SINS) (Förster Schreiber et al., 2009). We see consistent values of $\sigma_{\rm int}$ with SFGs in these samples. We also have compared our emission-line kinematics with the independent analysis of ZFIRE spectra presented by Straatman et al. (2017), and find consistent 1D line widths with their collapsed best-fit 2D kinematic models.

2.3.2 Virial Masses

In Figure 2.3 we compare estimated virial mass to stellar mass for the COSMOS field and cluster objects and to other high-redshift kinematic surveys. While stellar mass can be estimated by spectral energy distribution fitting, which examines stellar populations and colors, virial mass accounts for the total mass of the galaxy including gas and dark matter.

To calculate virial mass, we apply the virial formula

$$M_{\rm vir}(< R_e) = K_e \frac{\sigma_{int}^2 R_e}{G}. \tag{2.1}$$

For comparison to recent results by Barro et al. (2014); Masters et al. (2014), we assume a virial factor K$_e = 5$. We find that our virial masses are consistent with these existing studies and Förster Schreiber et al. (2009). Our linear best-fit relations for the cluster and field (Table 2.1) shows no significant environmental impact on our fits: cluster and field relations differ by $< 1\sigma$.

In our analysis, we use a constant virial factor but note that K_e depends on the structural parameters of the galaxy. Values in the literature range from $K_e \sim 2 - 10$ and using, $e.g.$ K$_e = 3.4$ from Erb et al. (2006) will introduce an offset of ~ -0.2 dex in our results. However, we stress that the relative comparison between cluster and field does not change.

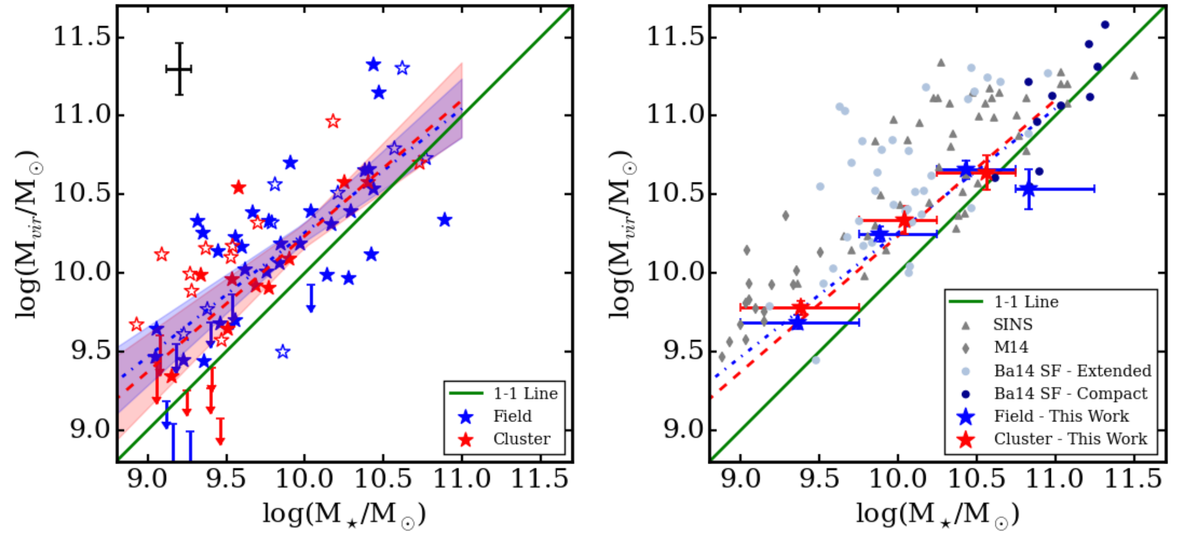

Figure 2.3: Left: Estimated virial masses obtained from the virial formula vs. stellar masses. Best-fit relations are included with 1σ deviation boxes, in the same colors as represented in Figure 2.2. Right: Virial masses binned by stellar mass. Errors in $\log(M_{\star}/M_{\odot})$ are the width of each bin. We compare the ZFIRE sample to the $z \sim 2$ field galaxies of Förster Schreiber et al. (2009), Barro et al. (2014), and Masters et al. (2014) to find consistent values with extended SFGs. Reproduced by permission of the AAS.

2.3.3 Estimating Gas Mass from the Kennicutt-Schmidt Relation

Gas masses are estimated from the Schmidt-Kennicutt relation (referred to here as the Kennicutt-Schmidt relation) (Kennicutt, 1998), using SFRs from Hα line fluxes corrected for dust using the method described in Tran et al. (2017). We assume a nebular attenuation from Cardelli et al. (1989) with $R_V = 3.1$, and a Calzetti et al. (2000) dust law. We calculate the SFR surface density, $\Sigma_{SFR} = SFR/(\pi R_{H\alpha}^2)$ and use the Kennicutt-Schmidt relation to solve for gas surface density, $\Sigma_{gas} = M_{gas}/(\pi R_{H\alpha}^2)$. $R_{H\alpha}$ is the circularized effective radius in kiloparsecs, after we have applied a correction factor from Nelson et al. (2016) to estimate the Hα radius from the stellar radius and mass. We add the estimated gas mass to the stellar mass to derive baryonic masses.

In Figure 2.4, we show a comparison between estimated baryonic and virial masses. Objects move closer to the unity relation than in Figure 2.3 due to high gas masses (the median gas fraction in the ZFIRE sample is 0.36, typical of the field galaxies seen in Tacconi et al.

(2013)). This implies most objects are baryon-dominated within one effective radius. We again find no significant environmental impact on the values for $M_{\rm baryon}$ vs. $M_{\rm vir}$, relations are consistent within 1σ. The MOSDEF survey similarly finds that field galaxies at $z \sim 2$ are distributed around the 1-1 line (Price et al., 2016).

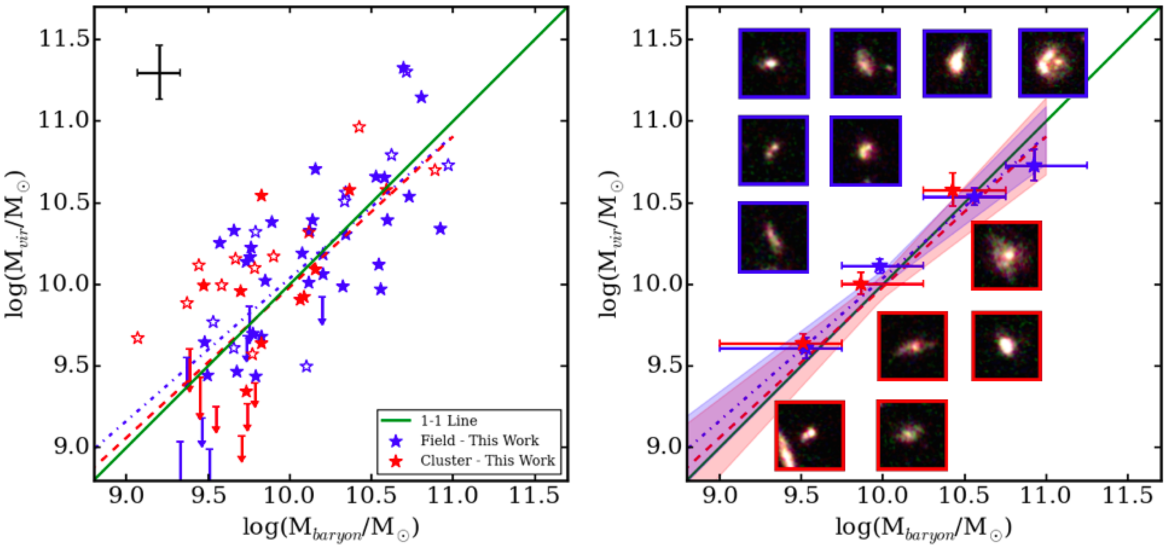

Figure 2.4: Left: Virial masses obtained from the virial formula compared to estimated baryonic masses. Baryonic masses are from the addition of stellar masses and gas masses computed from dust-corrected Hα fluxes and the Kennicutt-Schmidt relation (Kennicutt, 1998). We use the same colors as represented in Figure 2.2, with characteristic errorbars for our data in black in the upper left of the panel. Right: Virial mass binned by baryonic mass. We include $3'' \times 3''$ RGB images of selected galaxies in each bin. Borders around the RGB cutouts are blue for field galaxies, and red for cluster galaxies. Reproduced by permission of the AAS.

2.4 Summary

Using the Keck I MOSFIRE NIR spectrograph, we measure Hα emission lines of 28 COSMOS $z = 2.095$ star-forming cluster galaxies and 47 star-forming field galaxies to investigate environmental effects on high-redshift proto-clusters. Our objects are rest frame UVJ selected star-forming galaxies with no detected X-Ray, IR, or radio AGN signatures.

We measure Hα line widths to derive integrated velocity dispersions, σ_{int}, and use CANDELS/3DHST F160W imaging to measure galaxy sizes.

We derive high-redshift emission-line kinematic scaling relations and did not find any significant environmental effects; cluster and field least-squares linear relations were consistent within error. Compared to previous multi-slit and IFU kinematic surveys of the $z \sim 2$ field, (Barro et al., 2014; Masters et al., 2014; Förster Schreiber et al., 2009), we find consistent results in the $\mathrm{M}_{\star}$-σ_{int} relation with extended SFGs.

We estimate virial masses (which includes stellar, dark matter, and gas mass) for our galaxies from our gas kinematics. Gas masses were derived from dust-corrected Hα star-formation rates and the Kennicutt-Schmidt relation, and added to stellar masses to estimate baryonic masses. The median values for log($\mathrm{M}_{\mathrm{vir}}$/$\mathrm{M}_{\star}$) and log($\mathrm{M}_{\mathrm{vir}}$/$\mathrm{M}_{\mathrm{baryon}}$) are 0.30 and 0.07, respectively. We find consistent values between baryonic and virial mass estimates, showing baryon dominance within one effective radius from the center of these galaxies. There is no statistically significant evidence of environmental impacts on our sample; cluster and field best-fit relations in $\mathrm{M}_{\star}$-$\mathrm{M}_{\mathrm{vir}}$ and $\mathrm{M}_{\mathrm{baryon}}$-$\mathrm{M}_{\mathrm{vir}}$ are consistent within 1σ.

Our results demonstrate that the integrated gas kinematics of SFGs in the $z = 2.095$ overdensity are not strongly dependent on environment. Further studies of $z > 1.5$ cluster galaxies are needed to confirm our results. In addition, studies of $z > 1.5$ cluster galaxy absorption-line kinematics would also provide an opportunity to compare gas and stellar kinematics. In future work we will present an analysis of the Tully-Fisher relation of our galaxies to investigate the contributions of rotational velocity and velocity dispersion as a function of environment.

3. ZFIRE: 3D MODELING OF ROTATION, DISPERSION, AND ANGULAR MOMENTUM OF STAR-FORMING GALAXIES AT $Z \sim 2$

3.1 Introduction

The ΛCDM model predicts galaxies build their angular momentum through tidal interactions until the dark matter halo virializes (White and Rees, 1978; Fall and Efstathiou, 1980; Mo et al., 1998). Dark matter-dominated gravitational potentials accrete primordial gas, which collapses into galaxy disks. The angular momentum of the baryonic disk of a galaxy has been shown to correlate with the angular momentum of the dark matter halo in the overall population of star-forming galaxies (SFGs), and is therefore a fundamental indicator of the total (baryonic and dark matter) growth of galaxies (Emsellem et al., 2007; Romanowsky and Fall, 2012; Obreschkow and Glazebrook, 2014; Cortese et al., 2016).

As the baryonic matter collapses to form a disk, angular momentum will be subject to change due to gas accretion or merging events (Vitvitska et al., 2002; Lagos et al., 2017; Penoyre et al., 2017). In the case of cold gas accretion, as matter accretes onto the gravitational potential, a torque on the galaxy can be exerted and the angular momentum increases with time (White, 1984; Kereš et al., 2005; Sales et al., 2012; Stewart et al., 2013; Danovich et al., 2015). In the case of minor or major mergers, the angular momentum can increase or decrease based on the geometry of the merger itself (Vitvitska et al., 2002; Puech et al., 2007; Naab et al., 2014; Rodriguez-Gomez et al., 2017). However in a number of cases, both observed and simulated, galaxies with clear signs of disrupted morphology show coherent rotation (Hung et al., 2015; Turner et al., 2017; Rodriguez-Gomez et al., 2017). This could be caused by a merger that is at the correct orientation to increase the angular momentum of

---

Reprinted with permission from "ZFIRE: 3D Modeling of Rotation, Dispersion, and Angular Momentum of Star-Forming Galaxies at $z \sim 2$" by Alcorn, L., et al., 2018, *The Astrophysical Journal*, Volume 858, Article 47, Copyright 2018 American Astronomical Society.

the system. If major mergers are a significant part of galaxy evolution, then we should see a large scatter in angular momentum relations.

The mass - angular momentum plane can be mapped to the Fundamental Plane for spiral galaxies (Obreschkow and Glazebrook, 2014), and the projection of this plane forms the Tully-Fisher Relation (TFR, Tully and Fisher, 1977). However, high gas masses drive fundamental differences between local and high-redshift galaxies, most notably by increasing the star-formation rate (SFR), the increasing thickness of disks, the formation of large star-forming clumps, and the increased contribution of the gas velocity dispersion (σ_g) to the total kinematics of SFGs (Tacconi et al., 2010; Daddi et al., 2010; Obreschkow et al., 2016). The increase in σ_g could also be affected by cold-mode accretion or merging events, which could cause disk instabilities or loss of angular momentum (Hung et al., 2015). Kassin et al. (2007) accounted for the increased scatter of the TFR by including σ_g in the kinematic quantity $\mathrm{S}_{0.5}$. The scatter of the $\mathrm{S}_{0.5}$-$\mathrm{M}_\star$ relation is smaller than the scatter of the stellar - mass TFR at all redshifts. $V_{2.2}/\sigma_g$ is also used in multi-object slit spectroscopic surveys to quantify the rotation support against random motions (Price et al., 2016; Simons et al., 2017). However, significant scatter still remains in the TFR, $\mathrm{S}_{0.5}$, and $V_{2.2}/\sigma_g$ spaces explored by recent high-redshift surveys. Median values of these datasets demonstrate the decrease of σ_g and increase of V_{rot} with time and stellar mass, possibly indicating kinematic downsizing and the formation of disky SFGs (Kassin et al., 2007; Simons et al., 2016, 2017).

In this work, we investigate the relationship between irregular morphology and kinematics. Due to the availability high-resolution photometry by the Hubble Space Telescope (HST), we can examine the morphologies of galaxies at $z \sim 2$, in conjunction with the kinematic signatures provided by Keck/MOSFIRE (McLean et al., 2012). This will provide morphological signatures of recent merging events and irregular structure for our sample, which will allow us to determine if these morphologies are correlated with any kinematic effects such as increased σ_g, or an increased scatter in kinematic scaling relations in possible merging events.

These processes have been explored extensively and with great spatial precision in IFU surveys (Epinat et al., 2009; Law et al., 2009; Förster Schreiber et al., 2009; Swinbank et al., 2012; Wisnioski et al., 2015) (for a thorough review of these surveys, see Glazebrook, 2013). However, since IFU data requires light from a source to be separated into different spaxels rather than integrated into a single slit, low-mass (log(M$_\star$/$M_\odot$) $<$ 10.5) and faint galaxies are not well-represented by these data (Wisnioski et al., 2015; Burkert et al., 2016). Additionally, these surveys also tend to exclude morphologically complex galaxies and galaxies with misaligned kinematic and morphological position angles (PA), as well as galaxies with $V_{2.2}/\sigma_g$< 2.

In contrast, surveys utilizing slit spectroscopy are more sensitive to low-mass and faint galaxies. Multi-object slit surveys demonstrate that the low-mass population is sensitive to the processes which affect angular momentum (Simons et al., 2016). These processes include star-formation feedback, disk instabilities caused by rapid accretion of surrounding gas, or mergers. This population is often more dispersion-supported and irregularly shaped than the higher mass population at $z \sim 2$. These low-mass objects can provide evidence for which processes shape galaxy evolution at the peak of cosmic star-formation history. In addition,slit surveys can measure larger data sets, over a variety of properties such as mass, luminosity, and environment. Here, we attempt to bridge the gap between IFU and slit surveys. To investigate the effects of slit against IFU spectroscopy, we simulate IFU data cubes, and project them through a slit to create a slit observation of an emission line.

Our data consist of objects from the COSMOS field (Capak et al., 2007) measured by the ZFIRE survey (Nanayakkara et al., 2016), including a $z = 2.095$ confirmed over-dense region in the COSMOS field (Spitler et al., 2012; Yuan et al., 2014). ZFIRE[†] targets galaxy clusters at $z \sim 2$ to explore galaxy evolution as a function of environment. ZFIRE combines deep multi-wavelength imaging with spectroscopy obtained from MOSFIRE to measure galaxy properties including sizes, stellar masses, star formation rates, gas-phase metal-

---

[†] zfire.swinburne.edu.au

licities, and the interstellar medium (Kacprzak et al., 2015; Kewley et al., 2015; Tran et al., 2015; Kacprzak et al., 2016; Alcorn et al., 2016; Nanayakkara et al., 2016; Tran et al., 2017; Straatman et al., 2017; Nanayakkara et al., 2017).

In this work, we assume a flat ΛCDM cosmology with Ω_M=0.3, Ω_Λ =0.7, and H_0=70. At the cluster redshift, $z = 2.095$, one arcsecond corresponds to an angular scale of 8.33 kpc.

3.2 Data

3.2.1 Sample Selection

Our sample is drawn from the ZFIRE survey (Nanayakkara et al., 2016), a spectroscopic follow-up of ZFOURGE photometry (Straatman et al., 2016). To summarize, we identify star-forming galaxies (SFGs) within a photometric redshift range of $1.7 < z < 2.5$ in ZFOURGE NIR imaging of COSMOS fields. ZFOURGE combines broad-band imaging in K_s and the medium-band J_1, J_2, J_3, H_s, and H_l filters to select objects using K_s-band images with a 5σ limit of 25.3 AB magnitudes. Rest-frame UVJ colors are used to identify SFGs, which will have prominent emission lines. Objects with radio, infrared, ultraviolet, or x$-$ray indications of AGN activity (identified via Cowley et al., 2016) are rejected from this analysis.

The COSMOS proto-cluster was initially identified in Spitler et al. (2012) using photometric redshifts from ZFOURGE and subsequently confirmed with spectroscopic redshifts from MOSFIRE (Yuan et al., 2014). This over-density consists of four merging groups, and is projected to evolve into a Virgo-like cluster at $z = 0$. Cluster members are identified to redshifts within $2.08 < z < 2.12$.

ZFOURGE uses FAST (Kriek et al., 2009) to fit Bruzual and Charlot (2003) stellar population synthesis models to the galaxy spectral energy distributions to estimate observed galaxy properties. After spectroscopic redshifts were obtained on MOSFIRE, objects were run in FAST using the spectroscopically confirmed redshifts rather than the photometric redshifts, providing our stellar masses and attenuation values (A_V). We assume a Chabrier

(2003) initial mass function with constant solar metallicity and an exponentially declining star formation rate, and a Calzetti et al. (2000) dust law.

3.2.2 HST Imaging

Our morphological measurements are from the Cosmic Assembly Near-Infrared Deep Extragalactic Survey (Grogin et al., 2011; Koekemoer et al., 2011, CANDELS) imaging processed by the 3D-HST team (v4.1 data release) (Skelton et al., 2014). Our PSF is also constructed by the 3D-HST team. We use GALFIT software (Peng et al., 2010) to measure galaxy sizes from the F160W imaging. At $z \sim 2$, F160W corresponds to rest-frame g-band. Our morphological fitting is summarized in Alcorn et al. (2016) but we briefly repeat here.

We generate a custom pipeline to fit the 161 COSMOS galaxies in ZFIRE with F160W imaging using initial measurements of size, axis ratio (q), position angle (PA), and magnitude from SExtractor. Objects within $2''$ of a target galaxy are simultaneously fit with the central object. Residual images are visually inspected to determine the best possible fits for each galaxy. Galaxies with poor residuals are re-fit using a modified set of initial parameters. Galaxies were restricted to Sérsic indices (n) between $0.2 - 8.0$. If objects iterated to the boundaries of our Sérsic constraints, they were refit with a fixed Sérsic index ($n = 1.0$ for objects which went to $n = 0.2$, and $n = 4.0$ for objects which went to $n = 8.0$) Our results are consistent within 2σ to van der Wel et al. (2014) (see Table 3.1).

25 objects in our final sample are considered to be regular galaxies by evaluation of GALFIT residuals. Examples of our sample showing regular and irregular galaxies by our criteria are shown in Figure 3.1. To determine the presence of irregular morphology or tidal features, we examine residual images. Using segmentation maps from SExtractor, we isolate the individual galaxies and measure the residual, the sky flux, and the flux of the original object. If residual levels are at more than 2 times the level of the sky, and more than 25% of the flux of the original object remains, we determine the presence of significant artifacts. If residual images show significant artifacts, which indicate that a Sérsic profile is a poor or unreliable fit to the object, they are flagged as irregulars, although this population

ID	Cluster/Field	Regular/Irregular	R_e (arcseconds)	Sersic Index	Axis Ratio	PA
1814	Field	Irregular	0.29±0.01	1.0±0.0	0.8±0.0	-11.6±3.7
1961	Field	Regular	0.28±0.01	0.4±0.1	0.6±0.0	68.6±2.3
2715	Cluster	Irregular	0.46±0.01	0.9±0.1	0.6±0.0	-87.4±1.3
2723	Cluster	Irregular	0.13±0.11	2.6±5.4	0.9±0.9	20.7±32.7
2765	Field	Irregular	0.34±0.01	4.0±0.0	0.7±0.0	-87.8±2.0
3074	Field	Irregular	0.46±0.01	1.0±0.0	0.5±0.0	-55.7±0.8
342	Field	Regular	0.38±0.01	0.8±0.0	0.5±0.0	44.7±0.6
3527	Field	Irregular	0.38±0.01	0.9±0.0	0.5±0.0	-12.8±0.5
3532	Cluster	Irregular	0.20±0.01	0.9±0.1	0.4±0.0	-54.4±0.9
3619	Field	Irregular	0.25±0.01	0.7±0.2	0.2±0.0	37.1±1.3
3633	Cluster	Regular	0.59±0.01	0.8±0.1	0.3±0.0	-85.1±0.6
3655	Field	Irregular	0.54±0.01	0.7±0.0	0.9±0.0	44.5±2.6
3680	Field	Irregular	0.34±0.01	0.6±0.1	0.5±0.0	-11.6±1.6
3714	Field	Irregular	0.32±0.01	0.9±0.0	0.7±0.0	1.3±0.2
3842	Cluster	Irregular	0.43±0.01	0.9±0.0	0.5±0.0	-54.9±0.6
3844	Field	Irregular	0.66±0.02	1.0±0.0	0.7±0.0	-60.8±1.8
3883	Field	Regular	0.19±0.01	0.9±0.2	0.8±0.1	29.3±9.3
4010	Field	Regular	0.29±0.01	0.6±0.1	0.6±0.0	-8.7±1.0
4037	Field	Regular	0.38±0.01	0.6±0.0	0.7±0.0	-52.9±1.7
4091	Cluster	Regular	0.33±0.01	0.3±0.1	0.5±0.0	-88.5±0.5
4099	Field	Irregular	0.38±0.01	1.2±0.1	0.8±0.0	-11.1±3.8
4267	Field	Regular	0.30±0.01	1.0±0.0	0.3±0.0	29.4±1.3
4461	Field	Regular	0.30±0.01	4.0±0.0	0.9±0.1	-83.6±1.5
4488	Field	Regular	0.35±0.01	0.6±0.1	0.5±0.0	-71.3±1.2
4645	Cluster	Regular	0.33±0.01	0.4±0.1	0.3±0.0	-0.6±0.9
4724	Field	Regular	0.68±0.22	8.0±2.0	0.3±0.0	-82.4±1.5
4746	Field	Regular	0.14±0.01	0.9±0.1	0.5±0.0	-59.2±2.7
4796	Field	Regular	0.29±0.01	0.8±0.1	0.4±0.0	85.8±1.7
4930	Cluster	Irregular	0.39±0.01	1.0±0.0	0.1±0.0	88.6±0.5
5269	Cluster	Regular	0.54±0.01	0.5±0.0	0.5±0.0	-15.9±0.8
5342	Field	Regular	0.14±0.01	1.0±0.2	0.4±0.0	10.3±2.3
5408	Cluster	Regular	0.24±0.01	1.0±0.1	0.6±0.0	-76.9±2.1
5630	Field	Regular	0.38±0.01	1.4±0.1	0.3±0.0	-34.8±0.5
5745	Cluster	Regular	0.10±0.01	2.7±0.6	0.8±0.1	-37.1±12.1
5870	Cluster	Regular	0.38±0.01	0.7±0.0	0.7±0.0	-75.8±2.1
6485	Field	Regular	0.33±0.01	1.1±0.1	0.6±0.0	89.5±0.5
6908	Field	Irregular	0.51±0.01	0.5±0.0	0.9±0.0	-15.2±2.1
6954	Field	Regular	0.24±0.01	0.6±0.1	0.3±0.0	-34.9±1.0
7137	Field	Regular	0.36±0.01	1.1±0.1	0.7±0.0	-83.6±1.7
7676	Field	Irregular	0.54±0.01	0.7±0.1	0.2±0.0	26.4±0.5
7774	Field	Regular	0.24±0.01	1.2±0.2	0.8±0.1	-52.1±10.4
7930	Cluster	Irregular	0.53±0.03	2.5±0.2	0.2±0.0	13.1±0.5
8108	Field	Irregular	0.29±0.01	1.0±0.0	0.4±0.0	-34.8±1.2
9571	Cluster	Regular	0.48±0.03	4.0±0.0	0.6±0.0	11.0±2.9

Table 3.1: Morphological measurements from F160W imaging. Reproduced by permission of the AAS.

could include both irregulars and merging objects. Conversely, regulars show no significant residuals (residual levels are less than 2 times sky levels and less than 25% the flux levels of the object) when fit with a Sérsic profile. These values were determined empirically, although small changes do not significantly change our results.

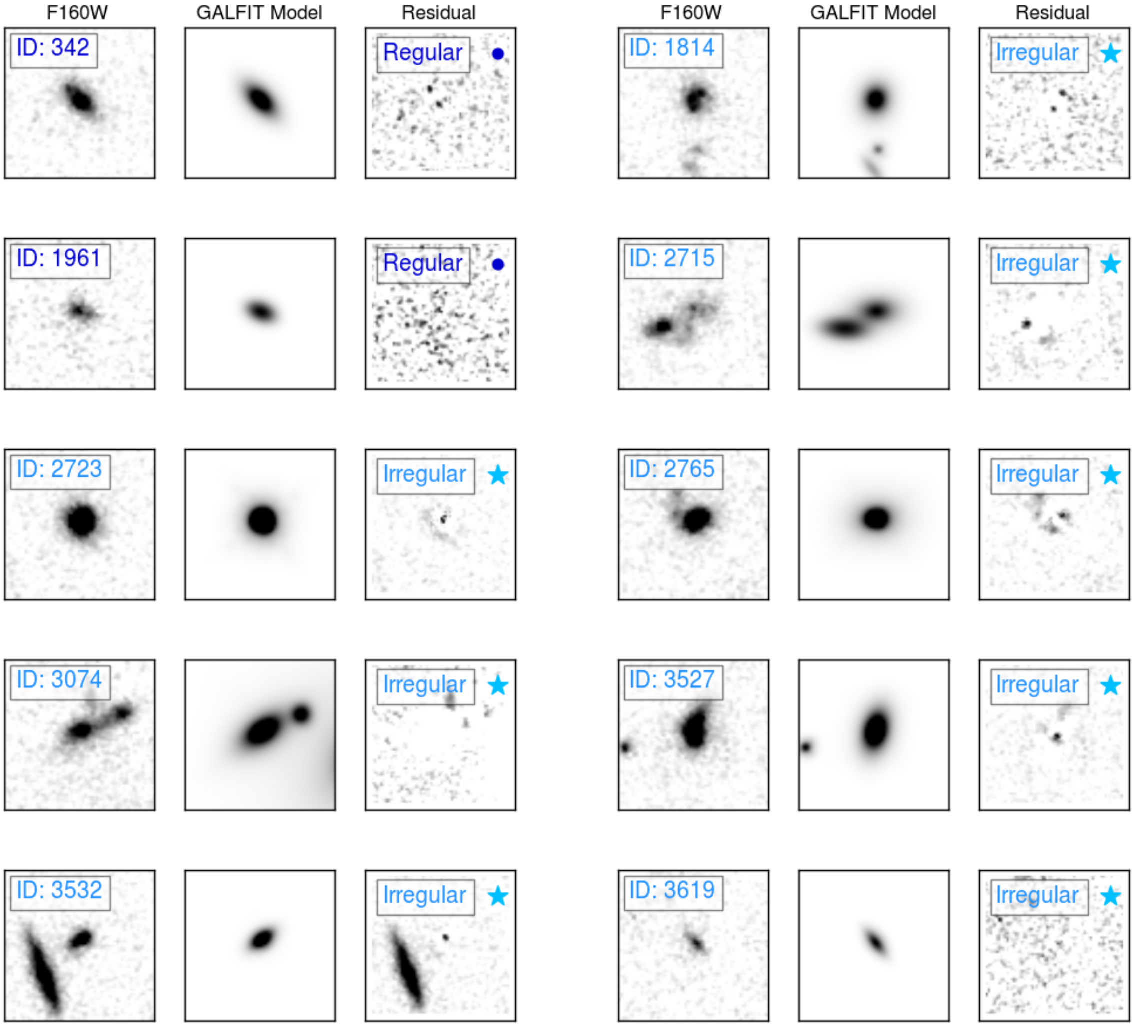

Figure 3.1: Imaging of our sample. Two galaxies are shown per row. From left for each galaxy: The F160W imaging from CANDELS/3D-HST. Center: Best-fit GALFIT model, and if the galaxy is considered "compact", it is noted. Right: Residual of the fit from the data. The residual is used to determine whether an object is regular or irregularly-shaped, and its classification is noted in this panel. Regular galaxies are in dark blue, and are plotted as dark blue circles in the text. Irregular galaxies are in light blue, and are plotted as light blue stars in the text. Compact galaxies of either classification are unfilled circles or stars. Reproduced by permission of the AAS.

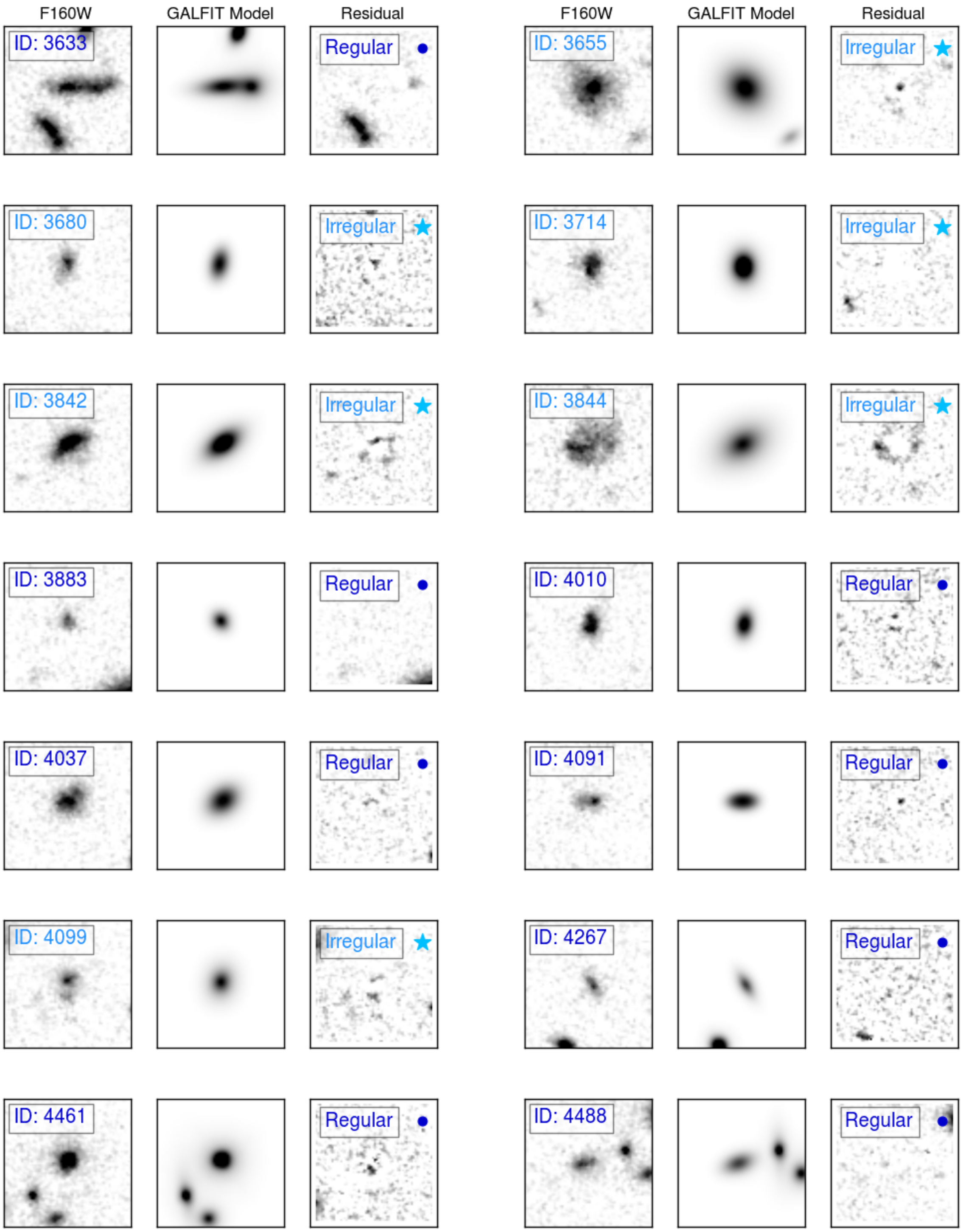

Figure 3.1 Continued. Reproduced by permission of the AAS.

In both cases, the presence of close companions was neglected in the absence of strong

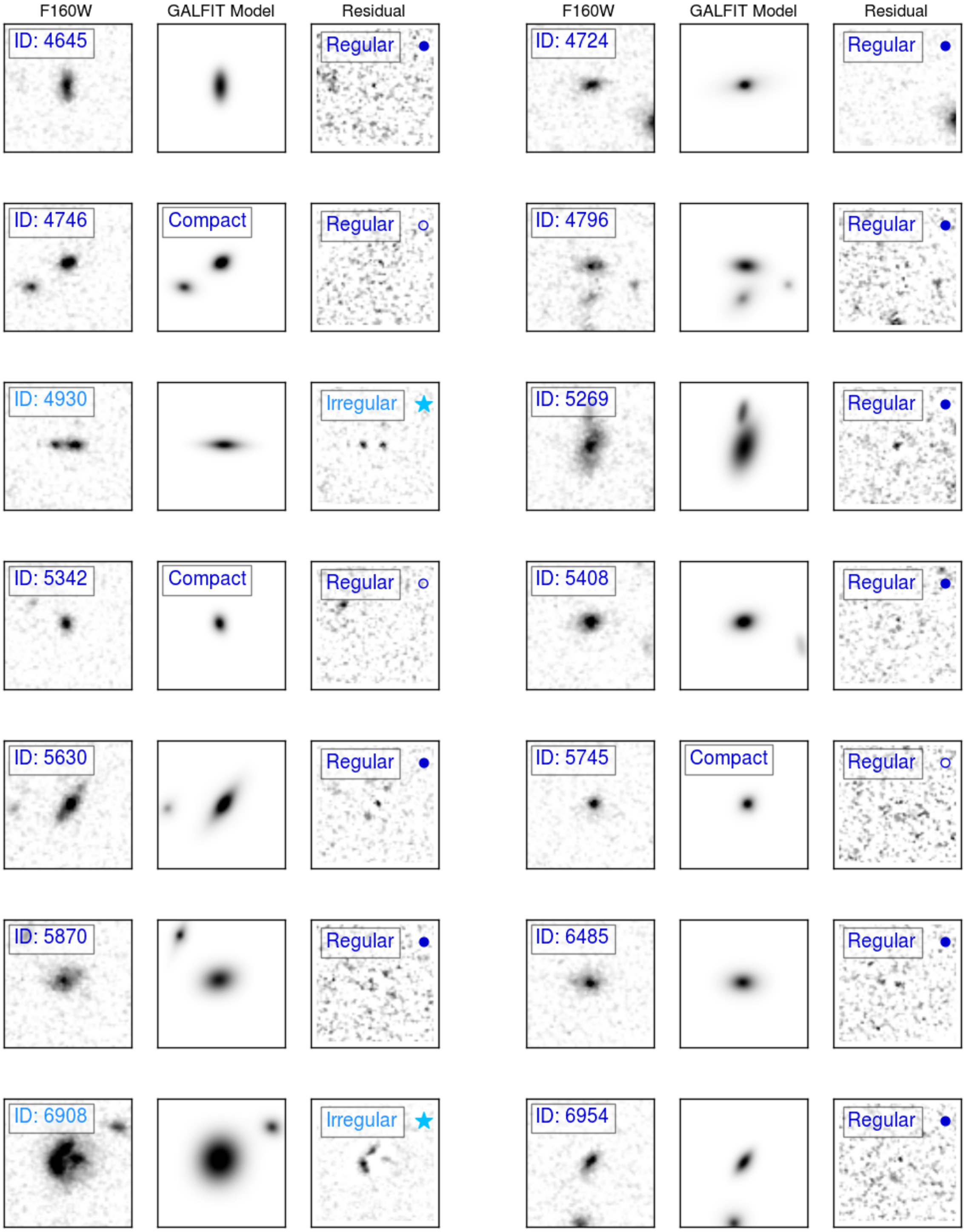

Figure 3.1 Continued. Reproduced by permission of the AAS.

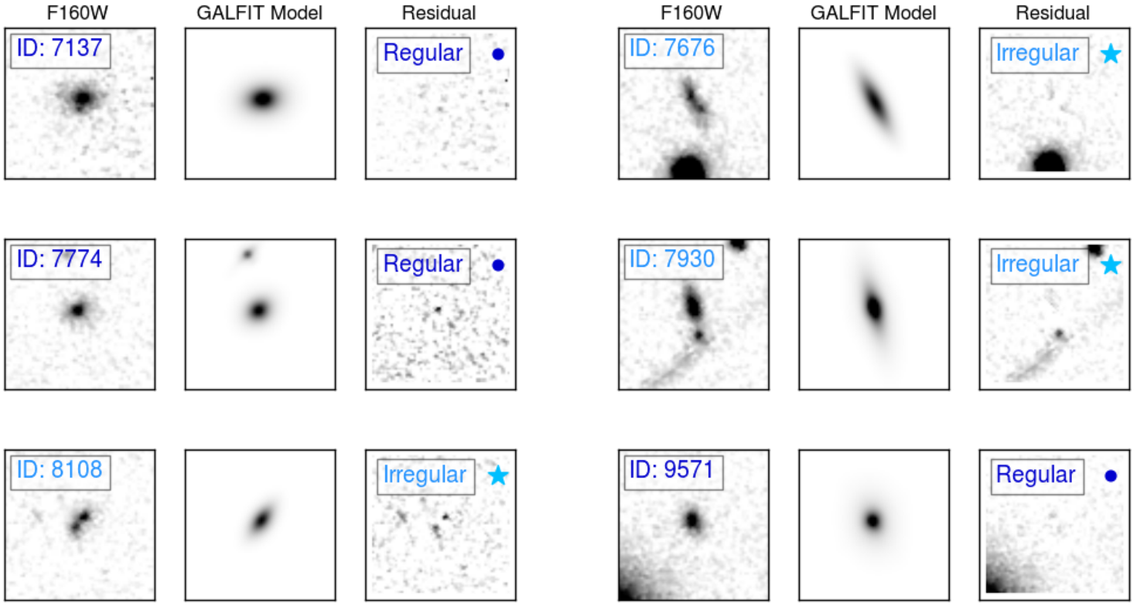

Figure 3.1 Continued. Reproduced by permission of the AAS.

residuals, as we cannot spectroscopically confirm the redshifts of nearby objects. This method is possibly biased toward classifying smaller galaxies ($< 0.3''$) as regular galaxies, because residual values are only measured in areas identified as being associated with the original object. Additionally, objects that are photometrically irregular may be kinematically regular, such as clumpy disks, and may not be distinct from regular galaxies apart from their photometry. When comparing our populations through a two-population KS test, we find a similar distribution of stellar masses from $9.0 \leq \log(\mathrm{M}_\star) \leq 11.0$ and Sérsic index from $0.2 < n < 8.0$. See Figure 3.2.

We include a category of "compactness" in our final sample, where objects with an effective radius r_e smaller than the HST F160W PSF FWHM ($r_e < 0.19''$, or 1.58 kpc at $z = 2.095$) Skelton et al. (2014) are compact. These objects are marked as unfilled points in our figures and are morphologically unresolved. From van der Wel et al. (2014) the median size of late-type galaxies at $z \sim 2$ in our M_* range is 2-4 kpc, thus we are confident that our adopted compactness threshold of 1.58 kpc is appropriate. This is in contrast to objects that are kinematically unresolved, where their diameter is less than the seeing limit (See

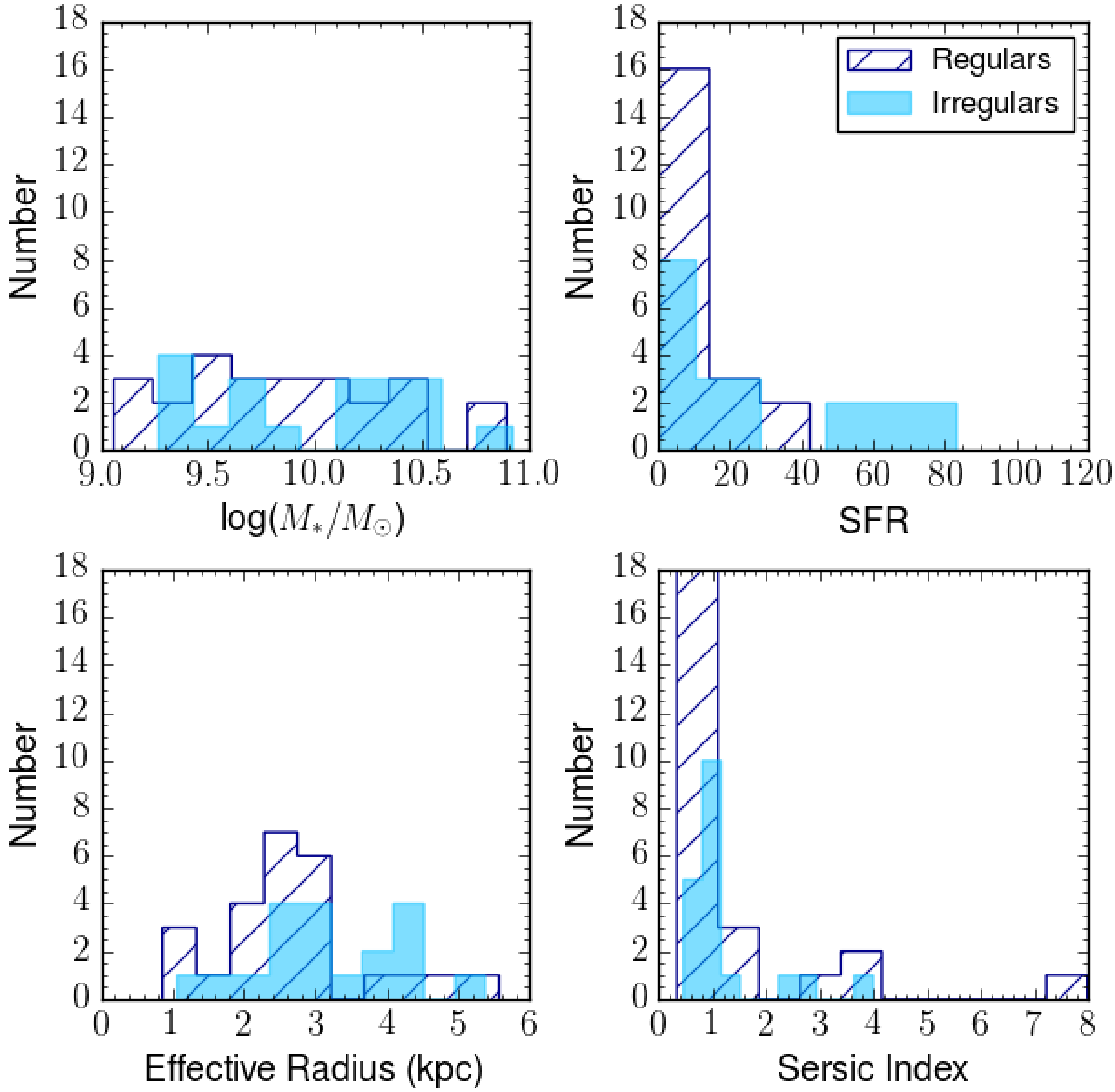

Figure 3.2: Histograms of our galaxy populations. Light blue solid bins are irregular galaxies, and dark blue hatched bins are regular galaxies. By applying a two-population KS test, we find similar properties in both populations, although irregulars are marginally more likely to have higher star-formation rates. Reproduced by permission of the AAS.

Table 3.2). 21 galaxies in this sample are kinematically unresolved. The velocity of these unresolved sources is often underestimated (Newman et al., 2012), but we include compact objects with reliable velocity measurements (Section 3.2.2).

3.2.3 MOSFIRE NIR Spectroscopy

Observations were taken in December 2013 and February 2014 in the K-band filter covering 1.93-2.45 μm, the wavelength range we would expect to see Hα and [N II] at the cluster redshift. Seeing varied from $\sim 0.4''$ to $\sim 1.3''$ over the course of our observations.

The spectra are flat-fielded, wavelength calibrated, and sky subtracted using the MOSFIRE data reduction pipeline (DRP)[‡]. A custom ZFIRE pipeline corrected for telluric absorption and performed a spectrophotometric flux calibration using a type A0V standard star. We flux calibrate our objects to the continuum of the standard star, and use ZFOURGE photometry as an anchor to correct offsets between photometric and spectroscopic magnitudes. The final result of the DRP are flux-calibrated 2D spectra and 2D 1σ images used for error analysis. For more information on ZFIRE spectroscopic data reduction and spectrophotometric calibrations, see Nanayakkara et al. (2016). 1D spectra and catalogs are available to the public on the ZFIRE website.

From spectroscopic observations, we reject objects with only one identified emission line, without morphological measurements, or with AGN signatures (Cowley et al., 2016), leaving 92 SFGs with K band spectroscopy.

3.2.4 PSF Fitting

The assumed PSF for an observation plays a role in the recovery of accurate velocities, as the mischaracterization of the shape of the PSF can result in an underestimation of the velocity. In most cases, a Gaussian PSF with a FWHM given by seeing conditions is convolved with the emission-line fit, but in recent work it has been shown that on the MOSFIRE instrument, a Moffat profile is a better fit to the PSF (Straatman et al., 2017). Therefore we fit and apply Moffat PSFs to all objects in our sample.

To determine our PSF, we create a 2D Moffat-profile simulated star. We collapse this star into a flat spectral profile and sum along the wavelength component to estimate the spatial

---

[‡] http://keck-datareductionpipelines.github.io/MosfireDRP/

1D profile of the star, and subtract the profile on either side of the peak at the positions of our dithering pattern ($1.25''$) to correctly account for any effect of the dither pattern on the wings of the PSF. Then for each observed mask, we sum along the wavelength plane to determine the spatial profile of our flux monitor star. We leave the Moffat parameters α and β free and fit the Moffat profile given as

$$PSF(r) = \frac{\beta - 1}{\pi\alpha^2}\left[1 + \left(\frac{r}{\alpha}\right)^2\right]^{-\beta}, \tag{3.1}$$

to our observed flux monitor stars, and use the best-fit values for the Moffat parameters to apply to our Moffat convolution kernel when we fit our emission lines. If the wings of the best-fit Moffat profile appear to over-fit the observed star, we fix $\beta = 2.5$ and refit to find α. The best fit Moffat parameters used to generate our emission line models can be seen in Table 3.2.

Date	Mask Name	Average Seeing (")	α	β	PA (degrees)
Dec 2013	Shallowmask1	0.7	0.601	2.487	134
Dec 2013	Shallowmask2	0.68	0.581	2.5	-47.3
Dec 2013	Shallowmask3	0.7	0.674	2.778	14.8
Dec 2013	Shallowmask4	0.67	0.516	2.574	-63
Feb 2014	DeepKband1	1.27	1.031	2.5	2
Feb 2014	DeepKband2	0.7	0.656	2.599	-62
Feb 2014	KbandLargeArea3	1.1	1.021	2.5	59
Feb 2014	KbandLargeArea4	0.66	0.489	2.525	2

Table 3.2: Properties and best-fit Moffat parameters of the ZFIRE observations and slit masks. PA is defined as east of north. Reproduced by permission of the AAS.

3.3 Methods

3.3.1 Spectroscopic Fitting Method

Our fitting procedure for our sample and our simulated observations are based around HELA (Heidelberg Emission-Line Algorithm), which was developed by C.M. Straatman. Information on the models generated by HELA is located in Appendix A.

We emphasize that there are many ways to refer to the velocity of a galaxy. In this text, we refer to velocity in three main ways. $V_{rot}(r)$ is the rotational velocity at a given radius of a galaxy, referred to as simply the rotational velocity in this text. This is in contrast to V_t, which is the asymptotic velocity (at the flat part of the rotation curve). Additionally we use $V_{2.2}$, which is the velocity at $2.2r_s$, where the rotation curve of an ideal disk peaks (Freeman, 1970), and is used widely in literature as a common reference point for velocity (Miller et al., 2011).

To determine best-fit parameters for our emission line, our procedure is thus:

1. Identify the position of the Hα emission line. Subtract continuum values if present (see Section 3.3).

2. Mask wavelengths which are strongly contaminated by sky emission in the observed spectra, or which are bad pixels.

3. Determine fitting bounds: -600 km s^{-1}< V_t < 600 km s^{-1}, 10 km s^{-1}< σ_g < 150 km s^{-1}, 0.1$''$ < r_s < 1$''$, and 0.03$''$ < r_t < r_s (we also perform fitting where r_t is fixed to $r_t = 0.33r_s$ or $r_t = 0.4r_s$). Position of the intensity peak cannot shift more than three pixels from given coordinates. These values and the intensity are all free parameters.

4. Run the simulated emission line through HELA (see Appendix) to derive best-fit parameters. We use a Markov-Chain Monte-Carlo analysis (MCMC) initializing 30 walkers over 1000 steps. Our walkers are initialized as a clump, values randomly distributed around the given wavelength and spatial position, and initial guess for V_t, σ_g, $r_s = r_e/1.678$ (where r_e is the effective radius measured from GALFIT), and $r_t = 0.3r_s$, or r_t fixed. We use the Python package emcee for our MCMC algorithm[§] (Foreman-Mackey et al., 2013).

[§] http://dan.iel.fm/emcee/current/

5. Discard the first 200 iterations out of a total of 1000 - where the MCMC algorithm tends to be far from convergence. Our best-fit model is taken to be the median of the posterior likelihood output of all our free parameters after convergence, and errors are the 16th and 84th percentiles of the walkers. The value for $V_{2.2}$ is determined by fitting the velocity curve function (Equation B.1) to each walker and step, and then measuring the median value.

6. In the case of multiple peaks in the posterior likelihood, we isolate one peak and fit a Gaussian to the largest peak to determine the best-fit values. Errors on the fit are determined from the σ value on this Gaussian fit.

We reject four compact galaxies with errors greater than $0.8V_{2.2}$ where $V_{2.2}> 35$ km s^{-1}, which are considered unreliable. Six morphologically resolved galaxies with similar kinematics were kept in the sample and are shown as upper limits on the TFR.

3.3.2 Fitting ZFIRE Data

Our fitting algorithm is applied to the 2D telluric and spectrophotometrically corrected emission lines. Faint continua are seen in a small number of objects, so we subtract a flat continuum when one is detected. Continuum subtraction is performed in the same method as Straatman et al. (2017). Summarized, for each row of pixels in a stamp 300 wide, we determine a median flux with outlier pixels $> 2.5\sigma$ above the median rejected, and any sky or Hα [N II] emission masked. This procedure is repeated a total of three times, then the median values are subtracted from each row.

The measured axis ratio from GALFIT is used to determine the inclination for use in our fitting procedure:

$$\sin i = \sqrt{\frac{1-q^2}{1-q_0^2}}, \tag{3.2}$$

where $q_0 = 0.19$ (Miller et al., 2011). 40 objects with galaxy PA-slit offset $\Delta\alpha > 45^o$ or $\Delta\alpha < -45^o$, where PA is determined from GALFIT modeling, are rejected from the final sample, although objects with large PA uncertainties (mostly objects with low inclination or high q) that could overlap within this range are not rejected. We also reject objects with significant sky emission (3 objects where more than 50% of the line is masked, Appendix B.1) or where SNR < 5 (5 objects).

3.4 Results

Our final sample consists of 44 galaxies within $-45^o < \Delta\alpha < 45^o$ and with less than half the emission line masked and SNR > 5. See Table 3.3 for all kinematic fit values. 14 of these objects are associated with an over-density at $z = 2.095$, and 30 are field objects. Due to the small number of cluster objects in our sample, as well as the lack of 1D environmental distinctions in this sample (Alcorn et al., 2016), we do not include any environmental analysis in this work. We identify 25 regular-type galaxies in our sample, and 19 galaxies which could include both merging galaxies and irregular galaxies - anything that is not well-described by a Sérsic profile. Wisnioski et al. (2015) determines a disk fraction of 58% at $z \sim 2$, similar to our estimated disk (regular) fraction (56.8%) determined from measuring the residual values after subtracting a Sérsic fit.

ID	Date	Mask	z_{spec}	M_*	SFR	$V_{2.2}$	σ_g	j_{disk}
1814	feb2014	KbandLargeArea4	2.17	9.76	14.6	108.44±13.19	66.19±3.55	321.87±39.63
1961	feb2014	KbandLargeArea3	2.31	9.79	N/A	90.85±46.57	103.72±8.78	241.22±123.8
2715	dec2013	mask2	2.08	9.88	13.7	119.38±5.98	55.18±4.51	555.5±30.6
2723	dec2013	mask2	2.09	10.92	N/A	406.46±16.23	96.47±37.72	717.42±616.43
2765	dec2013	mask1	2.23	10.44	83.3	193.38±4.42	80.17±2.42	1227.22±46.26
3074	dec2013	mask1	2.23	10.19	N/A	186.93±9.12	63.69±9.9	879.78±45.46
342	feb2014	KbandLargeArea4	2.15	10.42	31.3	218.5±3.04	28.66±2.65	823.63±15.56
3527	feb2014	KbandLargeArea4	2.19	10.38	56.1	151.4±1.39	64.26±1.65	579.59±7.11
3532	dec2013	mask1	2.1	9.4	9.9	3.57±4.8	40.39±1.31	7.27±9.77
3619	feb2014	KbandLargeArea3	2.29	9.27	3.3	32.43±20.07	41.56±6.78	81.71±50.66
3633	dec2013	mask1	2.1	10.4	42.4	315.97±8.34	33.83±11.64	1887.98±68.03
–	feb2014	DeepKband2	2.1	10.4	42.4	211.17±2.87	34.27±1.88	1261.76±35.41
3655	feb2014	KbandLargeArea3	2.13	10.35	17.7	185.23±6.35	40.64±3.43	1008.2±37.63
3680	dec2013	mask3	2.18	9.32	5.0	209.49±9.65	14.38±6.1	689.72±36.88
3714	dec2013	mask3	2.18	10.17	66.3	184.03±8.43	72.01±3.47	590.34±27.06
3842	dec2013	mask1	2.1	10.25	8.8	206.85±7.2	19.19±9.42	904.32±33.96
3844	feb2014	DeepKband2	2.44	10.44	N/A	248.01±6.05	38.03±6.42	1655.84±55.51
3883	dec2013	mask3	2.3	9.12	2.9	87.01±24.22	32.9±13.64	169.18±47.63
4010	feb2014	KbandLargeArea4	2.22	10.07	N/A	105.24±7.93	100.06±4.04	295.17±22.75
4037	dec2013	mask2	2.17	10.77	N/A	307.45±11.23	28.65±9.45	1156.14±45.06
4091	dec2013	mask1	2.1	9.4	3.6	133.45±36.72	62.65±13.94	425.12±117.36
4099	dec2013	mask3	2.44	10.28	N/A	119.92±8.5	16.67±10.01	472.09±37.65
4267	feb2014	KbandLargeArea3	2.41	10.14	N/A	128.02±19.22	46.88±19.41	388.38±59.6
4461	feb2014	DeepKband2	2.3	10.89	10.2	63.69±45.49	101.6±7.37	351.76±251.73
4488	dec2013	mask2	2.31	10.21	7.8	13.41±23.53	126.4±10.4	46.35±81.35
4645	feb2014	DeepKband1	2.1	9.53	5.5	154.04±7.65	13.71±5.65	488.73±25.11
4724	dec2013	mask2	2.3	9.54	3.1	1.42±18.89	56.5±4.74	42.13±561.56
4746	dec2013	mask4	2.18	9.54	6.1	28.37±45.49	56.59±6.91	40.63±65.17
–	feb2014	DeepKband2	2.18	9.54	6.1	58.66±47.28	43.72±5.9	84.02±67.76
4796	feb2014	DeepKband2	2.17	9.45	6.6	30.02±36.87	89.7±7.13	88.28±108.46

Table 3.3: Kinematic measurements of ZFIRE galaxies using HELA. SFR is determined from the Hα flux and corrected for dust assuming a Calzetti et al. (2000) dust law. Reproduced by permission of the AAS.

ID	Date	Mask	z_{spec}	M_*	SFR	$V_{2.2}$	σ_g	j_{disk}
4930	feb2014	DeepKband2	2.1	9.46	7.2	110.08±12.99	40.05±8.31	438.98±52.75
5269	dec2013	mask3	2.11	10.03	13.7	176.48±6.07	25.23±6.27	928.94±34.88
5342	dec2013	mask3	2.16	9.06	2.5	84.3±13.09	54.48±8.77	119.25±18.9
5408	dec2013	mask4	2.1	9.74	20.9	180.32±7.71	23.24±17.28	442.28±21.42
5630	feb2014	KbandLargeArea4	2.24	9.97	23.6	179.28±9.08	61.15±3.8	733.62±40.15
5745	feb2014	DeepKband2	2.09	9.15	8.6	41.15±14.31	60.86±2.79	60.21±21.35
5870	dec2013	mask4	2.1	9.9	7.8	118.68±5.07	23.47±3.97	444.18±21.64
6485	dec2013	mask2	2.16	10.41	17.1	182.66±6.08	67.17±6.05	619.32±29.24
6908	feb2014	DeepKband2	2.06	10.47	59.9	395.94±8.19	14.55±6.5	1985.46±43.6
6954	feb2014	DeepKband1	2.13	9.25	6.7	13.28±12.42	17.29±6.82	32.11±30.04
7137	dec2013	mask2	2.16	9.85	9.3	17.32±19.15	83.12±2.37	64.45±71.27
7676	dec2013	mask3	2.16	9.4	4.4	76.67±5.14	39.34±4.75	416.2±29.36
7774	feb2014	DeepKband1	2.2	10.17	10.9	111.81±50.62	95.29±10.76	278.55±126.33
7930	dec2013	mask3	2.1	9.69	8.2	68.3±2.32	58.92±1.79	492.14±28.89
8108	dec2013	mask2	2.16	9.67	6.1	167.71±5.73	48.6±7.88	502.34±23.26
9571	dec2013	mask3	2.09	9.7	7.8	97.75±42.2	66.87±12.8	876.68±383.16

Table 3.3 Continued. Reproduced by permission of the AAS.

3.4.1 Measured Kinematic Scaling Relations

We derive a best fit linear relation using the Levenberg - Marquardt algorithm for the TFR of the form

$$\log(V_{2.2}) = A\log(M_*/M_\odot - 10) + B, \tag{3.3}$$

weighted by the errors on $V_{2.2}$ (Figure 3.3, left). We reject objects greater than 3σ from the fit, and iterate the fit until the process converges. Ranges on the fitting parameters are determined by bootstrapping the sample 1000 times. In the case where A and B are both free parameters of the linear fit, we derive $A = 0.29 \pm 0.1$ and $B = 2.19 \pm 0.04$ for the total sample. The irregular and regular populations are offset by 0.08 dex. Scatter in all populations is high, at 0.5 ± 0.02 dex for the total sample, 0.6 ± 0.02 for regulars, and 0.39 ± 0.03 for irregulars. Given this high level of scatter, we do not think our offsets are significant. There are a number of low-mass objects that are significantly offset from the relation - these are the compact galaxies that could have underestimated velocities (Newman et al., 2012).

To compare our values for the TFR to literature values, in particular to determine a possible offset to local relations and IFU observations, we hold $A = 0.29$, determined by Reyes et al. (2011) for the local TFR. We derive an offset of $\Delta M/M_\odot$=-0.34±0.22 from local relations. See Table 3.4 for all linear fits.

In both free and fixed slope cases, we do not find any statistically significant difference between irregulars and regulars. Our results for the TFR do not change if we remove compact objects from our fitting.

In addition, given the values of both $V_{2.2}$ and σ_g, we derive a best-fit relation for $S_{0.5}$, defined in Kassin et al. (2007) as $S_{0.5} = \sqrt{0.5V_{2.2}^2 + \sigma_g^2}$. This equation is derived from a combined velocity scale S_K Weiner et al. (2006), $S_K^2 = KV_{rot}^2 + \sigma^2$, where K is a constant $<$ 1. Where rotation curves have been measured, $K = 0.3 - 0.5$, consistent with the prediction for an isothermal potential and a flat rotation curve. This suggests that S_K is a good tracer

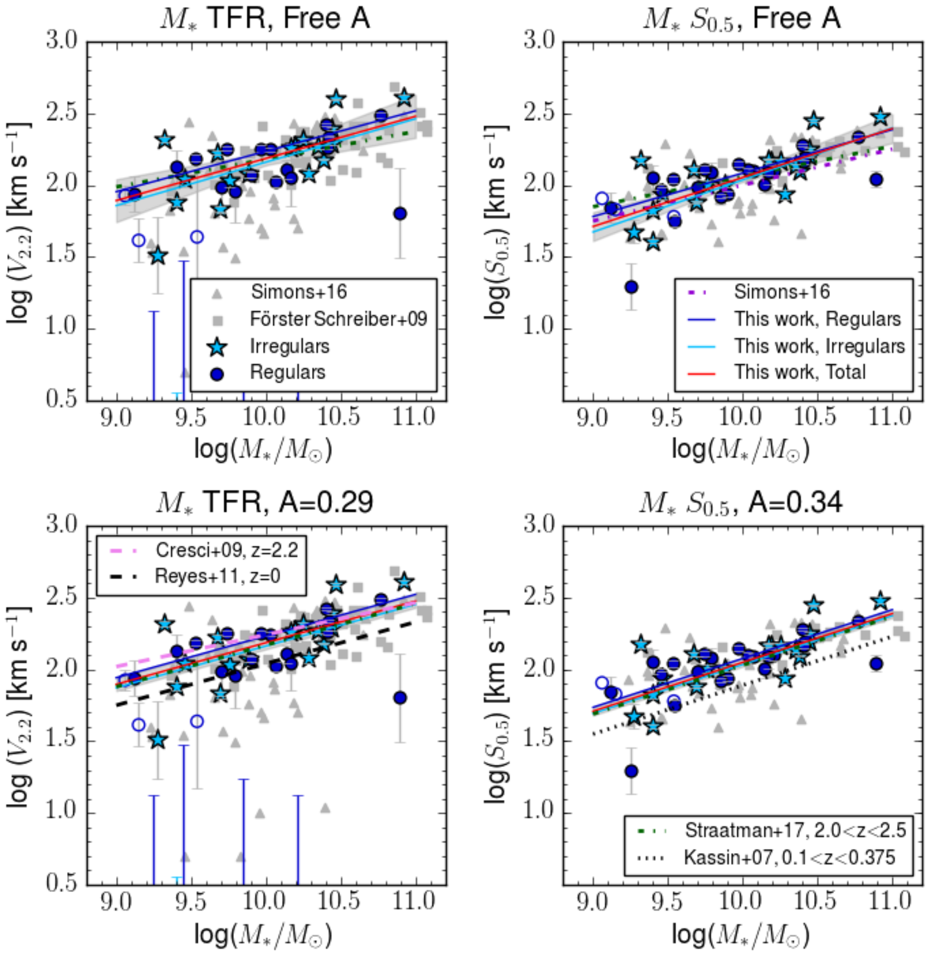

Figure 3.3: Kinematic scaling relations of the ZFIRE sample. Irregular galaxies are light blue stars, and the linear fit to irregular galaxies is the light blue line. Regular galaxies are dark blue circles, and the fit is the dark blue line. Compact galaxies of either population are unfilled circles or stars. Galaxies with unreliable velocity measurements are shown as upper limits. The best-fit linear relation to the total sample is the solid red line, and the grey shaded regions show the uncertainty in the best-fit line. The best-fit lines from Straatman et al. (2017) are the green dashed line. Upper Left: The stellar-mass TFR. We compare to the SIGMA sample (grey triangles) (Simons et al., 2016) and the SINS data points (grey squares) (Förster Schreiber et al., 2009). Lower Left: As upper left, with slope fixed to $A = 0.29$ for consistency with the $z = 0$ TFR (black dashed) (Reyes et al., 2011) and the SINS IFU survey (pink dashed) (Cresci et al., 2009). Upper Right: The stellar-mass $S_{0.5}$ relation from Kassin et al. (2007), which includes the contribution of σ_g to the total kinematics of the system, and a comparison to Simons et al. (2016). Lower Right: Slope is fixed to $A = 0.34$. We compare to their relation at $0.1 < z < 1.2$ and find an offset of 0.16±0.04 dex higher $S_{0.5}$ at a given stellar mass. Reproduced by permission of the AAS.

Population	x	y	A	B	B, fixed A	σ_{RMS}	N
Total	M_*	$V_{2.2}$	0.29±0.1	2.19±0.04	2.19±0.04	0.5±0.02	44
Regulars	M_*	$V_{2.2}$	0.28±0.07	2.24±0.03	2.23±0.02	0.6±0.02	25
Irregulars	M_*	$V_{2.2}$	0.3±0.15	2.16±0.06	2.16±0.06	0.39±0.03	19
Total	M_*	$S_{0.5}$	0.38±0.07	2.04±0.03	2.05±0.03	0.15±0.01	44
Regulars	M_*	$S_{0.5}$	0.31±0.05	2.08±0.02	2.08±0.02	0.16±0.01	25
Irregulars	M_*	$S_{0.5}$	0.43±0.1	2.01±0.04	2.03±0.04	0.16±0.01	19
Total	M_*	j	0.36±0.12	2.8±0.05	2.72±0.07	0.52±0.02	44
Regulars	M_*	j	0.39±0.11	2.8±0.05	2.73±0.06	0.56±0.03	25
Irregulars	M_*	j	0.33±0.20	2.81±0.07	2.71±0.11	0.48±0.05	19

Table 3.4: Values for all weighted least-square linear fits to the stellar-mass Tully-Fisher Relation and $S_{0.5}$ Relation and j-$M_\star$ Relation, of the form $\log(y) = A(\log(x) - 10.) + B$. Objects more than 3σ away from the fits are rejected from the fits to minimize the influence of outliers. Fixed values are $A = 0.29$ for the TFR, $A = 0.34$ for $S_{0.5}$, and $A = 0.67$ for j. Reproduced by permission of the AAS.

for the gravitational potential, and for consistency with the literature we use $K = 0.5$.

When we derive our equation of the form $\log(S_{0.5}) = A\log(M/M_\odot - 10) + B$ to the data, we find best fit parameters of 0.38 ± 0.07 and 2.04 ± 0.03 (Figure 3.3, Right). When we fix $A = 0.34$ (seen in $0.1 < z < 1.2$ from Kassin et al. (2007)) we measure $B = 2.05 \pm 0.03$. Scatter in all populations decreases significantly when we include the contribution of σ_g to the total kinematics (from 0.5 dex for the TFR to 0.15 dex for $S_{0.5}$). Kassin et al. (2007) derives a scatter of 0.16 dex in $S_{0.5}$ for $0.1 < z < 1.2$, similar to Price et al. (2016) who find a scatter of 0.17 dex at $1.4 < z < 2.6$. Straatman et al. (2017) finds consistent values with these at $2.0 < z < 2.5$ (0.15 dex), using 22 galaxies drawn from the same ZFIRE sample as this paper, 20 of which are in common with our sample. Our offset implies a zero-point evolution of $\Delta M/M_\odot$=-0.47±0.14.

When we hold $r_t = 1/3r_s$ and $r_t = 0.4r_s$, we find our results for both the $M_\star$-TFR and $S_{0.5}$ do not significantly change. Our simulated MOSFIRE observations (Appendix B), show that we tend to overestimate our values for $S_{0.5}$ to a median offset of ~10% (Figure B.3, top two rows). However, this offset is stable for SNR>10 and less than half the emission line masked (see Appendix B.1), indicating our $S_{0.5}$ values are reliable.

The $V_{2.2}/\sigma_g$ parameter derived from $V_{2.2}$ and σ_g is an instructive measurement for determining the amount of rotational dominance in integrated kinematics. Higher $V_{2.2}/\sigma_g$ indicates a well-ordered rotating disk with minimal random motion within the disk, whereas lower $V_{2.2}/\sigma_g$ signals a stronger presences of random motion. In Förster Schreiber et al. (2009); Wisnioski et al. (2015); Turner et al. (2017) galaxies are considered rotation-dominated at $V_{2.2}/\sigma_g > 1$ and pressure-dominated at $V_{2.2}/\sigma_g < 1$. Within our sample we observe both pressure-dominated and rotation-dominated galaxies.

We see a highly scattered trend between $M_\star$ and $V_{2.2}/\sigma_g$, where objects with smaller $M_\star$ are more likely to have log($V_{2.2}/\sigma_g$)< 0 (Figure 3.4). We can see a clear trend in all populations of increasing rotation support at increasing stellar mass. In Figure 3.5 we can see this is not due to a decrease in pressure support at high mass, as σ_g values are unrelated to the stellar mass of a galaxy. Scatter is large for all populations, 0.67 ± 0.04 dex for irregulars and 0.53 ± 0.01 dex for regulars. The median values of $V_{2.2}/\sigma_g$ for regular and irregular galaxies were 1.55 and 2.75, respectively, but given high levels of scatter in both populations, it is unclear if this difference is significant. The median value of $V_{2.2}/\sigma_g$ for the total sample was 2.48. Again, our results are not significantly affected by holding r_t to a fixed position relative to r_s.

Our MOSFIRE simulations (Appendix B) show difficulty in recovering $V_{2.2}/\sigma_g$ using slit spectroscopy. In the bottom two panels of Figure B.3, we see that we tend to overestimate $V_{2.2}/\sigma_g$ values by 25% of the input, with scatter of around 20%. This leads us to believe our values could be unreliable and could be related to the heavy scatter in our measured values for $V_{2.2}/\sigma_g$.

We notice a slight difference between the regular and irregular populations in recovered σ_g, where regulars are more likely to have high values of σ_g than irregulars (Figure 3.5). A logistic regression analysis was inconclusive.

Using our environmentally-diverse sample, our findings are consistent with the results of Simons et al. (2016). In all populations, at low stellar mass, we see evidence of less rotational support. As stellar mass increases, SFGs have increasing amounts of rotational support, no

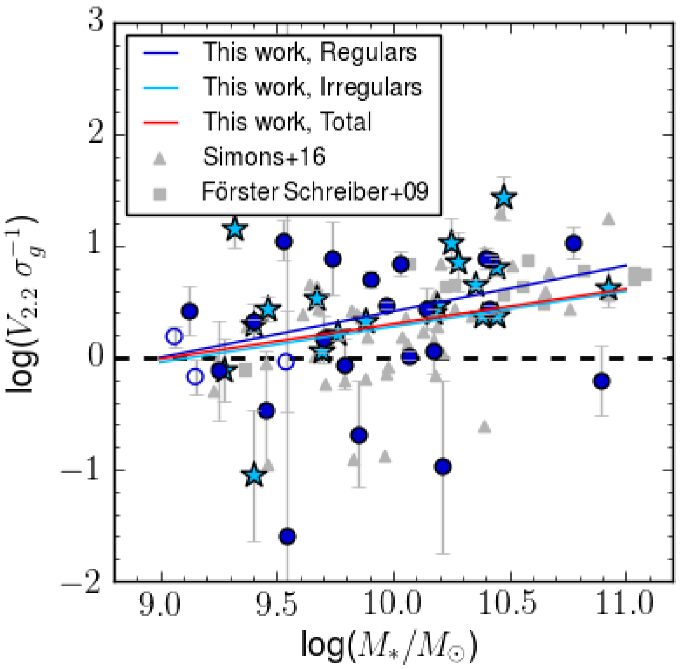

Figure 3.4: $V_{2.2}/\sigma_g$ of galaxies in the ZFIRE sample, showing the ratio of rotational support (measured at $V_{2.2}$) and σ_g, pressure support. We find consistent values between regulars and irregulars, and a clear relation between the rotational support and stellar mass. Colors and markers are as described in Figure 3.3. The black dashed line shows equal rotation and pressure support. Reproduced by permission of the AAS.

matter their morphology. Despite the large scatter in recovery of simulated $V_{2.2}/\sigma_g$, we can still observe a relation between rotational support and stellar mass.

3.4.2 Comparison to Disk-Formation Models

Krumholz et al. (2018) introduces a mathematical model for the evolution of gas in the disks of SFGs, which attempts to explain the nature of gas turbulence in these disks. According to this model, gas turbulence can be fed through star formation feedback, radiative transport, or both. The underlying prediction is that in gravitationally unstable galaxies, instability-driven mass transport will move mass inward toward the galaxy center until stability is restored. In this model, disks are never more than marginally gravitationally unstable, and maintain a balance between turbulence driven by star-formation feedback and gravitational instability and the dissipation of turbulence. It predicts that at high redshift,

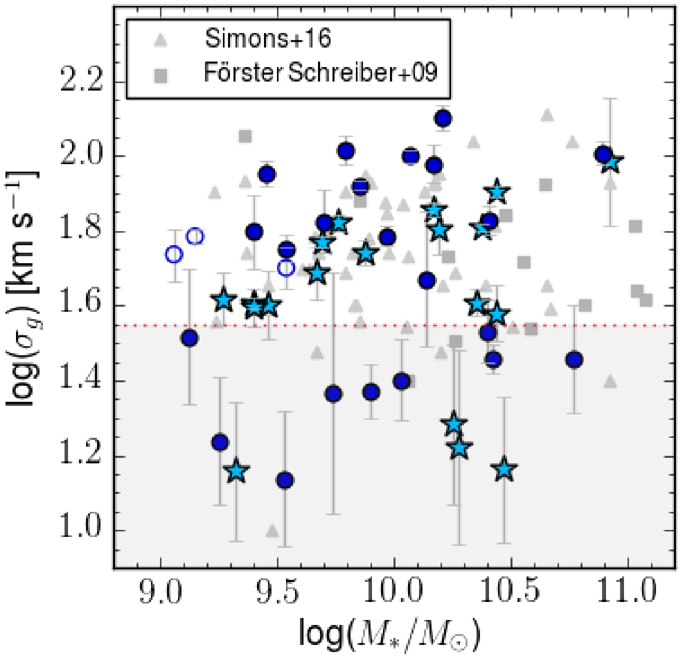

Figure 3.5: σ_g plotted against $M_\star$, values as determined by HELA models. Colors and markers are as described in Figure 3.5. Areas below MOSFIRE instrumental resolution are shown in the shaded region, marked by the red dotted line. Reproduced by permission of the AAS.

turbulence is mostly gravitationally-driven, whereas in local disks there is a minimum floor of σ_g ($\sim 6-10$ km s^{-1}) where the disks settle that is driven by star-formation feedback.

Our values for σ_g are determined through modeling with HELA, and our star-formation rates (SFR) are determined from dust-corrected Hα flux, assuming a Calzetti et al. (2000) dust law (Tran et al., 2017). In Figure 3.6, we compare these values to four theoretical models created assuming properties described in Krumholz et al. (2018): a local dwarf (fraction of the ISM in the star-forming phase [f_{sf}] = 0.2, rotational velocity at 100km s^{-1}), a local spiral (f_{sf} = 0.5, rotational velocity at 200km s^{-1}), a high-redshift galaxy (f_{sf} = 1.0, rotational velocity of 200km s^{-1}), and an Ultra-Luminous InfraRed Galaxy (ULIRG, f_{sf} = 1.0, rotational velocity of 300km s^{-1}). Our sample maintains a similar shape to the high-z and ULIRG models, but SFRs are lower, perhaps indicating that smaller SFRs can drive turbulence in high-z objects. However, this is consistent with the other high-z observations seen in the text and plotted in Figure 3.6 (Epinat et al., 2008, 2009; Förster Schreiber et al., 2009; Law et al., 2009; Jones et al., 2010; Green et al., 2014; Wisnioski et al., 2015; Stott et al., 2016; Di Teodoro et al., 2016).

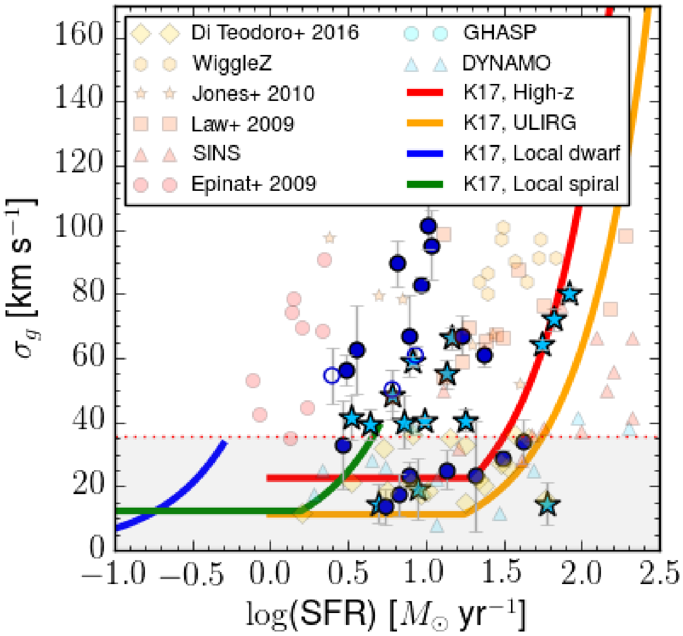

Figure 3.6: Relationship of our modeled σ_g values against dust-corrected Hα star-formation rate from Tran et al. (2017). We compare our results to the models derived in Krumholz et al. (2018) for local disks and high-z disks. Local and high-z samples with Hα SFRs featured in Krumholz et al. (2018) are also shown here. Reproduced by permission of the AAS.

The model calculated for a local disk assumes that the dispersion is driven mostly by star-formation feedback, and the ULIRG and high-z models are driven primarily by mass transfer to the core of the galaxy. In this case, it could show that there is more turbulence driven by star formation feedback and mass transfer plays less of a role in high-z galaxies than predicted. Krumholz et al. (2018) assumes these objects are disks and are never more than marginally unstable. The offset of these galaxies from these predictions could mean these objects are unstable and are possibly not even disks. Instead turbulence may be driven at least partially by external factors such as a recent merger or disk instabilities caused by rapid gas accretion.

3.4.3 Angular Momenta of SFGs at $z \sim 2$

Using the maximum rotational velocity (assuming ideal disks, this is $V_{2.2}$), and scale radius, we can estimate specific angular momenta of our galaxies given the formula:

$$j_{disk} = K_n r_s V_{2.2}, \tag{3.4}$$

where j_{disk} is the specific angular momentum (angular momentum per solar mass), and K_n is defined as

$$K_n = 1.15 + 0.029n + 0.062n^2, \tag{3.5}$$

where n is the Sérsic index of the galaxy (Romanowsky and Fall, 2012). We recognize that in the case of galaxies with complex kinematics and morphological structure, that r_s may not be the best representation of the disk radius, but to obtain a consistent sample we apply this to all galaxies.

Generally angular momentum measurements are taken using IFU spectroscopy. As such, our results may not be the same as what would be measured in an IFU survey. We hope to follow these results up with IFU observations of some of these objects, to determine if the 3D data-cube fitting method yields more accurate measurements of j_{disk} than traditional velocity curve-fitting methods for slit spectroscopy. Despite this disclaimer, our simulated slit observations (Appendix B) demonstrate that we can reliably recover our input j_{disk} to within an offset of -5% (Figure B.4). This small offset from our input is consistent over all simulated $\Delta\alpha$, inclination, and sizes, and only becomes unreliable at line masking $> 50\%$ and SNR<10.

Additionally, we assume that the angular momentum of the gas disk traces the angular momentum of the stellar disk and older stellar populations. Local kinematic studies usually make this assumption due to the difficulties of measuring the angular momentum of stellar populations (Romanowsky and Fall, 2012; Obreschkow and Glazebrook, 2014), and these difficulties increase at high redshift. Simulations show that the stellar disk rotates slower than the gaseous disk in late-type galaxies (El-Badry et al., 2018). In contrast, some observational studies of spatially resolved low-redshift clumpy star-forming disks show that the ionized gas and stellar kinematics are coupled (Bassett et al., 2014). The validity of our assumption is still under debate, but for consistency with local kinematic surveys we apply this assumption.

In Figure 3.7, left panel, we see our estimated j_{disk} compared to lower-redshift observations. We note a shallower slope than Romanowsky and Fall (2012) at $z = 0$ and KROSS (Harrison et al., 2017) ($z = 0.9$). For the total population, we find a slope of 0.36 ± 0.12 and intercept of 2.80 ± 0.05.

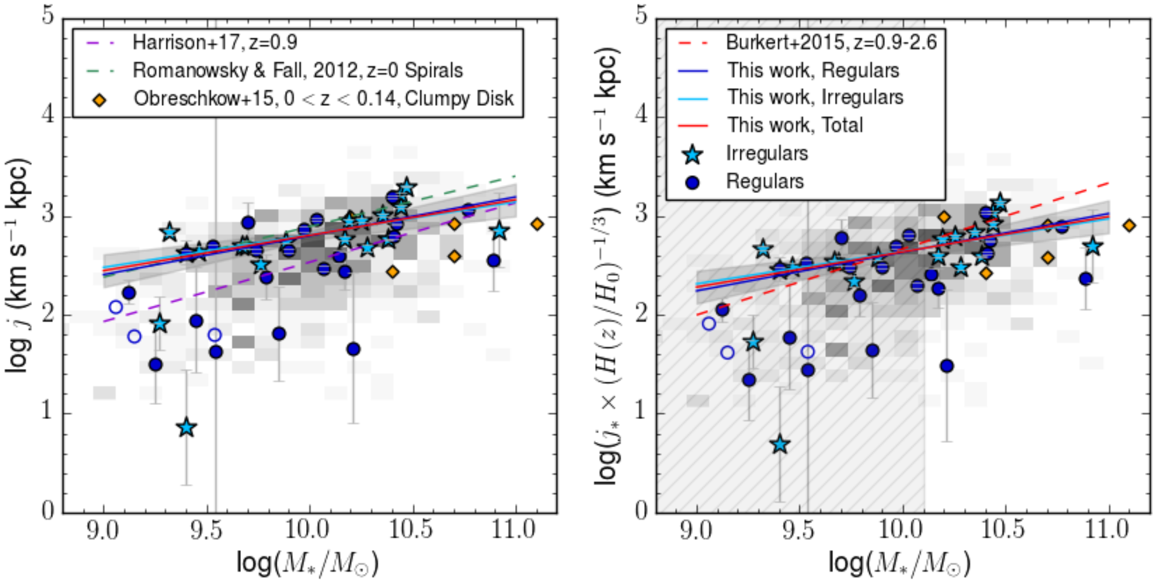

Figure 3.7: Specific angular momenta of ZFIRE galaxies. Left: Specific angular momenta j against M$_{\star}$. We compare to the $z = 0.9$ KROSS survey (purple dashed) (Harrison et al., 2017), the $z = 0$ spiral galaxies from Romanowsky and Fall (2012) (green dashed line), and the $z = 0.1$ clumpy, turbulent disk sample of Obreschkow et al. (2015). The shaded squares show the density of objects from the KROSS $z = 0.9$ survey. Right: We correct our values of j for redshift and compare to the results of Burkert et al. (2016) (red dashed). The shaded region shows the mass limit for the selection of galaxies used in the Burkert et al. (2016) sample. Reproduced by permission of the AAS.

There are no significant differences between regulars and irregulars, although scatter in regulars (0.56 ± 0.03 dex) is higher than irregulars (0.48 ± 0.03). The difference in scatter is due to the slow-rotating low-mass regulars. We see similar slow rotators in the irregular population, but we have fewer in our sample. In both cases, we find a similar, shallow slope of 0.39 ± 0.12 for regulars and 0.33 ± 0.20 for irregulars. The shallow slope is from weighting of our linear fits, since low-rotation objects tend to have higher uncertainties in their measurements. When we perform a linear fit without weighting, we find values much closer to the predicted ($A = 0.63 \pm 0.14$, for the total sample, 0.56 ± 0.15 for regulars, and 0.66 ± 0.27 for irregulars). When we fix $r_t = 1/3r_s$, we find the slope to move to 0.44 ± 0.12 with no significant differences between irregulars and regulars. We find similar results when $r_t = 0.4r_s$.

When we hold the slope to be 2/3, we obtain a normalization of 2.72 ± 0.07, which is a normalization offset of 0.12 ± 0.09, or little to no redshift evolution from $z = 0$. This is in conflict with the Harrison et al. (2017) measurement of a 0.3 dex offset from $z = 0$. However if we perform the linear fit without weighting, we find a consistent offset with Harrison et al. (2017). In order to conclusively measure the slope and normalization of the line, we will need to explore the kinematics of low-rotation galaxies with greater precision, to bring these minimize our uncertainties. It is expected that for ΛCDM disks, $\log j \propto \log({M_\odot}^{2/3})$ unless there is mass-dependent angular momentum buildup of the disk (Romanowsky and Fall, 2012). If these results are confirmed, it is suggestive that stellar mass has a larger effect on angular momentum than morphology at $z \sim 2$.

Angular momentum is expected to decrease with increasing redshift due to cosmic expansion as

$$j \propto (1+z)^{-1/2}, \tag{3.6}$$

(Obreschkow et al., 2015). To determine if our sample shows any evolution apart from the theoretical ΛCDM evolution we scale our sample to local galaxies using Equation 6. After correcting for any redshift evolution (Figure 3.7, right panel), we compare our findings to the work of Burkert et al. (2016). We again see a shallower slope than the $\log j \propto \log({M_\odot}^{2/3})$

trend, but when holding the slope to 2/3 we find an offset with the Burkert et al. (2016) results of 0.12 ± 0.07 dex. If we set r_t to fixed positions relative to r_s, find no significant difference from free r_t. Given the scatter in this relation (0.52 dex), we do not find this to be a significant difference from the Burkert et al. (2016) result, which is not expected to evolve with redshift.

A two-population KS test confirms that to a 95% confidence level, irregular galaxies have higher specific angular momenta than regular galaxies at equivalent stellar mass. Further observations are needed to confirm these results due to low numbers and possible unresolved irregular structure in regular galaxies. Most of this offset is on the low-mass ($M_\star$<10) end of the j-$M_\star$relation, on the high-mass end ($M_\star$>10) these relationships tighten. When low-rotation resolved objects are removed, the irregular and regular populations are not significantly different.

Additionally, we compare our sample to the clumpy, turbulent galaxies of Obreschkow et al. (2015), often considered high redshift analogs in the local universe. We can confirm that at least kinematically, $z \sim 2$ galaxies have similar properties to these local galaxies.

3.5 Discussion

3.5.1 Morphology and Kinematics

In some cases it appears that irregulars, including merger candidates, show ordered rotation fields, and as such cannot be identified by kinematics alone. This is also observed in the IFU-based work of KMOS Deep Survey (KDS) (Turner et al., 2017), who describe a similar phenomenon of merger candidates with ordered rotation fields. In Hung et al. (2015) local merging galaxies are artificially redshifted and their rotation is examined. All mergers with the exception of those with strong tidal features and two nuclei showed ordered rotation fields. This could explain the similarity of the kinematic scaling relations for regular and irregular galaxies, which could include mergers, derived in our results. We demonstrate that our irregular galaxies are often well-described by ordered rotation, as our models are derived from rotation-dominated isolated galaxies, and our kinematic extractions assume ordered rotation.

However as irregular galaxies are not well described by photometric modeling (Figure 3.1), these measurements could be incorrect from assuming that our morphological and kinematic PAs are consistent, and that our intrinsic axis ratio is 0.18. Similarly, in our modeling, we assume that all galaxies are infinitely thin disks with Sérsic indices of 1, which is not true for most of our measured galaxies, and for irregular galaxies, the Sérsic profile is unreliable.

Given these caveats in our analysis, we expect different behaviors in our kinematic relationships if growth is dominated by major mergers or smooth gas accretion. Mergers, depending on the geometry of the system, could cause a system to abruptly gain or lose angular momentum, and would increase the scatter around kinematic scaling relations (Vitvitska et al., 2002; Naab et al., 2014; Rodriguez-Gomez et al., 2017). Assuming that these mergers are not happening in a preferred direction, we would expect a larger scatter in our velocity and angular momentum relations in merging galaxies (which we are assuming are represented by irregulars). We would also expect these galaxies to have higher values for σ_g than galaxies that have not undergone a recent merger.

If growth is dominated by smooth accretion, the angular momentum of galaxies would again be subject to the direction of gas falling onto the disk. If gas is accreted along a filament, it would exert a torque causing an increase in angular momentum (White, 1984; Kereš et al., 2005; Sales et al., 2012).

Kinematic surveys are often biased toward galaxies with ordered rotation and a relatively small contribution of σ_g toward overall kinematics at an observed redshift. This is partially because these galaxies are usually intrinsically brighter, as they are more massive. In addition to brightness, the size of a galaxy can have an effect on its kinematics. Newman et al. (2012) demonstrated that spatially unresolved galaxies in kinematics surveys can have underestimated rotational velocities. In our sample, we rejected four compact galaxies with unreliable measurements for $V_{2.2}$. This could bias our sample and our results, underestimating the prevalence of low $V_{2.2}/\sigma_g$ galaxies. Additionally, we could be classifying galaxies with unresolved irregular structure as regular galaxies.

We find similar levels of scatter between regular and irregular populations in the TFR, $S_{0.5}$, (Figure 3.3) and j_{disk} relations, but irregular galaxies have higher j_{disk} values at given stellar mass (Figure 3.7), and do not have higher values of σ_g (Figure 3.5). Due to our limited sample, more observations are needed to confirm these results. Given that these galaxies have clear irregularities and sometimes show obvious signs of merging close companions, these results are puzzling. We have yet to find simulations which show results like our observations.

In the case that irregulars have higher j_{disk} than regular galaxies, a significant portion of our sample is in an over-dense proto-cluster region, and this may affect the direction of gas infall or orientation of mergers. Our assumption was that in the case of merger-dominated or accretion-dominated growth, orientation would be random, and would create a stochastic scatter. However it is possible that these interactions may have a preferred orientation, possibly due to the filamentary structure of the cosmic web (Kereš et al., 2005; Sales et al., 2012; Stewart et al., 2013; Danovich et al., 2015). More observations are needed for a robust analysis of our conjecture, and knowledge of the cosmic web surrounding this structure would be beneficial.

3.5.2 The Reliability of Kinematics From Slit Spectroscopy

Some of the scatter in our kinematic scaling relations and angular momentum is possibly related to the scatter in our ability to recover our simulated V_{rot} and σ_g, and the inherent issues with recovering velocities in unresolved galaxies. This was likely because in unresolved emission lines, the position of the turnover radius is unclear, so we tend to overestimate the positions of simulated r_t and V_t. In other surveys, it is assumed $r_t = 0.4r_s$, as observed in Miller et al. (2011). However, this is an empirical observation at $z \sim 1.7$, when disks are settling. Whether this assumption holds at $z > 2$ is unclear, but the position of r_t in an arctangent velocity curve will affect the derived rotational velocities of a galaxy.

Our simulations (Appendix B) demonstrate that we tend to consistently overestimate $V_{2.2}$ by around 10% at high data quality (Appendix B.1) and inclination $> 25^o$ (Figure B.2). When we can fix r_t to a known value, our recovery is more accurate, to 5%. Similarly we underestimate σ_g by 10%. Small deviations from our inputs in either of these values lead to overestimated values for $V_{2.2}/\sigma_g$ with a high scatter in recovered values of our simulations, meaning recovered $V_{2.2}/\sigma_g$ values may be unreliable (Figure B.3). However, these offsets lead to only slightly overestimated values for $S_{0.5}$, which are reliably offset at high data quality and inclination $> 25^o$. Similarly, our recovery of j_{disk} is reliable within 5% of the input with small scatter in our results (Figure B.4). These results show that given the degeneracies seen in modeling emission lines from slit spectroscopy, we can reliably recover values for $S_{0.5}$ and j_{disk} if these offsets are accounted for.

We suggest that current slit observations and data analysis can reliably measure $S_{0.5}$ and specific angular momentum of spatially resolved galaxies at $z \sim 2$. Unresolved galaxies can give unreliable velocity measurements, so increased spatial resolution in multi-object spectrographs are necessary to progress in our understanding of high-redshift kinematics. The James Webb Space Telescope (JWST) will benefit kinematics due to the NIRSPEC instrument for this reason. NIRSPEC shutter resolution will be at $0.1''$, but more importantly these data will not be seeing-limited. Multi-object slit spectroscopy and JWST provide the opportunity for larger sample sizes, and increased sensitivity to low-mass and faint objects. As we enter the era of large astronomical surveys, slit spectroscopy will prove an invaluable tool for building large samples of galaxies.

3.6 Summary

We examine an environmentally diverse sample of $z \sim 2$ star-forming galaxies in the COSMOS field observed by the ZFIRE survey. Complementary NIR imaging in the F160W bandpass from HST/WFC3 as part of the CANDELS project allow for morphological analysis of this sample. This sample is made up of 44 galaxies: 14 are associated with an over-dense region at $z = 2.095$ and 30 are in the field from $2.0 < z < 2.5$. These galaxies are split into two morphological sub-samples, termed "regulars" (25) and "irregulars" (19) (Figure 3.1). This classification is based on the presence of excess residual emission from a single-Sérsic fit where a galaxy is classified as an irregular if residual levels are above twice the nearby sky levels, and greater than 25% of the original flux levels.

The Hα emission lines are used to extract kinematic components using HELA. HELA simulates a 3D data cube, collapses it into a 0.7$''$ slit, and runs an MCMC simulation to determine the best-fit model to the emission line, assuming an arctangent rotation curve and a constant gas velocity dispersion. HELA recovers the velocity of simulated galaxies (Appendix B) at $2.2r_s$ ($V_{2.2}$) to within 10% of our input and σ_g to within -10% of its input (Figure B.2). Using recovered kinematics, HELA can reliably recover $S_{0.5}$ to a minor offset of within -10% of the input, and j_{disk} (specific angular momentum) to within -5% of the input (Figures B.3 and B.4). $V_{2.2}/\sigma_g$ tends to be overestimated by 30% with a high scatter in recovery. When we constrain the location of the kinematic turnover radius r_t to a known position relative to the scale radius r_s, our offsets decrease by 5% from inputs.

Using the values for $V_{2.2}$ derived from our fitting method, we determine a stellar-mass TFR of $\log(V_{2.2}) = (0.29 \pm 0.1) \log(M/M_\odot - 10) + (2.19 \pm 0.04)$ (Figure 3.3). There are no significant differences between regulars and irregulars. When we include the contribution of σ_g, in the case of $S_{0.5}$, we find $\log(S_{0.5}) = (0.38 \pm 0.07) \log(M/M_\odot - 10) + (2.04 \pm 0.03)$. The scatter of the overall sample is consistent with other measurements of $S_{0.5}$ at $z > 1.5$ Price et al. (2016); Straatman et al. (2017).

To measure pressure against rotational support, we determine $V_{2.2}/\sigma_g$ (Figure 3.4), and measure a trend of increasing rotational support with increasing stellar mass, similar to the results of Simons et al. (2016). However there is high scatter in our recovery of simulated $V_{2.2}/\sigma_g$values, leading us to believe that the significant scatter in our results (0.6 dex) may be driven by measurement uncertainties.

We compare our results to the mathematical modeling of Krumholz et al. (2018), which are based on a balance between turbulence driven by star-formation feedback and gravitational instability, and the dissipation of turbulence by mass transport (Figure 3.6). Our sample shows a similar shape in the dust-corrected SFR and $\sigma_g$turbulence but the models over-predict the SFR necessary to produce high gas turbulence in high redshift galaxies.

We also estimate specific angular momentum values (Figure 3.7), and determine that galaxies have a shallower relationship (slope $A = 0.36 \pm 0.12$) between j_{disk} and $M_\star$ than predicted ($A = 0.67$), either due to undersampling low-rotation low-mass galaxies, or due to a mass-dependent angular momentum buildup in the disk (Romanowsky and Fall, 2012). Additionally, we do not find any evidence of angular momentum offsets with redshift at consistent stellar mass. More observations of these galaxies will clarify our results, as well as more precise measurements of the kinematics of pressure-dominated SFGs. Our irregular and regular populations were consistent. Our simulated observations demonstrate reliable recovery of input kinematics, and we achieve similar j_{disk} measurements to $z \sim 0.1$ high-z analogs (Obreschkow et al., 2015).

Our work demonstrates that slit spectroscopy can reliably recover kinematics measurements such as $V_{2.2}$, $S_{0.5}$, or j_{disk} to either a consistent offset that can be corrected, or to a small offset from simulated inputs. Low spatial resolution can limit our ability to recover kinematics, but with an increase in resolution, MOS spectroscopy can provide robust kinematic measurements. In the coming age of large astronomical datasets, the reliability of slit spectroscopy will be instrumental in building large spectroscopic samples at high redshift and using the Near Infrared Spectrograph, NIRSPEC on the James Webb Space Telescope.

4. NEBULAR GAS PROPERTIES OF PROTO-CLUSTERS AT $Z \sim 1.6$ AND $Z \sim 2$

4.1 Introduction

Proto-clusters are the precursor to the most extreme environments in the universe. In the local universe ($z = 0$), there is a relationship between environmental density and the properties of galaxies (i.e. morphology, stellar populations, star-formation rate). In particular, studies have found an elevated gas-phase metallicity fraction in local cluster galaxies (Cooper et al., 2008; Ellison et al., 2009), lower star-formation rates (SFR) (Lewis et al., 2002; Grootes et al., 2017; Jarrett et al., 2017), a greater fraction of elliptical and lenticular galaxies in denser environments (Houghton, 2015), and a higher fraction of slow rotators in dense environments (Cappellari et al., 2011). Since cluster environments show this correlation at low redshift ($z < 0.5$), we wish to observe when and by which mechanisms the environment-dependent evolution of galaxies unfolds. At higher redshifts and younger cluster ages, the fraction of low SFR and quenched galaxies in denser environments decreases (Kawinwanichakij et al., 2017), until the star formation rate density of the universe reaches its peak (Madau and Dickinson, 2014).

The period known as "Cosmic Noon" ($1.5 < z < 2.5$) is of particular interest as this is the stage where massive galaxies within proto-clusters are rapidly building their stellar populations (Tran et al., 2010). Analyses of metallicity (Kacprzak et al., 2015, 2016), star-formation (Tran et al., 2015, 2017), ionized gas characteristics (Kewley et al., 2015), and kinematics (Alcorn et al., 2016) of proto-cluster members at $z > 1.5$ showed no differences from observed field galaxies. However, other studies have shown an increase in the radii of star-forming cluster galaxies relative to the field (Allen et al., 2015), clear signatures of the morphology and color relation in dense environments (Papovich et al., 2012; Bassett et al., 2013), and an increase in merger rates in high-redshift clusters (Lotz et al., 2013). Cosmological simulations have not focused on the cluster environment at $z > 1.5$ until recently. Gupta et al. (2018) observed that within the Illustris-TNG (100 Mpc)^3 simulation (TNG100), galaxies bound to 127 proto-clusters show a ∼0.05 dex gas-phase metallicity enhancement compared to field galaxies starting at $z = 1.5$, but no significant offsets at $z = 2$ and higher. This possibly identifies the redshift when the cluster environment starts influencing member galaxies.

The ZFIRE survey (Nanayakkara et al., 2016) observed and spectroscopically confirmed the over-dense regions in the COSMOS field at $z = 2.095$ (Yuan et al., 2014), and the over-dense region in the UDS field at $z = 1.62$ was spectroscopically verified in Papovich et al. (2010) and subsequently analyzed in Tran et al. (2015). With this data set, it is possible to extend scaling relations to the proto-cluster environment at higher redshift, and examine the baryon cycle, galactic winds, and the interstellar medium (ISM) in a cluster and its member galaxies. The proto-clusters observed in this study were originally identified using deep NIR imaging in Papovich et al. (2010); Spitler et al. (2012). Using rest-frame optical emission lines from the ZFIRE collaboration, we can directly compare nebular gas properties of cluster and field populations at this epoch.

The ZFIRE collaboration has extended its sample size from the initial data release (Nanayakkara et al., 2016) in both the UDS and COSMOS fields, and measured more nebular emission lines (Hβ, [O III]) from galaxies in the previous sample. The extended sample allows us to perform an improved analysis of the Baldwin-Phillips-Terlevich (BPT) Diagnostics (Baldwin et al., 1981) on the basis of redshift, inferred stellar mass, and environmental density. This diagnostic will provide information on the nebular gas in each cluster to determine if star-forming conditions evolve with redshift.

By including improvements in gas-phase metallicity indicators, we will re-examine galaxy metallicity and directly compare two proto-clusters at differing redshifts. Gas-phase metallicity measurements can differ between objects by up to 1 order of magnitude. Discrepancies between different strong-line indicators are possibly the result of calibration on local HII regions. Calibrations using local HII regions are can be flawed when used for high-redshift measurements because significant changes in the ISM of high-redshift galaxies have been observed. In particular, galaxies at high redshift have been observed to have higher ionization parameter and electron density than local galaxies (Kewley et al., 2013; Shapley et al., 2015).

We utilize the strong-line diagnostics introduced in Pettini and Pagel (2004) (referred to herein as PP04) and the newer indicator Dopita et al. (2016) (referred to as D16). The PP04 indicator is in widespread use in high-redshift extragalactic astronomy (Sanders et al., 2018) and is not sensitive to reddening (as it requires a ratio of Hα and [N II] fluxes). However it is subject to the calibration issues presented and is sensitive to the ionization parameter and electron density of a host galaxy. The D16 indicator attempts to correct this by including the [S II] doublet in this ratio, and modeling shows that it is insensitive to ionization parameter and electron density. We measure gas-phase metallicity using both indicators in this study to determine the effectiveness of the D16 indicator.

In Section 4.2 we review our data from ZFOURGE, UKIRT, and MOSFIRE. We discuss our line-fitting and flux extraction methods in Section 4.3 including both individual objects (Section 4.3.1) and stacked emission lines (Section 4.3.2). Our results for gas-phase metallicity between cluster and field and any possible redshift evolution between the UDS and COSMOS clusters are shown in Section 4.4.1. The nebular gas analysis of individual galaxies and our stacked objects is located in Section 4.4.2. Finally, our results are put into the context of proto-cluster evolution in Section 4.5.

In this work, we assume a flat ΛCDM cosmology with Ω_M=0.3, Ω_Λ=0.7, and H_0=70. At the COSMOS cluster redshift, $z = 2.095$, one arcsecond corresponds to an angular scale of 8.33 kpc. At the UDS cluster redshift, $z = 1.62$, one arcsecond corresponds to an angular scale of 8.47 kpc.

4.2 Data

4.2.1 Sample Selection

Our proto-cluster and field samples are drawn from the ZFIRE survey, a spectroscopic follow-up of ZFOURGE photometry (Straatman et al., 2016). For a full summary, see Nanayakkara et al. (2016).

ZFOURGE combines broad-band imaging in K_s and the medium-band J_1, J_2, J_3, H_s, and H_l filters to select objects using K_s-band images with a 5σ limit of 25.3 AB magnitudes. Candidate cluster members and field galaxies are identified from ZFOURGE NIR imaging of COSMOS fields, and the Williams et al. (2009) catalog of UDS, a subset of the UKIRT survey (Lawrence et al., 2007). Rest-frame UVJ colors are used to identify SFGs, that will have prominent nebular emission lines.

The UDS proto-cluster at $z = 1.62$ was identified by Papovich et al. (2010) and Tanaka et al. (2010). A spectroscopic confirmation of the cluster is in Papovich et al. (2010). This cluster was shown to have a strikingly low velocity dispersion of $\sigma_{cl} = 254 \pm 50$ km s^{-1} (Tran et al., 2015), and notably shows an increase in star-formation with local density (Tran et al., 2010). Previous studies of this proto-cluster show no enhancement in gas-phase metallicity (using the PP04 indicator, commonly referred to as N2 in literature) or attenuation compared to field samples (Tran et al., 2015).

The COSMOS proto-cluster was initially identified in Spitler et al. (2012) using photometric redshifts from ZFOURGE and confirmed with spectroscopic redshifts from MOSFIRE (Yuan et al., 2014). This over-density consists of four merging groups, and is projected to evolve into a Virgo-like cluster at $z = 0$. Cluster members are identified to redshifts within $2.08 < z < 2.12$, and the cluster velocity dispersion was shown to be $\sigma_{cl} = 552 \pm 52$ km s^{-1}.

ZFOURGE uses FAST (Kriek et al., 2009) to fit Bruzual and Charlot (2003) stellar population synthesis models to the galaxy spectral energy distributions to estimate observed galaxy properties. We calculated stellar masses and attenuation values (A_V) with FAST using the spectroscopic redshift from MOSFIRE. We assume a Chabrier (2003) initial mass function with constant solar metallicity and an exponentially declining star formation rate, and a Calzetti et al. (2000) dust law.

4.2.2 MOSFIRE NIR Spectroscopy

Observations were taken in December 2013, February 2014, January 2016, and February 2017 in the H and K filters covering 1.47-1.81 μm and 1.93-2.45 μm, respectively. Seeing varied from $\sim 0.4''$ to $\sim 1.3''$ over the course of our observations.

The spectra are flat-fielded, wavelength calibrated, and sky subtracted using the MOSFIRE data reduction pipeline (DRP)¶. A custom ZFIRE pipeline corrected for telluric absorption and performed a spectrophotometric flux calibration using a type A0V standard star. We flux calibrate our objects to the continuum of the standard star, and use ZFOURGE photometry as an anchor to correct offsets between photometric and spectroscopic magnitudes. The final result of the DRP are flux-calibrated 2D spectra and 2D 1σ images used for error analysis with a flux calibration error of $<$10% ($\sim$0.08 mag). For more information on ZFIRE spectroscopic data reduction and spectrophotometric calibrations, see Nanayakkara et al. (2016).

4.3 Methods

4.3.1 Emission Line Flux Measurements

We obtain emission line fluxes from our telluric-corrected and flux-calibrated spectra by fitting Gaussian profiles to our emission lines. Our 2D spectra are collapsed to a 1D spectrum by fitting a Gaussian to the spatial line profile, and summing along an aperture where each edge is two Gaussian full-width half max away from the centeroid of the spatial profile of the emission line. We then fit a single Gaussian profile to the 1D spectrum of the emission line. In the case of the [S II] doublet, we fit two single Gaussian profiles simultaneously at fixed, redshifted offset between their centroids. In Figure 4.1, it is clear that the [S II] lines are

---

¶http://keck-datareductionpipelines.github.io/MosfireDRP/

well resolved and not blended, so we fit independent Gaussian profiles to the [S II] doublet at fixed width between the peaks of each emission line.

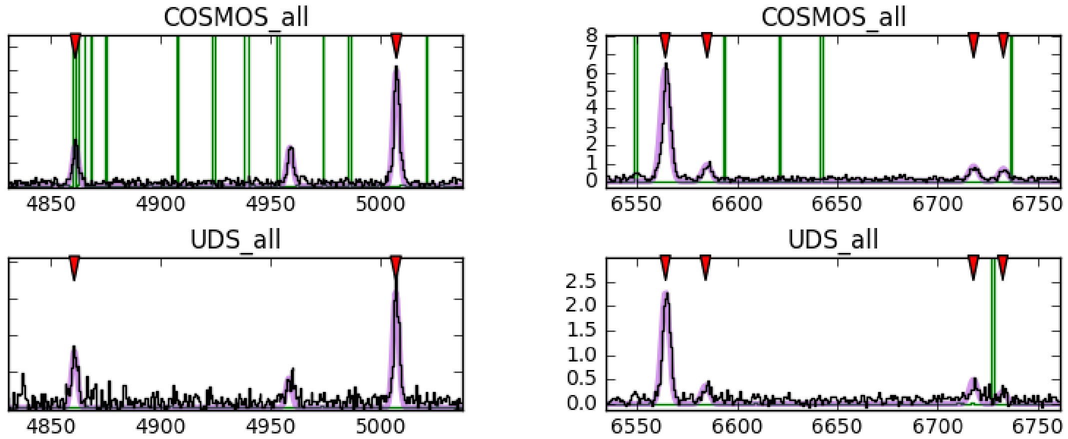
COSMOS_all
COSMOS_all
UDS_all
UDS_all

Figure 4.1: Stacked rest-frame spectra of our sample, showing Hα, [N II] , Hβ, and [O III]. In the COSMOS sample, Hβ and [O III] are found in the MOSFIRE H band, and Hα,[N II] , and [S II] in the K band. Black are the stacked lines, which have been outlier-rejected. Green are the error spectrum, and pink are the best-fit Gaussian for the measured emission lines. Red arrows at the top of each spectrum point to the measured emission lines. Left Column: The stacked [O III] and Hβ emission lines. In COSMOS, these lines are observed in the MOSFIRE H band. Right: The stacked Hα, [N II] , and [S II] emission lines. In the COSMOS sample, these lines are observed in the K band. The Gaussian fits are used to measure stacked flux ratios.

From the best fit profile to the emission line, the standard deviation of the Gaussian is used to determine the range over which the line will be integrated, and we sum under the best-fit Gaussian from $-3\sigma < \lambda_{obs} < 3\sigma$. This value is our extracted flux measurement. We measure noise by summing the error spectrum in quadrature over the same bounds as the signal. If the best-fit Gaussian for a faint line ([N II] , [S II] , Hβ) has a width less than $2\times$ the wavelength resolution, we refit the line holding the Gaussian σ fixed to the σ measurement of the Hα line (for [N II] and [S II]) or the [O III] emission line (for Hβ). If the emission line of an object is less than $2\times$ the measured noise in its region, we mark this object as an upper limit of the signal (unfilled points on Figure 4.2) and use the 1σ noise limit as our flux detection.

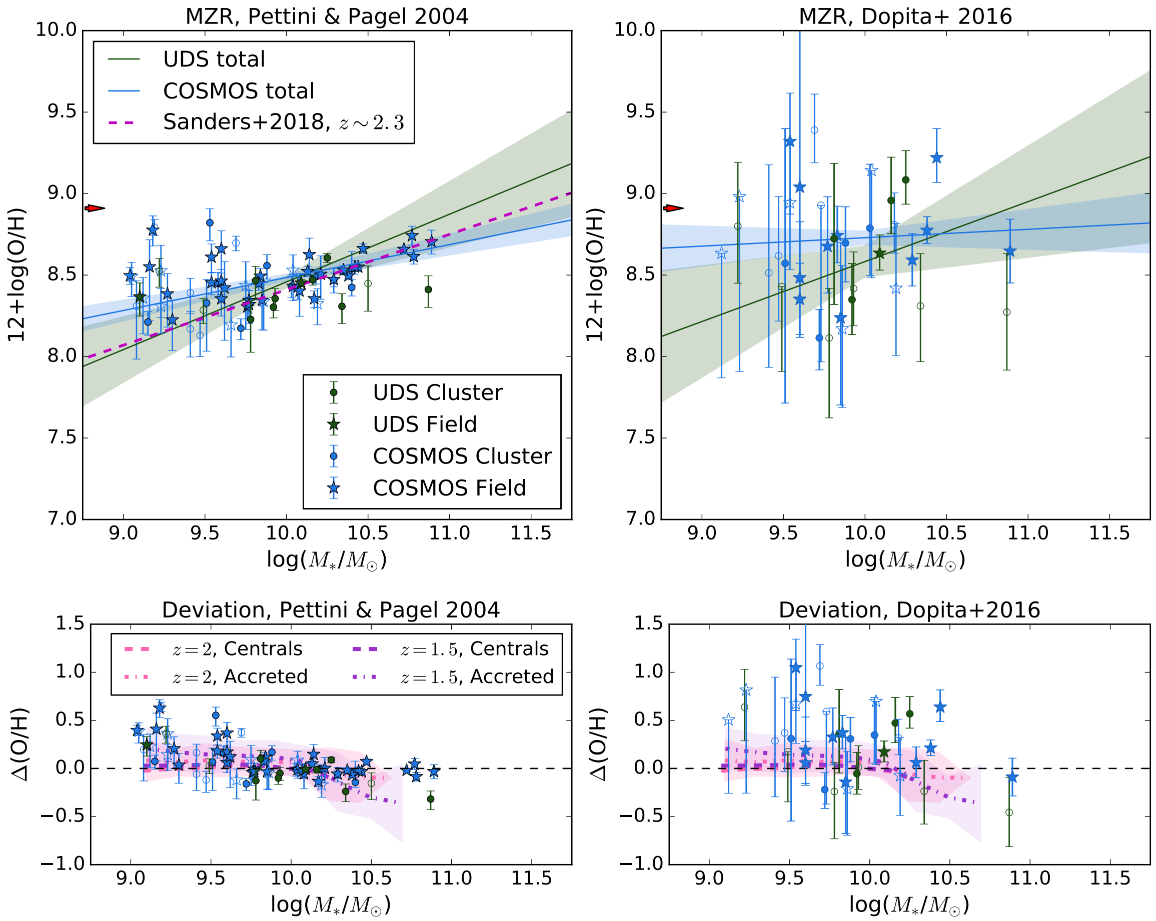

Figure 4.2: Top Left: Metallicity values as determined by the indicator presented in Pettini and Pagel (2004). All emission lines are above a 2σ detection limit. When at least one emission line shows significant sky interference, the point is unfilled. We compare to the MOSDEF metallicity measurements (Sanders et al., 2018) at $z \sim 2.3$. Top Right: Metallicity values as determined by the indicator presented in Dopita et al. (2016). We show our best-fit linear relations for UDS and COSMOS in their respective colors. Bottom rows: The dotted and dashed lines in pink and lavender are theoretical measures of the Mass-Metallicity Relation (MZR) from the Illustris simulation (Torrey et al., 2018). Shaded regions show the scatter in the accreted populations. Central galaxies have equivalent levels of scatter. Centrals are galaxies in the center of their own dark matter potential (equivalent to a field sample), and accreted galaxies are equivalent to a cluster sample. We plot the deviation from the MZR predicted in IllustrisTNG with respect to $z = 2$ centrals (black dotted line).

4.3.2 Stacking Emission Lines

As many of our galaxies have very faint emission lines (i.e. [N II] , Hβ, [S II]), we stack our galaxy spectra into bins of stellar mass and environment to determine characteristics of their populations. To separate the effects of AGN activity, we reject the objects identified as AGN in Cowley et al. (2016) from our bins and stack separately in our BPT diagrams for reference. Cowley et al. (2016) identifies AGN in the ZFOURGE sample using radio, IR, UV, and X-ray data. AGN can affect placement on the BPT diagram as the emission is from shocked gas or photoionization by the hard ionizing spectrum of the AGN rather than gas photo-ionized by young stellar populations.

Spectra are collapsed over the same spatial aperture as determined in Section 4.3.1, then normalized to the Hα flux or [O III] flux, dependent on the filter observed. Objects are then interpolated onto a reference rest wavelength range preserving flux. We sum our stacks after rejecting outlier pixels with values greater than the median $\pm 3\sigma$. We perform our Gaussian line-fitting procedure from Section 4.3.1 to determine stacked fluxes.

We stack our objects based on mass, environment, field (COSMOS vs. UDS), and detected AGN activity. Objects are separated into low vs. high stellar mass objects ($\mathrm{M}_{\star} < 9.72$ and $\mathrm{M}_{\star} > 9.72$, determined from the median stellar mass of the total ZFIRE sample), as well as objects identified within each field's proto-cluster and field objects. We performed a mass-matched analysis to determine if this affects our results, by rejecting objects in the UDS sample that are higher mass than the objects in the COSMOS sample, and find our results are consistent.

4.4 Results

4.4.1 Gas-Phase Metallicity

We apply the strong line diagnostic presented in Dopita et al. (2016) to determine gas-phase metallicities for a sample of our galaxies (Figure 4.2). This indicator requires measurements of the Hα, [N II] , and [S II] emission lines. In the MOSFIRE K band, this indicator can be used from $1.8 < z < 2.6$. In the H band, it can be used from $1.2 < z < 1.8$. These lines are able to be observed in the same band for most of our objects observed on MOSFIRE, and as such are less sensitive to the effects of dust reddening, as absolute fluxes are not required.

However, the [S II] doublet is quite faint for most objects in our sample, and in many of our objects we can only determine an upper bound of metallicity, as the [S II] doublet may only be slightly above the noise level, and our error ranges can be quite large. Additionally, in the UDS sample, the [S II] 6731Å emission line is in a region of high sky interference, so we mark most of our UDS objects as having unreliable Dopita et al. (2016) metallicities. However, it may bias our sample if we only include objects with strong [S II] fluxes in low sky regions, so we mark objects with sky interference with unfilled points in Figure 4.2.

Despite this observational difficulty, the strength of this diagnostic is its independence from ionization parameter and ISM pressure, which have been shown to differ between local galaxy populations and those at high redshift (Kewley et al., 2015). This diagnostic depends on the correct calibration of the N/O ratio, as with the N2 metallicity diagnostic (Pettini and Pagel, 2004).

For comparison, we also determine metallicities from the PP04, or N2, indicator (Pettini and Pagel, 2004). We find that at lower values of metallicity $12 + log(O/H) < 8.25$, the Pettini and Pagel (2004) indicator predicts higher metallicity values than the Dopita et al. (2016) method, possibly indicating a floor on measurement sensitivity at lower metallicity and low mass at $z > 1.5$. Additionally, we compared our measurements to the MOSDEF sample, which only used the N2 indicator (Sanders et al., 2018), and found similar results with our N2 measurements.

There is a large difference in the scatter of between the two metallicity indicators. The scatter from the PP04 method is much lower than D16, most likely because there are fewer low-flux emission lines needed for the PP04 measurement. [S II] is a very faint emission line doublet, and for many of our galaxies we extracted flux limits rather than fluxes. Additionally, the [S II] line 6731Å in the UDS cluster is located in a high sky-noise region, making flux extraction difficult and we extract flux upper limits. This likely explains the high scatter and super-solar metallicity values.

We find consistent results to the previous ZFIRE analysis of metallicity (Kacprzak et al., 2015), which determined that the COSMOS $z = 2.095$ cluster shared the same Mass-Metallicity Relation as the field galaxies. Similarly, in (Tran et al., 2015) the UDS $z = 1.62$ cluster also showed a lack of environmental influence on gas-phase metallicity. We find here that these clusters also share the same Mass-Metallicity Relation (MZR), and show no strong environmental influences. There is no redshift evolution between these clusters in metal abundances.

IllustrisTNG determined gas-phase metallicity relations for $2 < z < 10$ (Torrey et al., 2018) and we compare our results to these values. In Figure 4.3, we show the relation for central galaxies (central galaxies within their dark matter halo, similar to our field galaxies) and accreted galaxies (in-falling galaxies, equivalent to our cluster galaxy samples) at $z = 2$. The IllustrisTNG relations were not analyzed on the basis of normalization, as there are uncertainties inherent in gas-phase metallicity indicators, and instead the analysis was focused on the relative difference between the MZR at differing redshifts, which is the reason for the offset seen in Figure 4.2 between theoretical and observed values.

When we stack our galaxies by environment and stellar mass (see Figure 4.3), we find the same results. We find that the MZR of cluster and field populations are consistent with each other. We find no strong offsets between cluster and field in gas-phase metallicity.

4.4.2 BPT Diagnostics

A subset of our galaxies in both proto-clusters have measurements of all emission lines necessary to apply Baldwin-Phillips-Terlevich (BPT) Diagnostics (Baldwin et al., 1981). These emission lines are Hβ 4861Å, [O III] 5007Å, Hα 6563Å, and [N II] 6585Å. We require our detections for all lines to be at SNR> 2.

UDS galaxies appear to be offset from the COSMOS sample in the BPT diagram (Figure

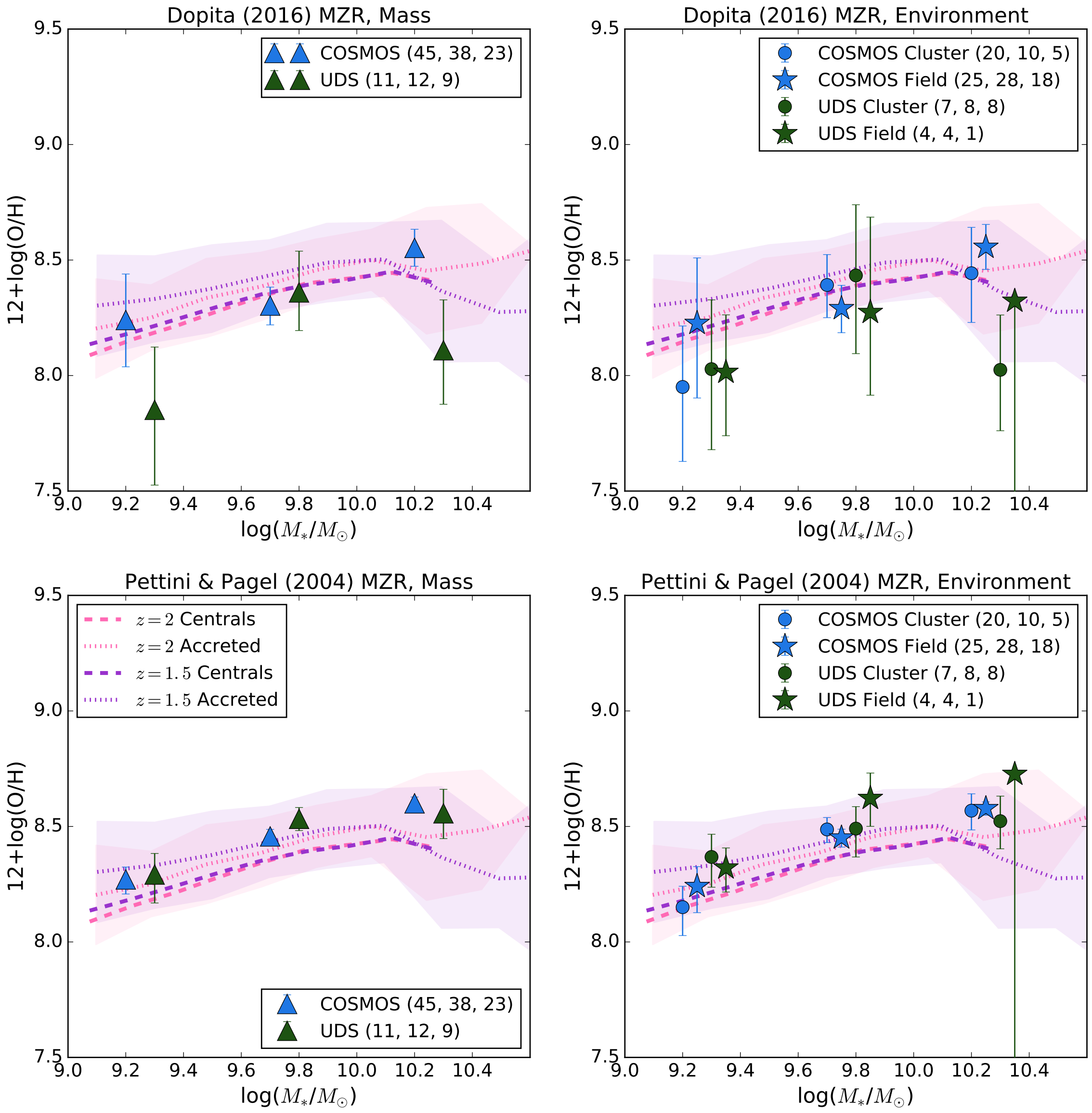

Figure 4.3: The stacked metallicity measurements from the sample. Top rows are metallicities determined from the indicator presented in Pettini and Pagel (2004), bottom rows are determined from the indicator in Dopita et al. (2016). Mass bins are offset for clarity. The IllustrisTNG simulations are shown in pink and lavender, with scatter in the accreted values shown in shaded regions. Left: Metallicity values binned by mass. The low mass bin includes galaxies with log($M_\star$) < 9.54, the medium mass bin from $9.54 <$log($M_\star$)< 10.1, and the high mass bin from log($M_\star$)> 10.1. The legend displays the number of galaxies in low, medium, and high mass bins, respectively. Right: Metallicity binned by environment and mass.

4.4), however the Hβ line in UDS is located in a high sky-noise region, so our study may be biased toward objects with higher Hβ flux. A two-population KolmogorovâĂŞSmirnov test can reject the null hypothesis at a level of 0.005 that the COSMOS sample does not have a higher $\log([\text{O III}]/\text{H}\beta)$ ratio than the UDS sample (at a p-value of 0.0013). Deeper observations may be necessary to determine if sky interference is biasing this analysis, however our KS test results hold when we reject objects where any emission line displays significant sky interference.

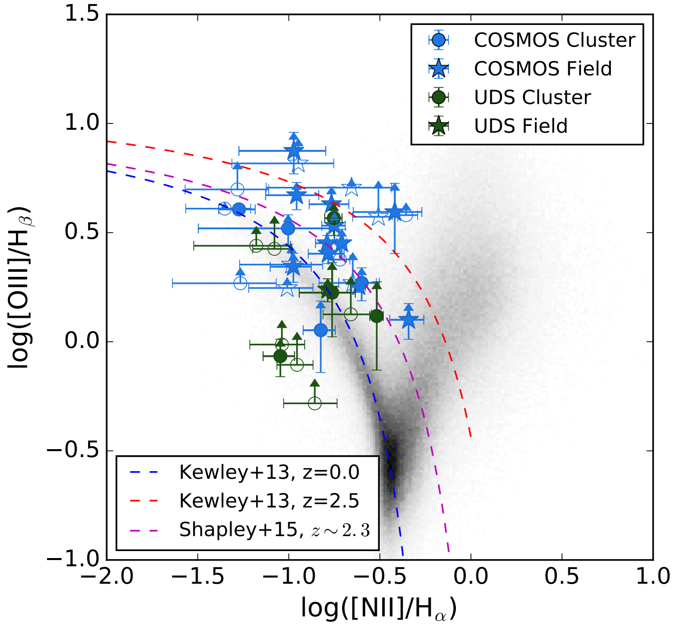

Figure 4.4: BPT diagram of galaxies within our two fields (COSMOS and UDS). Galaxies with all four emission lines Hα, [N II] , Hβ, and [O III] with greater than 2σ detection limit are shown. Galaxies with one or more emission lines with heavy sky interference are unfilled points. Colors are as in Figure 4.2. Shaded regions are SDSS galaxies. Colored curves from Kewley et al. (2013) are the upper-limit to the theoretical evolution of star-forming galaxies at $z = 0$ and $z = 2.5$.

ISM conditions are known to change in high-redshift SFGs compared to local SFGs (Kewley et al., 2013, 2015; Shapley et al., 2015). Evolution of the ionization parameter (the amount of ionization a luminous source can produce in an HII region) does not evolve significantly between $0 < z < 1$, but changes to more extreme ionizing conditions between $1 < z < 3$. Our results between the COSMOS and UDS cluster could show a tendency in the $z = 2.095$ population to have more extreme ISM conditions than the $z = 1.62$ population.

Our stacked results tell a similar story (Figure 4.5). Galaxies are binned according to stellar mass (inferred from FAST), environment, AGN status (confirmed AGN are excluded from the sample but shown on our figures), and subdivided into low and high stellar mass bins for each cluster and field sample. Spectra within a bin are then stacked. In each case, the stellar mass has a strong influence on position in the BPT diagram. Higher stellar mass is known to correlate with higher metallicity and therefore higher [N II] /Hα. Cluster and field values at similar stellar mass show offsets in log([O III]/Hβ). Field objects in COSMOS are offset from cluster objects by ~ 0.15 dex, which is an offset of 2σ uncertainty. Field objects in UDS are offset from cluster objects by ~ 0.25 dex, offset by 2σ uncertainty. We will summarize each panel of Figure 4.5 here.

In the upper left panel of Figure 4.5, we see galaxies in COSMOS and UDS binned purely by cluster status. The COSMOS cluster (blue solid circle) is offset from the field (blue solid star) by ~ 0.35 dex in log([N II] /Hα), and no significant log([O III]/Hβ) offset. The UDS cluster (green solid circle), in contrast, shows a ~ 0.25 dex offset from the field (green solid star) in log([O III]/Hβ) and no log([N II] /Hα) offset. Binned and stacked AGN are shown for reference (solid black circle). Both cluster samples are located in the same range as the SDSS sample, and both field samples have consistent log([O III]/Hβ) values as the Shapley et al. (2015) MOSDEF sample of $z \sim 2.3$ field galaxies (fuchsia solid line).

We isolate the effects of stellar mass on nebular gas properties in the upper right hand panel of Figure 4.5. Very clearly there is a sequence of increasing log([N II] /Hα) ratio with stellar mass in both the COSMOS (blue triangles) and UDS (green triangles) samples. When we reject UDS galaxies at a higher stellar mass than the highers stellar mass galaxy in the COSMOS sample (a mass-matched sample), our results do not significantly change.

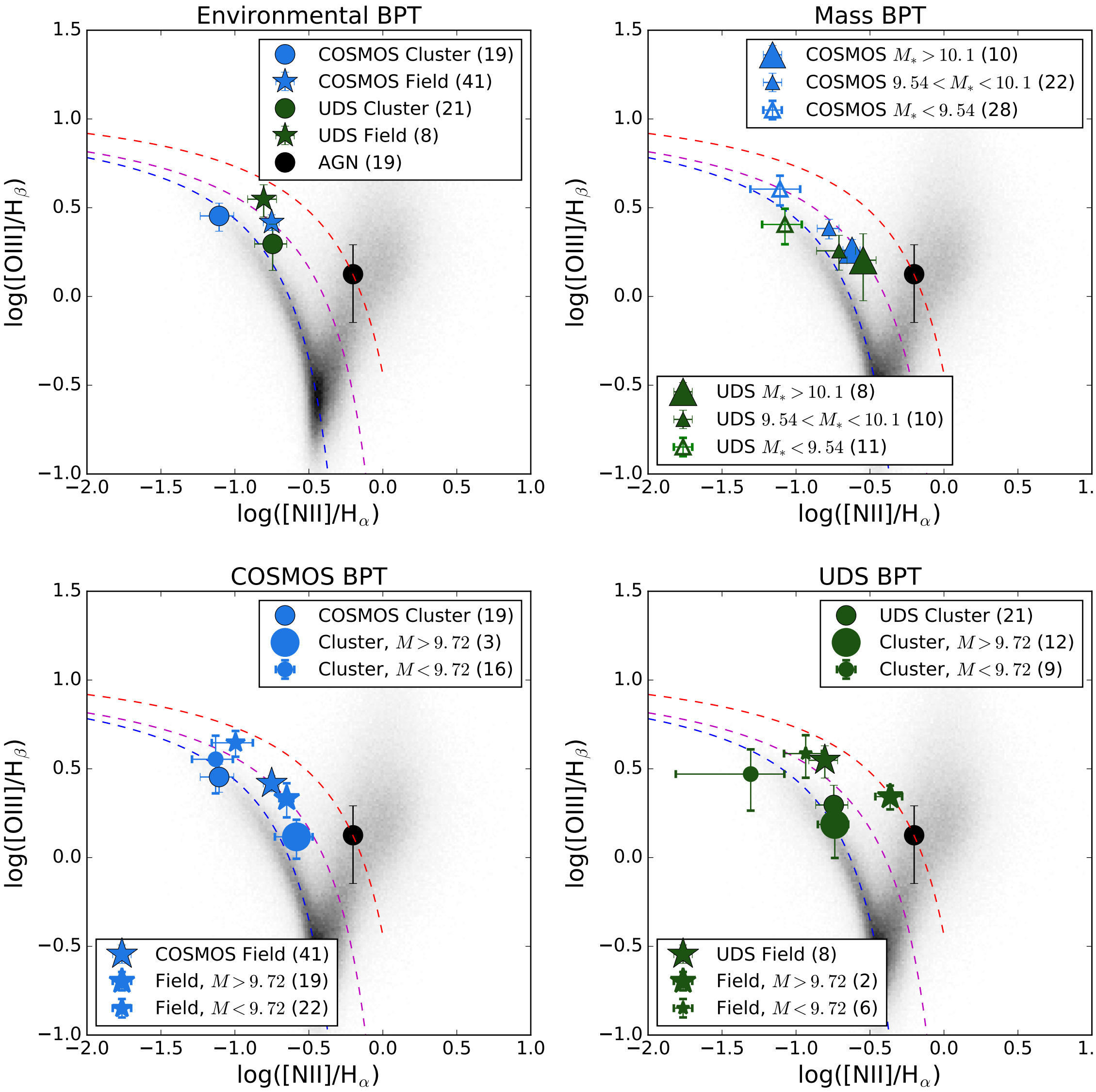

Figure 4.5: BPT diagram of galaxies within our two proto-clusters. We stack our galaxies according to their mass, environmental density, field (COSMOS or UDS), and inferred excitation mechanism (AGN identified via radio, IR, UV, or BPT diagram are separated from all stacks). Upper left: Stacking according to field and environmental density, where we find no significant environmental effects in either field. Upper right: Stacking according to FAST-inferred stellar mass. We find a stronger effect from stellar mass in both fields. Lower left: The COSMOS $z \sim 2$ sample, split into low and high mass bins in both cluster and field. We see a ~ 0.2 dex offset between field and cluster galaxies. Lower right: The UDS sample similarly separated into high and low stellar mass bins with respect to environment, again showing a strong effect of stellar mass on the Hα/[N II] ratio, but also an offset between cluster and field in [O III]/Hβ.

In order to disentangle the effects of environment and mass, we separate our cluster and field sample by stellar mass in the bottom two panels of Figure 4.5. Our cluster and field bins are binned into a low (log(M$_\star$) < 9.2, unfilled small points) and high mass (log(M$_\star$) > 9.2, unfilled large points) bin. On the lower left panel for the COSMOS sample, we find that cluster and field galaxies at equivalent stellar masses are ~ 0.15 dex offset in $\log$([O III]/Hβ). The cluster sample remains at equivalent values to the SDSS sample. These results continue in the lower right panel for the UDS sample, where instead cluster and field galaxies are offset by ~ 0.2 dex in $\log$([O III]/Hβ).

We discuss the possible explanations for this offset in Section 4.5. But, it is clear that cluster galaxies in both samples have similar ionization characteristics to SDSS local galaxies and our field samples have ionization characteristics equivalent to other $z \sim 2$ galaxies.

4.5 Analysis

The ZFIRE survey was conducted to determine if and when a galaxy's environmental density at high redshift plays a role in the evolution of its observed properties. Multiple analyses focused on star-formation rate, metallicity, ISM characteristics, and kinematics have shown that the proto-clusters observed at $z > 1.5$ have no significant environmental trends. After analyzing metallicity using an ionization parameter-independent metallicity indicator, we continue to see no strong evidence of environmental influence at $z > 1.5$ on gas-phase metallicity. We find that using the PP04 indicator continues to show a lack of environmental influence on gas-phase metallicity. Additionally, we do not find any redshift evolution between our samples. We find consistent measurements with Sanders et al. (2018) galaxies, equivalent to a field sample at $z \sim 2.3$.

The D16 indicator is less sensitive to the effects of electron density and ionization parameter (which have been observed to differ from local galaxies which metallicity indicators are commonly calibrated upon). We applied this indicator to the same sample of galaxies. Unfortunately, due to high levels of sky emission, we extracted upper limits from 13 UDS galaxy (only one galaxy without upper limits) and 47 COSMOS galaxies (13 without upper limits on fluxes). With this constraint, we find the same result as using the PP04 indicator, that environment has limited to no effect on gas-phase metallicity, and no redshift evolution.

We compare to simulated results from Illustris TNG (Torrey et al., 2018; Gupta et al., 2018), which find that cluster galaxies at $z = 1.5$ display a $\sim 0.1 - 0.2$ dex enhancement in gas-phase metallicity from field galaxies. At higher redshifts, these enhancements are not significant. We can confirm that in both populations at $z = 1.62$ and $z = 2.095$, cluster galaxies do not have significantly enhanced metallicities.

Despite previous non-detections of environmental effects on galaxy properties (Kewley et al., 2015), we do find an environmental effect on galaxy [O III]/Hβ ratio when we stack our galaxies. Cluster galaxies have on average a (0.2 dex) lower value for $\log$([O III]/Hβ) than field galaxies at equivalent stellar mass. The [O III]/Hβ ratio correlates with the ionization parameter and metallicity. Having shown no environmental offsets due to metallicity, we can assume the offset is because field galaxies have a higher ionization parameter than cluster galaxies. The offset is seen in both the UDS and COSMOS populations.

Though discovering the cause of this offset is beyond the scope of this study, we offer a few possible (but speculative) explanations for our results.

A possible cause of the lower ionization parameter seen in cluster galaxies is due to their larger volume. Allen et al. (2015) found that in the COSMOS cluster, star-forming galaxies were marginally larger in effective radius ($\sim .12$ dex) than field galaxies at equivalent stellar mass. Tran et al. (2017) found cluster and field galaxies in this sample had no significant environmental offsets in the SFR-M$_\star$ relation. Ionization parameter is the flux of ionizing photons per volume. Hence, large disk size (and therefore larger volume) of cluster galaxies at $z \sim 2$ at similar SFRs (similar ionizing flux) would result in a lower ionization parameter.

Another possible explanation of the offset could be the cut-off of cold-mode accretion, which shocks the ISM gas due to the pressure imbalance, increasing the hardness of ionizing radiation. The cold mode accretion would be cut-off in the proto-cluster environment because of the ICM (Kereš et al., 2005; van de Voort et al., 2017), resulting in harder ionizing flux in field galaxies compared to cluster galaxies. A harder ionizing flux in field galaxies can be responsible for the higher [O III]/Hβ ratio of field galaxies compared to cluster. However, this should result in a higher [N II] /Hα ratio for the cluster galaxies, which is not see in our sample. Also, shocks from filamentary accretion are unlikely to be a dominant source of ionizing photons (Rauch et al., 2011).

The UDS cluster has an observed X-ray luminosity component from which temperature (and cluster mass) can be measured (Tanaka et al., 2010; Papovich et al., 2010). The temperature measured from the X-ray luminosity was 1.7 ± 0.3 KeV, equivalent to roughly $\sim 2 \times 10^7$ Kelvin. In Kereš et al. (2005) the transition temperature between the filamentary cold-mode accretion to hot-mode spherical accretion happens when the gas is heated to $T = 2.5 \times 10^5$ Kelvin. However, we do not see an X-ray component to the COSMOS cluster, so alternative measures of the gas temperature are necessary to confirm this speculation (i.e. ALMA measurements of gas temperature).

4.6 Conclusions

We perform a BPT and metallicity analysis of two over-dense regions in UDS ($z = 1.62$) and COSMOS ($z = 2.095$). The rest-frame optical diagnostic lines Hβ, [O III], Hα, [N II] , and [S II] are measured using the NIR spectrograph on Keck, MOSFIRE. Fluxes of these emission lines and the [S II] doublet are extracted via a Gaussian fit to the 1D spectrum.

Absolute fluxes of Hα, [N II] , and [S II] are used to calculate the gas-phase metallicity using the abundance indicator presented in Dopita et al. (2016). We find no offsets between our two clusters at differing redshifts, or any enhancement relative to field galaxies at the redshifts of these galaxies. This is consistent with predictions from IllustrisTNG (Torrey et al., 2018; Gupta et al., 2018).

For the subset of galaxies where all four diagnostic lines (or their 1σ detection limits) are measured, we perform an analysis of the nebular gas properties using the BPT diagram. We find an offset in the [O III]/Hβ ratio in each population from the local SDSS sample, consistent with photoionization models at high redshift, due to an increasing ionization parameter

(Kewley et al., 2013). When objects are stacked, we find at most a ~ 0.25 dex [O III]/Hβ enhancement in field galaxies compared to cluster galaxies, which is within 2σ uncertainty. We find higher-mass ($M_* > 10.1$) stacks in both UDS and COSMOS to have an enhanced Hα/[N II] ratio compared to low-mass objects ($M_* > 10.1$), in both the cluster and field environments.

With this analysis, we can conclude that at $z > 1.5$, galaxies associated with the cluster environment do not display a metallicity enhancement relative to field galaxies. However, cluster galaxies display a ~ 0.2 dex lower offset in $\log$([O III]/Hβ) from field galaxies at comparable redshifts. The explanation of this offset remains for future work, but we speculate it is due to the shutoff of cold-mode gas accretion to cluster galaxies, or a decrease in ionization parameter due to larger sizes observed in cluster galaxies. Further observations of galaxy clusters are needed to confirm our results, particularly clusters at $z \sim 1.5$, where simulations in Illustris-TNG predicts a metallicity enhancement occurs in dense environments.

5. SUMMARY AND CONCLUSIONS

In this work, I have studied the properties of galaxies in proto-clusters at $z \sim 2$. Based on observations of environmental effects on members of galaxy clusters at $z = 0$, we hypothesized that the cluster environment would effect the evolution of its members starting during its formation. At $z \sim 2$, galaxies in clusters, even brightest cluster galaxies, were forming stars rapidly. However, in local clusters, star formation is shut off due to environmental quenching mechanisms like ram-pressure stripping or galaxy strangulation. Local cluster galaxies appear to have more evolved stellar populations, therefore we test to see if the cluster environment causes a more rapid evolution in star-forming galaxies to explain the prevalence of galaxies with older stellar populations in clusters at local redshifts. Additionally, we measure the nebular gas properties of cluster galaxies to determine if there are signals of chemical pre-processing or differing ionization conditions from the field. These observations provide constraints on the effect of environment on cluster galaxies at early points in the development of a cluster.

5.1 The Kinematics of Star-Forming Galaxies at $z \sim 2$ as a Function of Environment

We have observed the Hα kinematics of galaxies in the cluster environment at $z = 2.095$ in COSMOS. Hα was used because it is a very bright emission line, and is the result of star formation. At $z \sim 2$ it is observed in both cluster and field galaxies, so it allows us to directly compare kinematic properties of both populations. We measured the width of the emission line and converted this width to an integrated gas velocity dispersion ($\sigma_{\rm int}$), accounting for both velocity and dispersion in this kinematic measurement. We found no significant differences in the velocity dispersions of cluster and field galaxies, and velocity dispersion measurements of other star-forming galaxies in the field at $z \sim 2$.

The integrated velocity dispersion measurements can be used to trace the gravitational potential of a galaxy. We used these measurements of $\sigma_{\rm int}$ to measure the dynamical mass (dark matter and baryonic matter) of the internal effective radius of our galaxies, assuming a spherical matter distribution. We did not correct for inclination or offset of the kinematic axis and the slit position angle because we did not want to make further assumptions of the galaxy's morphology. We found no variations between the overall kinematics of cluster and field galaxies. When we used $\sigma_{\rm int}$ to estimate dynamical masses, we again found no significant differences from field galaxies.

Kinematics were measured using the Hα emission line, so we extracted Hα fluxes, and used the fluxes to estimate the gas mass of a galaxy from the Kennicutt-Schmidt Law (Kennicutt, 1998). Again we found no significant differences between cluster and field galaxies, but we were also able to determine that within 1 effective radius (1-2 kiloparsecs), the mass of an SFG was dominated by baryonic matter.

5.2 The 3D Kinematics of Star-Forming Galaxies at $z \sim 2$

We continued our work by investigating the contributions of velocity ($V_{2.2}$) and velocity dispersion (σ_g) and their relationship to morphology. Our hypothesis was that if clumpy or irregular morphology in the COSMOS population was caused by merging or gravitational instabilities due to high gas fractions, we would see a larger scatter around kinematic scaling relations and in angular momentum values for irregular galaxies than regular galaxies. Studies at $z > 0.7$ have shown a larger scatter of angular momentum values in recent merger galaxies (Puech et al., 2007). This hypothesis assumed a stochastic variation in the orientations of mergers and gas accretion, as the angular momentum gain or loss is dependent on the orientation.

We used HELA modeling to extract the rotation curves and constant gas velocity dispersion of our galaxy populations. Modeling using simulated emission lines generated by Bekiaris et al. (2016) showed that we recover $V_{2.2}$ to an offset of $> 10\%$ of the input, and within 2% for σ_g. However we recover our kinematic indicators S$_{0.5}$ and j_{disk} (specific angular momentum) reliably. We found no increase in scatter around the S$_{0.5}$ scaling relation in irregulars compared to regulars, or in any other kinematic scaling relation. Our results were consistent with Simons et al. (2017) who found an increase in $V_{2.2}/\sigma_g$, but modeling showed our recovery in $V_{2.2}/\sigma_g$ was likely unreliable.

Our most compelling result was the result of a two-population Kolmogorov - Smirnov test on the specific angular momentum values of irregular and regular galaxies. We found that irregular galaxies had higher j_{disk} values than regular galaxies to a 90% confidence value. This contradicted our hypothesis as we found greater scatter in angular momentum values in regular galaxies. What we propose is the explanation for this that either we are unable to resolve the clumpy structure in low-mass SFGs, or the accretion and merging events that cause these structures are not happening at random orientations. Further observations are needed to follow up these results, including measurements of possible metallicity gradients, spatial information from IFUs, or simply larger datasets of cluster and field galaxies, to see if there is an environmental or Cosmic Web component.

5.3 Nebular Gas Properties and Gas-Phase Metallicities of Star-Forming Galaxies at $z \sim 2$

We complete our study of galaxy properties within proto-clusters by studying two proto-clusters. The first cluster is the COSMOS cluster which was the focus of our investigation in Chapters 2 and 3. We add the second cluster, in UDS at $z = 1.62$, for our analysis of nebular gas properties of proto-clusters. We also add more observations of emission lines of galaxies in COSMOS from our previous ionized gas measurements of Kewley et al. (2015), and perform an analysis of gas-phase metallicity using a strong line metallicity indicator modeled to be insensitive to the effects of ionization parameter and electron density (Dopita et al., 2016).

Our metallicity indicator required flux measurements of the [S II] emission line doublet, a very faint emission line, so for most of our objects, we found flux limits of the [S II] lines. We found no offsets between cluster and field, or between the COSMOS and UDS populations using either the Dopita et al. (2016) indicator or the Pettini and Pagel (2004) indicator in wider use. We do find that the Dopita et al. (2016) values were highly scattered due to faint emission line measurements and high sky noise. Our results confirm predictions made by IllustrisTNG on the redshifts when chemical pre-processing signatures are found in the gas-phase metallicity of star-forming galaxies in clusters (Gupta et al., 2018; Torrey et al., 2018)

With no indication of environmental effects on gas-phase metallicity, confirming the results of Kacprzak et al. (2015); Tran et al. (2015), we can perform a BPT analysis to determine nebular gas properties of our galaxies. We find that the UDS population has a lower $\log([\mathrm{O\,III}]/\mathrm{H}\beta)$ ratio than the COSMOS population, likely due to the increase in ionization parameter at higher redshift (Kewley et al., 2013; Shapley et al., 2015). Additionally we find that by stacking by environment and mass within environmental samples, we find a ~ 0.3 dex offset between cluster and field galaxies in both samples, where cluster galaxies have a lower $\log([\mathrm{O\,III}]/\mathrm{H}\beta)$ ratio than the field. The cluster galaxies had consistent $\log([\mathrm{O\,III}]/\mathrm{H}\beta)$ values with the $z = 0$ SDSS sample, and field galaxies were consistent with other $z \sim 2$ studies (Sanders et al., 2018).

We speculate that this offset is the result of the larger sizes of galaxies in proto-clusters at $z \sim 2$ (Allen et al., 2015) with similar SFRs between cluster and field galaxies (Tran et al., 2017). This would cause a lower ionizing flux per unit volume, which would be a lower ionization parameter, and decrease the $\log([\mathrm{O\,III}]/\mathrm{H}\beta)$ ratio of the cluster samples. Alternatively, the high $\log([\mathrm{O\,III}]/\mathrm{H}\beta)$ ratio in the field galaxies compared to the cluster could be the result of shocks from cold-mode accretion. The cluster environment would be forming the ICM, which would heat infalling gas before going through the virial radius of cluster galaxies, and would dampen any temperature-based shock. Both these explanations require further investigation, but are the first indication of an environmental effect on the nebular gas properties of galaxies in proto-clusters.

5.4 Further Study

The most prominent challenges in the field of galaxy evolution within clusters across cosmic time include small sample size, spatial resolution, sky emission, and lack of simulation predictions. Space-based and adaptive optics observations will provide spatially resolved kinematics and allow for greater modeling of the complex kinematics of high-redshift and merging galaxies. Additionally, greater spatial resolution will be useful for detecting metallicity gradients, which will be useful in correlating kinematics and gas accretion. More clusters must be identified before concluding that the results in this work are typical of proto-clusters at $z > 1.5$. More clusters at varying redshifts will pinpoint the epochs of environmental effects in the growth of a cluster. Finally, a greater emphasis on identifying the simulated predictions of physical properties and their relationship to environment (kinematics, metallicity, gas temperature and ionization conditions) will help us understand the direct evolutionary tracks of galaxies within proto-clusters.

5.4.1 On Kinematics and Environment

Following up on my previous research, I am interested in exploring the connection between kinematics and the processes which build the gas reservoirs of galaxies. An open question in the study of how galaxies build their gas mass is how gas accretes onto a galaxy. Does the gas accrete through flows from filamentary structures? Or does it fall onto the disk randomly from the circumgalactic medium? Are wet (gas-rich) mergers a dominant or minor mechanism of this growth? Accretion of gas from the circumgalactic medium and through filaments (Kereš et al., 2005; Danovich et al., 2015), and similarly major and minor mergers (Rodriguez-Gomez et al., 2017), leave indications in the gas kinematics of a galaxy.

While our simulated kinematic properties $\mathrm{S}_{0.5}$ and j_{disk} were recovered to a high level of accuracy (within 5% of the input kinematics, Appendix B), we believe follow-up observations of our sample are necessary. It is worthwhile to determine if we measure consistent values of rotation and dispersion with IFU spectroscopy of galaxies within our sample. OSIRIS, NIFS, or KMOS measurements of the gas kinematics of the ZFIRE sample would allow us to determine if we are consistent or offset from IFU observations. If there is an offset, then there is a need to develop more complex kinematic models. If we are consistent with IFU observations, then we can reliably build large samples of $z \sim 2$ galaxies with multi-slit spectrographs.

Our kinematics relied on a number of assumptions, and our modeling could be improved with a few modifications if we find our recovered kinematics are offset from IFU spectroscopy. In our models, we assume an arctangent rotation curve, a constant velocity dispersion, and an infinitely thin disk. We could remove the assumption of an infinitely thin disk, and add a thickness to the disk. Once that is done, it could be possible to modify our velocity dispersion so it is not constant through the disk. The amount of variation will likely depend on the resolution of the instrument. Alternatives to the arctangent rotation curve could also be used, for example, the falling rotation curves observed by Lang et al. (2017).

A full-scale study of these questions on the nature of gas accretion is a worthwhile exploration. It is valuable to explore a large sample of local spatially resolved galaxies (or as resolved as possible for high-z galaxies) with spatial and spectral data. The SAMI instrument, KMOS, OSIRIS, and NIFS would provide the best current datasets for exploring the relationship between gas kinematics and environment. In the future, HECTOR, GIRMOS, and JWST will similarly provide large datasets useful for these studies. A knowledge of proto-cluster structures, galaxy spatial distribution within a cluster, metallicity gradients, and modeling complex kinematics will greatly enhance our knowledge of how galaxies build their gas reservoirs and how the environment affects these processes.

5.4.2 On Ionized Gas and Environment

The cause of the offset between cluster and field galaxies at $z = 1.62$ and $z = 2.1$ is still unknown. It is advisable to measure the gas mass directly from the galaxies in the COSMOS and UDS samples using ALMA, rather than estimating from the Kennicutt-Schmidt Law. With this data, we could determine if the ionizing flux does remain the same between cluster and field, while sizes of cluster galaxies increase. Alternatively, one could test the accretion shock theory by trying to measure the temperature of the ICM in the COSMOS and UDS clusters against the CGM gas surrounding field galaxies, or the temperature of gas in their filaments.

REFERENCES

Alcorn, L. Y., Tran, K.-V. H., Kacprzak, G. G., Nanayakkara, T., Straatman, C., Yuan, T., Allen, R. J., Cowley, M., Davé, R., Glazebrook, K., Kewley, L. J., Labbé, I., Quadri, R., Spitler, L. R., and Tomczak, A. (2016). ZFIRE: The Kinematics of Star-forming Galaxies as a Function of Environment at z $\sim$ 2. *The Astrophysical Journal Letters*, 825:L2–L8.

Allen, R. J., Kacprzak, G. G., Spitler, L. R., Glazebrook, K., Labbé, I., Tran, K.-V. H., Straatman, C. M. S., Nanayakkara, T., Brammer, G. B., Quadri, R. F., Cowley, M., Monson, A., Papovich, C., Persson, S. E., Rees, G., Tilvi, V., and Tomczak, A. R. (2015). The Differential Size Growth of Field and Cluster Galaxies at z = 2.1 Using the ZFOURGE Survey. *The Astrophysical Journal*, 806:3–14.

Baldwin, J. A., Phillips, M. M., and Terlevich, R. (1981). Classification Parameters for the Emission-Line Spectra of Extragalactic Objects. *Astronomical Society of the Pacific Publications*, 93:5–19.

Barro, G., Trump, J. R., Koo, D. C., Dekel, A., Kassin, S. A., Kocevski, D. D., Faber, S. M., van der Wel, A., Guo, Y., Pérez-González, P. G., Toloba, E., Fang, J. J., Pacifici, C., Simons, R., Campbell, R. D., Ceverino, D., Finkelstein, S. L., Goodrich, B., Kassis, M., Koekemoer, A. M., Konidaris, N. P., Livermore, R. C., Lyke, J. E., Mobasher, B., Nayyeri, H., Peth, M., Primack, J. R., Rizzi, L., Somerville, R. S., Wirth, G. D., and Zolotov, A. (2014). Keck-I MOSFIRE Spectroscopy of Compact Star-forming Galaxies at z $>\sim$ 2: High Velocity Dispersions in Progenitors of Compact Quiescent Galaxies. *The Astrophysical Journal*, 795:145–157.

Bassett, R., Glazebrook, K., Fisher, D. B., Green, A. W., Wisnioski, E., Obreschkow, D., Cooper, E. M., Abraham, R. G., Damjanov, I., and McGregor, P. J. (2014). DYNAMO - II. Coupled Stellar and Ionized-Gas Kinematics in Two Low-Redshift Clumpy Discs. *Monthly Notices of the Royal Astronomical Society*, 442:3206–3221.

Bassett, R., Papovich, C., Lotz, J. M., Bell, E. F., Finkelstein, S. L., Newman, J. A., Tran, K.-

V., Almaini, O., Lani, C., Cooper, M., Croton, D., Dekel, A., Ferguson, H. C., Kocevski, D. D., Koekemoer, A. M., Koo, D. C., McGrath, E. J., McIntosh, D. H., and Wechsler, R. (2013). CANDELS Observations of the Environmental Dependence of the Color-Mass-Morphology Relation at z = 1.6. *The Astrophysical Journal*, 770:58–75.

Bekiaris, G., Glazebrook, K., Fluke, C. J., and Abraham, R. (2016). Kinematic Modelling of Disc Galaxies Using Graphics Processing Units. *Monthly Notices of the Royal Astronomical Society*, 455:754–784.

Bertin, E. and Arnouts, S. (1996). SExtractor: Software for Source Extraction. *Astronomy and Astrophysics Supplement*, 117:393–404.

Bösch, B., Böhm, A., Wolf, C., Aragón-Salamanca, A., Ziegler, B. L., Barden, M., Gray, M. E., Balogh, M., Meisenheimer, K., and Schindler, S. (2013). Tully-Fisher Analysis of the Multiple Cluster System Abell 901/902. *Astronomy & Astrophysics*, 554:97–112.

Brodwin, M., Stanford, S. A., Gonzalez, A. H., Zeimann, G. R., Snyder, G. F., Mancone, C. L., Pope, A., Eisenhardt, P. R., Stern, D., Alberts, S., Ashby, M. L. N., Brown, M. J. I., Chary, R.-R., Dey, A., Galametz, A., Gettings, D. P., Jannuzi, B. T., Miller, E. D., Moustakas, J., and Moustakas, L. A. (2013). The Era of Star Formation in Galaxy Clusters. *The Astrophysical Journal*, 779:138–153.

Bruzual, G. and Charlot, S. (2003). Stellar Population Synthesis at the Resolution of 2003. *Monthly Notices of the Royal Astronomical Society*, 344:1000–1028.

Burkert, A., Förster Schreiber, N. M., Genzel, R., Lang, P., Tacconi, L. J., Wisnioski, E., Wuyts, S., Bandara, K., Beifiori, A., Bender, R., Brammer, G., Chan, J., Davies, R., Dekel, A., Fabricius, M., Fossati, M., Kulkarni, S., Lutz, D., Mendel, J. T., Momcheva, I., Nelson, E. J., Naab, T., Renzini, A., Saglia, R., Sharples, R. M., Sternberg, A., Wilman, D., and Wuyts, E. (2016). The Angular Momentum Distribution and Baryon Content of Star-forming Galaxies at z $\sim$ 1-3. *The Astrophysical Journal*, 826:214–235.

Calzetti, D., Armus, L., Bohlin, R. C., Kinney, A. L., Koornneef, J., and Storchi-Bergmann, T. (2000). The Dust Content and Opacity of Actively Star-forming Galaxies. *The Astro-*

physical Journal, 533:682–695.

Capak, P., Aussel, H., Ajiki, M., McCracken, H. J., Mobasher, B., Scoville, N., Shopbell, P., Taniguchi, Y., Thompson, D., Tribiano, S., Sasaki, S., Blain, A. W., Brusa, M., Carilli, C., Comastri, A., Carollo, C. M., Cassata, P., Colbert, J., Ellis, R. S., Elvis, M., Giavalisco, M., Green, W., Guzzo, L., Hasinger, G., Ilbert, O., Impey, C., Jahnke, K., Kartaltepe, J., Kneib, J.-P., Koda, J., Koekemoer, A., Komiyama, Y., Leauthaud, A., Le Fevre, O., Lilly, S., Liu, C., Massey, R., Miyazaki, S., Murayama, T., Nagao, T., Peacock, J. A., Pickles, A., Porciani, C., Renzini, A., Rhodes, J., Rich, M., Salvato, M., Sanders, D. B., Scarlata, C., Schiminovich, D., Schinnerer, E., Scodeggio, M., Sheth, K., Shioya, Y., Tasca, L. A. M., Taylor, J. E., Yan, L., and Zamorani, G. (2007). The First Release COSMOS Optical and Near-IR Data and Catalog. *The Astrophysical Journal Supplements*, 172:99–116.

Cappellari, M., Emsellem, E., Krajnović, D., McDermid, R. M., Serra, P., Alatalo, K., Blitz, L., Bois, M., Bournaud, F., Bureau, M., Davies, R. L., Davis, T. A., de Zeeuw, P. T., Khochfar, S., Kuntschner, H., Lablanche, P.-Y., Morganti, R., Naab, T., Oosterloo, T., Sarzi, M., Scott, N., Weijmans, A.-M., and Young, L. M. (2011). The ATLAS^{3D} Project - VII. A New Look at the Morphology of Nearby Galaxies: The Kinematic Morphology-Density Relation. *Monthly Notices of the Royal Astronomical Society*, 416:1680–1696.

Cardelli, J. A., Clayton, G. C., and Mathis, J. S. (1989). The Relationship Between Infrared, Optical, and Ultraviolet Extinction. *The Astrophysical Journal*, 345:245–256.

Chabrier, G. (2003). Galactic Stellar and Substellar Initial Mass Function. *PASP*, 115:763–795.

Cooper, M. C., Tremonti, C. A., Newman, J. A., and Zabludoff, A. I. (2008). The Role of Environment in the Mass-Metallicity Relation. *Monthly Notices of the Royal Astronomical Society*, 390:245–256.

Cortese, L., Fogarty, L. M. R., Bekki, K., van de Sande, J., Couch, W., Catinella, B., Colless, M., Obreschkow, D., Taranu, D., Tescari, E., Barat, D., Bland-Hawthorn, J., Bloom, J., Bryant, J. J., Cluver, M., Croom, S. M., Drinkwater, M. J., d'Eugenio, F., Konstantopoulos, I. S., Lopez-Sanchez, A., Mahajan, S., Scott, N., Tonini, C., Wong, O. I., Allen, J. T., Brough, S., Goodwin, M., Green, A. W., Ho, I.-T., Kelvin, L. S., Lawrence, J. S., Lorente, N. P. F., Medling, A. M., Owers, M. S., Richards, S., Sharp, R., and Sweet, S. M. (2016). The SAMI Galaxy Survey: The Link Between Angular Momentum and Optical Morphology. *Monthly Notices of the Royal Astronomical Society*, 463:170–184.

Cowley, M. J., Spitler, L. R., Tran, K.-V. H., Rees, G. A., Labbé, I., Allen, R. J., Brammer, G. B., Glazebrook, K., Hopkins, A. M., Juneau, S., Kacprzak, G. G., Mullaney, J. R., Nanayakkara, T., Papovich, C., Quadri, R. F., Straatman, C. M. S., Tomczak, A. R., and van Dokkum, P. G. (2016). ZFOURGE Catalogue of AGN Candidates: An Enhancement of 160-μm-Derived Star Formation Rates in Active Galaxies to z = 3.2. *Monthly Notices of the Royal Astronomical Society*, 457:629–641.

Cresci, G., Hicks, E. K. S., Genzel, R., Schreiber, N. M. F., Davies, R., Bouché, N., Buschkamp, P., Genel, S., Shapiro, K., Tacconi, L., Sommer-Larsen, J., Burkert, A., Eisenhauer, F., Gerhard, O., Lutz, D., Naab, T., Sternberg, A., Cimatti, A., Daddi, E., Erb, D. K., Kurk, J., Lilly, S. L., Renzini, A., Shapley, A., Steidel, C. C., and Caputi, K. (2009). The SINS Survey: Modeling the Dynamics of z $\sim$ 2 Galaxies and the High-z Tully-Fisher Relation. *The Astrophysical Journal*, 697:115–132.

Daddi, E., Bournaud, F., Walter, F., Dannerbauer, H., Carilli, C. L., Dickinson, M., Elbaz, D., Morrison, G. E., Riechers, D., Onodera, M., Salmi, F., Krips, M., and Stern, D. (2010). Very High Gas Fractions and Extended Gas Reservoirs in z = 1.5 Disk Galaxies. *The Astrophysical Journal*, 713:686–707.

Danovich, M., Dekel, A., Hahn, O., Ceverino, D., and Primack, J. (2015). Four Phases of Angular-Momentum Buildup in High-z Galaxies: From Cosmic-Web Streams Through an Extended Ring to Disc and Bulge. *Monthly Notices of the Royal Astronomical Society*, 449:2087–2111.

Di Teodoro, E. M., Fraternali, F., and Miller, S. H. (2016). Flat Rotation Curves and Low Velocity Dispersions in KMOS Star-Forming Galaxies at z $\sim$ 1. *Astronomy & Astrophysics*, 594:A77–A88.

Dopita, M. A., Kewley, L. J., Sutherland, R. S., and Nicholls, D. C. (2016). Chemical Abundances in High-Redshift Galaxies: A Powerful New Emission Line Diagnostic. *Astrophysics and Space Science*, 361:61–68.

Dressler, A. (1980). Galaxy Morphology in Rich Clusters - Implications for the Formation and Evolution of Galaxies. *The Astrophysical Journal*, 236:351–365.

Dutton, A. A., van den Bosch, F. C., Faber, S. M., Simard, L., Kassin, S. A., Koo, D. C., Bundy, K., Huang, J., Weiner, B. J., Cooper, M. C., Newman, J. A., Mozena, M., and Koekemoer, A. M. (2011). On the Evolution of the Velocity-Mass-Size Relations of Disc-Dominated Galaxies Over the Past 10 Billion Years. *Monthly Notices of the Royal Astronomical Society*, 410:1660–1676.

Ebeling, H., Stephenson, L. N., and Edge, A. C. (2014). Jellyfish: Evidence of Extreme Ram-pressure Stripping in Massive Galaxy Clusters. *The Astrophysical Journal Letters*, 781:L40–L45.

El-Badry, K., Quataert, E., Wetzel, A., Hopkins, P. F., Weisz, D. R., Chan, T. K., Fitts, A., Boylan-Kolchin, M., Kereš, D., Faucher-Giguère, C.-A., and Garrison-Kimmel, S. (2018). Gas Kinematics, Morphology and Angular Momentum in the FIRE Simulations. *Monthly Notices of the Royal Astronomical Society*, 473:1930–1955.

Ellison, S. L., Simard, L., Cowan, N. B., Baldry, I. K., Patton, D. R., and McConnachie, A. W. (2009). The Mass-Metallicity Relation in Galaxy Clusters: The Relative Importance of Cluster Membership Versus Local Environment. *Monthly Notices of the Royal Astronomical Society*, 396:1257–1272.

Emsellem, E., Cappellari, M., Krajnović, D., van de Ven, G., Bacon, R., Bureau, M., Davies, R. L., de Zeeuw, P. T., Falcón-Barroso, J., Kuntschner, H., McDermid, R., Peletier, R. F., and Sarzi, M. (2007). The SAURON Project - IX. A Kinematic Classification for Early-Type Galaxies. *Monthly Notices of the Royal Astronomical Society*, 379:401–417.

Epinat, B., Amram, P., and Marcelin, M. (2008). GHASP: An Hα Kinematic Survey of

203 Spiral and Irregular Galaxies - VII. Revisiting the Analysis of Hα Data Cubes for 97 Galaxies. *Monthly Notices of the Royal Astronomical Society*, 390:466–504.

Epinat, B., Contini, T., Le Fèvre, O., Vergani, D., Garilli, B., Amram, P., Queyrel, J., Tasca, L., and Tresse, L. (2009). Integral Field Spectroscopy With SINFONI of VVDS Galaxies. I. Galaxy Dynamics and Mass Assembly at 1.2 $<$ z $<$ 1.6. *AAP*, 504:789–805.

Erb, D. K., Steidel, C. C., Shapley, A. E., Pettini, M., Reddy, N. A., and Adelberger, K. L. (2006). Hα Observations of a Large Sample of Galaxies at z $\sim$ 2: Implications for Star Formation in High-Redshift Galaxies. *The Astrophysical Journal*, 647:128–139.

Fall, S. M. and Efstathiou, G. (1980). Formation and Rotation of Disc Galaxies with Haloes. *Monthly Notices of the Royal Astronomical Society*, 193:189–206.

Foreman-Mackey, D., Hogg, D. W., Lang, D., and Goodman, J. (2013). emcee: The MCMC Hammer. *Publications of the Astronomical Society of the Pacific*, 125:306–312.

Forrest, B., Tran, K.-V. H., Broussard, A., Allen, R. J., Apfel, M., Cowley, M. J., Glazebrook, K., Kacprzak, G. G., Labbé, I., Nanayakkara, T., Papovich, C., Quadri, R. F., Spitler, L. R., Straatman, C. M. S., and Tomczak, A. (2017). Discovery of Extreme [O III]+Hβ Emitting Galaxies Tracing an Overdensity at z $\sim$ 3.5 in CDF-South. *The Astrophysical Journal Letters*, 838:L12–L18.

Forrest, B., Tran, K.-V. H., Tomczak, A. R., Broussard, A., Labbé, I., Papovich, C., Kriek, M., Allen, R. J., Cowley, M., Dickinson, M., Glazebrook, K., van Houdt, J., Inami, H., Kacprzak, G. G., Kawinwanichakij, L., Kelson, D., McCarthy, P. J., Monson, A., Morrison, G., Nanayakkara, T., Persson, S. E., Quadri, R. F., Spitler, L. R., Straatman, C., and Tilvi, V. (2016). UV to IR Luminosities and Dust Attenuation Determined from $\sim$4000 K-selected Galaxies at 1 $<$ z $<$ 3 in the ZFOURGE Survey. *The Astrophysical Journal Letters*, 818:L26–L32.

Förster Schreiber, N. M., Genzel, R., Bouché, N., Cresci, G., Davies, R., Buschkamp, P., Shapiro, K., Tacconi, L. J., Hicks, E. K. S., Genel, S., Shapley, A. E., Erb, D. K., Steidel, C. C., Lutz, D., Eisenhauer, F., Gillessen, S., Sternberg, A., Renzini, A., Cimatti, A., Daddi, E., Kurk, J., Lilly, S., Kong, X., Lehnert, M. D., Nesvadba, N., Verma, A., McCracken, H., Arimoto, N., Mignoli, M., and Onodera, M. (2009). The SINS Survey: SINFONI Integral Field Spectroscopy of z $\sim$ 2 Star-forming Galaxies. *The Astrophysical Journal*, 706:1364–1428.

Freeman, K. C. (1970). On the Disks of Spiral and S0 Galaxies. *The Astrophysical Journal*, 160:811.

Glazebrook, K. (2013). The Dawes Review 1: Kinematic Studies of Star-Forming Galaxies Across Cosmic Time. *Publications of the Astronomical Society of Australia*, 30:56–103.

Gnerucci, A., Marconi, A., Cresci, G., Maiolino, R., Mannucci, F., Calura, F., Cimatti, A., Cocchia, F., Grazian, A., Matteucci, F., Nagao, T., Pozzetti, L., and Troncoso, P. (2011). Dynamical Properties of AMAZE and LSD Galaxies From Gas Kinematics and the Tully-Fisher Relation at z $\sim$ 3. *Astronomy & Astrophysics*, 528:88–111.

Green, A. W., Glazebrook, K., McGregor, P. J., Damjanov, I., Wisnioski, E., Abraham, R. G., Colless, M., Sharp, R. G., Crain, R. A., Poole, G. B., and McCarthy, P. J. (2014). DYNAMO - I. A Sample of Hα-Luminous Galaxies with Resolved Kinematics. *Monthly Notices of the Royal Astronomical Society*, 437:1070–1095.

Grogin, N. A., Kocevski, D. D., Faber, S. M., Ferguson, H. C., Koekemoer, A. M., Riess, A. G., Acquaviva, V., Alexander, D. M., Almaini, O., Ashby, M. L. N., Barden, M., Bell, E. F., Bournaud, F., Brown, T. M., Caputi, K. I., Casertano, S., Cassata, P., Castellano, M., Challis, P., Chary, R.-R., Cheung, E., Cirasuolo, M., Conselice, C. J., Roshan Cooray, A., Croton, D. J., Daddi, E., Dahlen, T., Davé, R., de Mello, D. F., Dekel, A., Dickinson, M., Dolch, T., Donley, J. L., Dunlop, J. S., Dutton, A. A., Elbaz, D., Fazio, G. G., Filippenko, A. V., Finkelstein, S. L., Fontana, A., Gardner, J. P., Garnavich, P. M., Gawiser, E., Giavalisco, M., Grazian, A., Guo, Y., Hathi, N. P., Häussler, B., Hopkins, P. F., Huang, J.-S., Huang, K.-H., Jha, S. W., Kartaltepe, J. S., Kirshner, R. P., Koo, D. C., Lai, K., Lee, K.-S., Li, W., Lotz, J. M., Lucas, R. A., Madau, P., McCarthy, P. J., McGrath, E. J., McIntosh, D. H., McLure, R. J., Mobasher, B., Moustakas, L. A., Mozena, M., Nandra, K., Newman, J. A., Niemi, S.-M., Noeske, K. G., Papovich, C. J., Pentericci, L., Pope, A., Primack, J. R., Rajan, A., Ravindranath, S., Reddy, N. A., Renzini, A., Rix, H.-W., Robaina, A. R., Rodney, S. A., Rosario, D. J., Rosati, P., Salimbeni, S., Scarlata, C., Siana, B., Simard, L., Smidt, J., Somerville, R. S., Spinrad, H., Straughn, A. N., Strolger, L.-G., Telford, O., Teplitz, H. I., Trump, J. R., van der Wel, A., Villforth, C., Wechsler, R. H., Weiner, B. J., Wiklind, T., Wild, V., Wilson, G., Wuyts, S., Yan, H.-J., and Yun, M. S. (2011). CANDELS: The Cosmic Assembly Near-infrared Deep Extragalactic Legacy Survey. *The Astrophysical Journal Supplements*, 197:35–72.

Grootes, M. W., Tuffs, R. J., Popescu, C. C., Norberg, P., Robotham, A. S. G., Liske, J., Andrae, E., Baldry, I. K., Gunawardhana, M., Kelvin, L. S., Madore, B. F., Seibert, M., Taylor, E. N., Alpaslan, M., Brown, M. J. I., Cluver, M. E., Driver, S. P., Bland-Hawthorn, J., Holwerda, B. W., Hopkins, A. M., Lopez-Sanchez, A. R., Loveday, J., and Rushton, M. (2017). Galaxy And Mass Assembly (GAMA): Gas Fueling of Spiral Galaxies in the Local Universe. I. The Effect of the Group Environment on Star Formation in Spiral Galaxies. *The Astronomical Journal*, 153:111–160.

Gupta, A., Yuan, T., Torrey, P., Vogelsberger, M., Martizzi, D., Tran, K.-V. H., Kewley, L. J., Marinacci, F., Nelson, D., Pillepich, A., Hernquist, L., Genel, S., and Springel, V. (2018). Chemical Pre-processing of Cluster Galaxies Over the Past 10 Billion Years in the IllustrisTNG Simulations. *Monthly Notices of the Royal Astronomical Society*, 477:L35–L39.

Harrison, C. M., Johnson, H. L., Swinbank, A. M., Stott, J. P., Bower, R. G., Smail, I., Tiley, A. L., Bunker, A. J., Cirasuolo, M., Sobral, D., Sharples, R. M., Best, P., Bureau, M., Jarvis, M. J., and Magdis, G. (2017). The KMOS Redshift One Spectroscopic Survey (KROSS): Rotational Velocities and Angular Momentum of z = 0.9 Galaxies. *Monthly Notices of the Royal Astronomical Society*, 467:1965–1983.

Houghton, R. C. W. (2015). Revisiting the Original Morphology-Density Relation. *Monthly Notices of the Royal Astronomical Society*, 451:3427–3436.

Hubble, E. P. (1927). The Classification of Spiral Nebulae. *The Observatory*, 50:276–281.

Hung, C.-L., Rich, J. A., Yuan, T., Larson, K. L., Casey, C. M., Smith, H. A., Sanders, D. B., Kewley, L. J., and Hayward, C. C. (2015). Kinematic Classifications of Local Interacting Galaxies: Implications for the Merger/Disk Classifications at High-z. *The Astrophysical Journal*, 803:62–77.

Jarrett, T. H., Cluver, M. E., Magoulas, C., Bilicki, M., Alpaslan, M., Bland-Hawthorn, J., Brough, S., Brown, M. J. I., Croom, S., Driver, S., Holwerda, B. W., Hopkins, A. M., Loveday, J., Norberg, P., Peacock, J. A., Popescu, C. C., Sadler, E. M., Taylor, E. N., Tuffs, R. J., and Wang, L. (2017). Galaxy and Mass Assembly (GAMA): Exploring the WISE Web in G12. *The Astrophysical Journal*, 836:182–210.

Jones, T. A., Swinbank, A. M., Ellis, R. S., Richard, J., and Stark, D. P. (2010). Resolved Spectroscopy of Gravitationally Lensed Galaxies: Recovering Coherent Velocity Fields in Subluminous z $\sim$ 2-3 Galaxies. *Monthly Notices of the Royal Astronomical Society*, 404:1247–1262.

Kacprzak, G. G., van de Voort, F., Glazebrook, K., Tran, K.-V. H., Yuan, T., Nanayakkara, T., Allen, R. J., Alcorn, L., Cowley, M., Labbé, I., Spitler, L., Straatman, C., and Tomczak, A. (2016). Cold-mode Accretion: Driving the Fundamental Mass-Metallicity Relation at z $\sim$ 2. *The Astrophysical Journal Letters*, 826:L11–L17.

Kacprzak, G. G., Yuan, T., Nanayakkara, T., Kobayashi, C., Tran, K.-V. H., Kewley, L. J., Glazebrook, K., Spitler, L., Taylor, P., Cowley, M., Labbe, I., Straatman, C., and Tomczak, A. (2015). The Absence of an Environmental Dependence in the Mass-Metallicity Relation at z = 2. *The Astrophysical Journal Letters*, 802:L26–L31.

Kassin, S. A., Weiner, B. J., Faber, S. M., Koo, D. C., Lotz, J. M., Diemand, J., Harker, J. J., Bundy, K., Metevier, A. J., Phillips, A. C., Cooper, M. C., Croton, D. J., Konidaris, N., Noeske, K. G., and Willmer, C. N. A. (2007). The Stellar Mass Tully-Fisher Relation to z = 1.2 from AEGIS. *The Astrophysical Journal Letters*, 660:L35–L38.

Kawinwanichakij, L., Papovich, C., Quadri, R. F., Glazebrook, K., Kacprzak, G. G., Allen,

R. J., Bell, E. F., Croton, D. J., Dekel, A., Ferguson, H. C., Forrest, B., Grogin, N. A., Guo, Y., Kocevski, D. D., Koekemoer, A. M., Labbé, I., Lucas, R. A., Nanayakkara, T., Spitler, L. R., Straatman, C. M. S., Tran, K.-V. H., Tomczak, A., and van Dokkum, P. (2017). Effect of Local Environment and Stellar Mass on Galaxy Quenching and Morphology at $0.5 < z < 2.0$. *The Astrophysical Journal*, 847:134–155.

Kawinwanichakij, L., Papovich, C., Quadri, R. F., Tran, K.-V. H., Spitler, L. R., Kacprzak, G. G., Labbé, I., Straatman, C. M. S., Glazebrook, K., Allen, R., Cowley, M., Davé, R., Dekel, A., Ferguson, H. C., Hartley, W. G., Koekemoer, A. M., Koo, D. C., Lu, Y., Mehrtens, N., Nanayakkara, T., Persson, S. E., Rees, G., Salmon, B., Tilvi, V., Tomczak, A. R., and van Dokkum, P. (2014). The Distribution of Satellites around Massive Galaxies at $1 < z < 3$ in ZFOURGE/CANDELS: Dependence on Star Formation Activity. *The Astrophysical Journal*, 792:103–122.

Kawinwanichakij, L., Quadri, R. F., Papovich, C., Kacprzak, G. G., Labbé, I., Spitler, L. R., Straatman, C. M. S., Tran, K.-V. H., Allen, R., Behroozi, P., Cowley, M., Dekel, A., Glazebrook, K., Hartley, W. G., Kelson, D. D., Koo, D. C., Lee, S.-K., Lu, Y., Nanayakkara, T., Persson, S. E., Primack, J., Tilvi, V., Tomczak, A. R., and van Dokkum, P. (2016). Satellite Quenching and Galactic Conformity at $0.3 < z < 2.5$. *The Astrophysical Journal*, 817:9–28.

Kennicutt, Jr., R. C. (1998). The Global Schmidt Law in Star-forming Galaxies. *The Astrophysical Journal*, 498:541–552.

Kereš, D., Katz, N., Weinberg, D. H., and Davé, R. (2005). How Do Galaxies Get Their Gas? *Monthly Notices of the Royal Astronomical Society*, 363:2–28.

Kewley, L. J., Dopita, M. A., Leitherer, C., Davé, R., Yuan, T., Allen, M., Groves, B., and Sutherland, R. (2013). Theoretical Evolution of Optical Strong Lines across Cosmic Time. *The Astrophysical Journal*, 774:100–117.

Kewley, L. J., Zahid, H. J., Geller, M. J., Dopita, M. A., Hwang, H. S., and Fabricant, D. (2015). A Rise in the Ionizing Photons in Star-forming Galaxies over the Past 8 Billion

Years. *The Astrophysical Journal Letters*, 812:L20–L25.

Koekemoer, A. M., Faber, S. M., Ferguson, H. C., Grogin, N. A., Kocevski, D. D., Koo, D. C., Lai, K., Lotz, J. M., Lucas, R. A., McGrath, E. J., Ogaz, S., Rajan, A., Riess, A. G., Rodney, S. A., Strolger, L., Casertano, S., Castellano, M., Dahlen, T., Dickinson, M., Dolch, T., Fontana, A., Giavalisco, M., Grazian, A., Guo, Y., Hathi, N. P., Huang, K.-H., van der Wel, A., Yan, H.-J., Acquaviva, V., Alexander, D. M., Almaini, O., Ashby, M. L. N., Barden, M., Bell, E. F., Bournaud, F., Brown, T. M., Caputi, K. I., Cassata, P., Challis, P. J., Chary, R.-R., Cheung, E., Cirasuolo, M., Conselice, C. J., Roshan Cooray, A., Croton, D. J., Daddi, E., Davé, R., de Mello, D. F., de Ravel, L., Dekel, A., Donley, J. L., Dunlop, J. S., Dutton, A. A., Elbaz, D., Fazio, G. G., Filippenko, A. V., Finkelstein, S. L., Frazer, C., Gardner, J. P., Garnavich, P. M., Gawiser, E., Gruetzbauch, R., Hartley, W. G., Häussler, B., Herrington, J., Hopkins, P. F., Huang, J.-S., Jha, S. W., Johnson, A., Kartaltepe, J. S., Khostovan, A. A., Kirshner, R. P., Lani, C., Lee, K.-S., Li, W., Madau, P., McCarthy, P. J., McIntosh, D. H., McLure, R. J., McPartland, C., Mobasher, B., Moreira, H., Mortlock, A., Moustakas, L. A., Mozena, M., Nandra, K., Newman, J. A., Nielsen, J. L., Niemi, S., Noeske, K. G., Papovich, C. J., Pentericci, L., Pope, A., Primack, J. R., Ravindranath, S., Reddy, N. A., Renzini, A., Rix, H.-W., Robaina, A. R., Rosario, D. J., Rosati, P., Salimbeni, S., Scarlata, C., Siana, B., Simard, L., Smidt, J., Snyder, D., Somerville, R. S., Spinrad, H., Straughn, A. N., Telford, O., Teplitz, H. I., Trump, J. R., Vargas, C., Villforth, C., Wagner, C. R., Wandro, P., Wechsler, R. H., Weiner, B. J., Wiklind, T., Wild, V., Wilson, G., Wuyts, S., and Yun, M. S. (2011). CANDELS: The Cosmic Assembly Near-infrared Deep Extragalactic Legacy Survey - The Hubble Space Telescope Observations, Imaging Data Products, and Mosaics. *The Astrophysical Journal Supplements*, 197:36–72.

Kriek, M., van Dokkum, P. G., Labbé, I., Franx, M., Illingworth, G. D., Marchesini, D., and Quadri, R. F. (2009). An Ultra-Deep Near-Infrared Spectrum of a Compact Quiescent Galaxy at z = 2.2. *The Astrophysical Journal*, 700:221–231.

Krumholz, M. R., Burkhart, B., Forbes, J. C., and Crocker, R. M. (2018). A Unified Model for Galactic Discs: Star Formation, Turbulence Driving, and Mass Transport. *Monthly Notices of the Royal Astronomical Society*, 477:2716–2740.

Lagos, C. d. P., Theuns, T., Stevens, A. R. H., Cortese, L., Padilla, N. D., Davis, T. A., Contreras, S., and Croton, D. (2017). Angular Momentum Evolution of Galaxies in EAGLE. *Monthly Notices of the Royal Astronomical Society*, 464:3850–3870.

Lang, P., Förster Schreiber, N. M., Genzel, R., Wuyts, S., Wisnioski, E., Beifiori, A., Belli, S., Bender, R., Brammer, G., Burkert, A., Chan, J., Davies, R., Fossati, M., Galametz, A., Kulkarni, S. K., Lutz, D., Mendel, J. T., Momcheva, I. G., Naab, T., Nelson, E. J., Saglia, R. P., Seitz, S., Tacchella, S., Tacconi, L. J., Tadaki, K.-i., Übler, H., van Dokkum, P. G., and Wilman, D. J. (2017). Falling Outer Rotation Curves of Star-forming Galaxies at 0.6 < z < 2.6 Probed with KMOS^{3D} and SINS/zC-SINF. *The Astrophysical Journal*, 840:92–116.

Law, D. R., Steidel, C. C., Erb, D. K., Larkin, J. E., Pettini, M., Shapley, A. E., and Wright, S. A. (2009). The Kiloparsec-scale Kinematics of High-redshift Star-forming Galaxies. *The Astrophysical Journal*, 697:2057–2082.

Lawrence, A., Warren, S. J., Almaini, O., Edge, A. C., Hambly, N. C., Jameson, R. F., Lucas, P., Casali, M., Adamson, A., Dye, S., Emerson, J. P., Foucaud, S., Hewett, P., Hirst, P., Hodgkin, S. T., Irwin, M. J., Lodieu, N., McMahon, R. G., Simpson, C., Smail, I., Mortlock, D., and Folger, M. (2007). The UKIRT Infrared Deep Sky Survey (UKIDSS). *Monthly Notices of the Royal Astronomical Society*, 379:1599–1617.

Lewis, I., Balogh, M., De Propris, R., Couch, W., Bower, R., Offer, A., Bland-Hawthorn, J., Baldry, I. K., Baugh, C., Bridges, T., Cannon, R., Cole, S., Colless, M., Collins, C., Cross, N., Dalton, G., Driver, S. P., Efstathiou, G., Ellis, R. S., Frenk, C. S., Glazebrook, K., Hawkins, E., Jackson, C., Lahav, O., Lumsden, S., Maddox, S., Madgwick, D., Norberg, P., Peacock, J. A., Percival, W., Peterson, B. A., Sutherland, W., and Taylor, K. (2002). The 2dF Galaxy Redshift Survey: The Environmental Dependence of Galaxy Star Formation

Rates Near Clusters. *Monthly Notices of the Royal Astronomical Society*, 334:673–683.

Lotz, J. M., Papovich, C., Faber, S. M., Ferguson, H. C., Grogin, N., Guo, Y., Kocevski, D., Koekemoer, A. M., Lee, K.-S., McIntosh, D., Momcheva, I., Rudnick, G., Saintonge, A., Tran, K.-V., van der Wel, A., and Willmer, C. (2013). Caught in the Act: The Assembly of Massive Cluster Galaxies at z = 1.62. *The Astrophysical Journal*, 773:154–164.

Madau, P. and Dickinson, M. (2014). Cosmic Star-Formation History. *Annual Review of Astronomy and Astrophysics*, 52:415–486.

Masters, D., McCarthy, P., Siana, B., Malkan, M., Mobasher, B., Atek, H., Henry, A., Martin, C. L., Rafelski, M., Hathi, N. P., Scarlata, C., Ross, N. R., Bunker, A. J., Blanc, G., Bedregal, A. G., Domínguez, A., Colbert, J., Teplitz, H., and Dressler, A. (2014). Physical Properties of Emission-line Galaxies at z $\sim$ 2 from Near-infrared Spectroscopy with Magellan FIRE. *The Astrophysical Journal*, 785:153–173.

McLean, I. S., Steidel, C. C., Epps, H. W., Konidaris, N., Matthews, K. Y., Adkins, S., Aliado, T., Brims, G., Canfield, J. M., Cromer, J. L., Fucik, J., Kulas, K., Mace, G., Magnone, K., Rodriguez, H., Rudie, G., Trainor, R., Wang, E., Weber, B., and Weiss, J. (2012). MOSFIRE, the Multi-Object Spectrometer for Infra-Red Exploration at the Keck Observatory. In *Ground-based and Airborne Instrumentation for Astronomy IV*, volume 8446 of *Proceedings of the SPIE*, page 84460J.

Miller, S. H., Bundy, K., Sullivan, M., Ellis, R. S., and Treu, T. (2011). The Assembly History of Disk Galaxies. I. The Tully-Fisher Relation to z $\sim=$ 1.3 from Deep Exposures with DEIMOS. *The Astrophysical Journal*, 741:115–135.

Mo, H. J., Mao, S., and White, S. D. M. (1998). The Formation of Galactic Discs. *Monthly Notices of the Royal Astronomical Society*, 295:319–336.

Mocz, P., Green, A., Malacari, M., and Glazebrook, K. (2012). The Tully-Fisher Relation for 25 000 Sloan Digital Sky Survey Galaxies as a Function of Environment. *Monthly Notices of the Royal Astronomical Society*, 425:296–310.

Muzzin, A., van der Burg, R. F. J., McGee, S. L., Balogh, M., Franx, M., Hoekstra, H., Hudson, M. J., Noble, A., Taranu, D. S., Webb, T., Wilson, G., and Yee, H. K. C. (2014). The Phase Space and Stellar Populations of Cluster Galaxies at z $\sim$ 1: Simultaneous Constraints on the Location and Timescale of Satellite Quenching. *The Astrophysical Journal*, 796:65–75.

Naab, T., Oser, L., Emsellem, E., Cappellari, M., Krajnović, D., McDermid, R. M., Alatalo, K., Bayet, E., Blitz, L., Bois, M., Bournaud, F., Bureau, M., Crocker, A., Davies, R. L., Davis, T. A., de Zeeuw, P. T., Duc, P.-A., Hirschmann, M., Johansson, P. H., Khochfar, S., Kuntschner, H., Morganti, R., Oosterloo, T., Sarzi, M., Scott, N., Serra, P., van de Ven, G., Weijmans, A., and Young, L. M. (2014). The ATLAS^{3D} Project - XXV. Two-Dimensional Kinematic Analysis of Simulated Galaxies and the Cosmological Origin of Fast and Slow Rotators. *Monthly Notices of the Royal Astronomical Society*, 444:3357–3387.

Nanayakkara, T., Glazebrook, K., Kacprzak, G. G., Yuan, T., Fisher, D., Tran, K.-V., Kewley, L. J., Spitler, L., Alcorn, L., Cowley, M., Labbe, I., Straatman, C., and Tomczak, A. (2017). ZFIRE: Using Hα Equivalent Widths to Investigate the In Situ Initial Mass Function at z $\sim$ 2. *Monthly Notices of the Royal Astronomical Society*, 468:3071–3108.

Nanayakkara, T., Glazebrook, K., Kacprzak, G. G., Yuan, T., Tran, K.-V., Spitler, L., Kewley, L., Straatman, C., Cowley, M., Fisher, D., Labbe, I., Tomczak, A., Allen, R., and Alcorn, L. (2016). ZFIRE: A KECK/MOSFIRE Spectroscopic Survey of Galaxies in Rich Environments at z $\sim$ 2. *The Astrophysical Journal*, 828:21–47.

Nelson, E. J., van Dokkum, P. G., Förster Schreiber, N. M., Franx, M., Brammer, G. B., Momcheva, I. G., Wuyts, S., Whitaker, K. E., Skelton, R. E., Fumagalli, M., Hayward, C. C., Kriek, M., Labbé, I., Leja, J., Rix, H.-W., Tacconi, L. J., van der Wel, A., van den Bosch, F. C., Oesch, P. A., Dickey, C., and Ulf Lange, J. (2016). Where Stars Form: Inside-out Growth and Coherent Star Formation from HST Hα Maps of 3200 Galaxies across the Main Sequence at $0.7 < z < 1.5$. *The Astrophysical Journal*, 828:27–51.

Newman, S. F., Genzel, R., Förster-Schreiber, N. M., Shapiro Griffin, K., Mancini, C., Lilly, S. J., Renzini, A., Bouché, N., Burkert, A., Buschkamp, P., Carollo, C. M., Cresci, G., Davies, R., Eisenhauer, F., Genel, S., Hicks, E. K. S., Kurk, J., Lutz, D., Naab, T., Peng, Y., Sternberg, A., Tacconi, L. J., Vergani, D., Wuyts, S., and Zamorani, G. (2012). The SINS/zC-SINF Survey of z $\sim$ 2 Galaxy Kinematics: Outflow Properties. *The Astrophysical Journal*, 761:43–50.

Obreschkow, D. and Glazebrook, K. (2014). Fundamental Mass-Spin-Morphology Relation Of Spiral Galaxies. *The Astrophysical Journal*, 784:26–44.

Obreschkow, D., Glazebrook, K., Bassett, R., Fisher, D. B., Abraham, R. G., Wisnioski, E., Green, A. W., McGregor, P. J., Damjanov, I., Popping, A., and Jørgensen, I. (2015). Low Angular Momentum in Clumpy, Turbulent Disk Galaxies. *The Astrophysical Journal*, 815:97–106.

Obreschkow, D., Glazebrook, K., Kilborn, V., and Lutz, K. (2016). Angular Momentum Regulates Atomic Gas Fractions of Galactic Disks. *The Astrophysical Journal Letters*, 824:L26–L31.

Papovich, C., Bassett, R., Lotz, J. M., van der Wel, A., Tran, K.-V., Finkelstein, S. L., Bell, E. F., Conselice, C. J., Dekel, A., Dunlop, J. S., Guo, Y., Faber, S. M., Farrah, D., Ferguson, H. C., Finkelstein, K. D., Häussler, B., Kocevski, D. D., Koekemoer, A. M., Koo, D. C., McGrath, E. J., McLure, R. J., McIntosh, D. H., Momcheva, I., Newman, J. A., Rudnick, G., Weiner, B., Willmer, C. N. A., and Wuyts, S. (2012). CANDELS Observations of the Structural Properties of Cluster Galaxies at z = 1.62. *The Astrophysical Journal*, 750:93–107.

Papovich, C., Kawinwanichakij, L., Quadri, R. F., Glazebrook, K., Labbé, I., Tran, K.-V. H., Forrest, B., Kacprzak, G. G., Spitler, L. R., Straatman, C. M. S., and Tomczak, A. R. (2018). The Effects of Environment on the Evolution of the Galaxy Stellar Mass Function. *The Astrophysical Journal*, 854:30–44.

Papovich, C., Labbé, I., Quadri, R., Tilvi, V., Behroozi, P., Bell, E. F., Glazebrook, K., Spitler, L., Straatman, C. M. S., Tran, K.-V., Cowley, M., Davé, R., Dekel, A., Dickinson, M., Ferguson, H. C., Finkelstein, S. L., Gawiser, E., Inami, H., Faber, S. M., Kacprzak,

G. G., Kawinwanichakij, L., Kocevski, D., Koekemoer, A., Koo, D. C., Kurczynski, P., Lotz, J. M., Lu, Y., Lucas, R. A., McIntosh, D., Mehrtens, N., Mobasher, B., Monson, A., Morrison, G., Nanayakkara, T., Persson, S. E., Salmon, B., Simons, R., Tomczak, A., van Dokkum, P., Weiner, B., and Willner, S. P. (2015). ZFOURGE/CANDELS: On the Evolution of M* Galaxy Progenitors from z = 3 to 0.5. *The Astrophysical Journal*, 803:26–50.

Papovich, C., Momcheva, I., Willmer, C. N. A., Finkelstein, K. D., Finkelstein, S. L., Tran, K.-V., Brodwin, M., Dunlop, J. S., Farrah, D., Khan, S. A., Lotz, J., McCarthy, P., McLure, R. J., Rieke, M., Rudnick, G., Sivanandam, S., Pacaud, F., and Pierre, M. (2010). A Spitzer-selected Galaxy Cluster at z = 1.62. *The Astrophysical Journal*, 716:1503–1513.

Peng, C. Y., Ho, L. C., Impey, C. D., and Rix, H.-W. (2010). Detailed Decomposition of Galaxy Images. II. Beyond Axisymmetric Models. *The Astrophysical Journal*, 139:2097–2129.

Penoyre, Z., Moster, B. P., Sijacki, D., and Genel, S. (2017). The Origin and Evolution of Fast and Slow Rotators in the Illustris Simulation. *Monthly Notices of the Royal Astronomical Society*, 468:3883–3906.

Pettini, M. and Pagel, B. E. J. (2004). [OIII]/[NII] as an Abundance Indicator at High Redshift. *Monthly Notices of the Royal Astronomical Society*, 348:L59–L63.

Planck Collaboration, Aghanim, N., Akrami, Y., Ashdown, M., Aumont, J., Baccigalupi, C., Ballardini, M., Banday, A. J., Barreiro, R. B., Bartolo, N., Basak, S., Battye, R., Benabed, K., Bernard, J.-P., Bersanelli, M., Bielewicz, P., Bock, J. J., Bond, J. R., Borrill, J., Bouchet, F. R., Boulanger, F., Bucher, M., Burigana, C., Butler, R. C., Calabrese, E., Cardoso, J.-F., Carron, J., Challinor, A., Chiang, H. C., Chluba, J., Colombo, L. P. L., Combet, C., Contreras, D., Crill, B. P., Cuttaia, F., de Bernardis, P., de Zotti, G., Delabrouille, J., Delouis, J.-M., Di Valentino, E., Diego, J. M., Doré, O., Douspis, M., Ducout, A., Dupac, X., Dusini, S., Efstathiou, G., Elsner, F., Enßlin, T. A., Eriksen, H. K., Fantaye, Y., Farhang, M., Fergusson, J., Fernandez-Cobos, R., Finelli, F., Forastieri, F., Frailis, M., Franceschi, E., Frolov, A., Galeotta, S., Galli, S., Ganga, K., Génova-Santos, R. T., Gerbino, M., Ghosh, T., González-Nuevo, J., Górski, K. M., Gratton, S., Gruppuso, A., Gudmundsson, J. E., Hamann, J., Handley, W., Herranz, D., Hivon, E., Huang, Z., Jaffe, A. H., Jones, W. C., Karakci, A., Keihänen, E., Keskitalo, R., Kiiveri, K., Kim, J., Kisner, T. S., Knox, L., Krachmalnicoff, N., Kunz, M., Kurki-Suonio, H., Lagache, G., Lamarre, J.-M., Lasenby, A., Lattanzi, M., Lawrence, C. R., Le Jeune, M., Lemos, P., Lesgourgues, J., Levrier, F., Lewis, A., Liguori, M., Lilje, P. B., Lilley, M., Lindholm, V., López-Caniego, M., Lubin, P. M., Ma, Y.-Z., Macías-Pérez, J. F., Maggio, G., Maino, D., Mandolesi, N., Mangilli, A., Marcos-Caballero, A., Maris, M., Martin, P. G., Martinelli, M., Martínez-González, E., Matarrese, S., Mauri, N., McEwen, J. D., Meinhold, P. R., Melchiorri, A., Mennella, A., Migliaccio, M., Millea, M., Mitra, S., Miville-Deschênes, M.-A., Molinari, D., Montier, L., Morgante, G., Moss, A., Natoli, P., Nørgaard-Nielsen, H. U., Pagano, L., Paoletti, D., Partridge, B., Patanchon, G., Peiris, H. V., Perrotta, F., Pettorino, V., Piacentini, F., Polastri, L., Polenta, G., Puget, J.-L., Rachen, J. P., Reinecke, M., Remazeilles, M., Renzi, A., Rocha, G., Rosset, C., Roudier, G., Rubiño-Martín, J. A., Ruiz-Granados, B., Salvati, L., Sandri, M., Savelainen, M., Scott, D., Shellard, E. P. S., Sirignano, C., Sirri, G., Spencer, L. D., Sunyaev, R., Suur-Uski, A.-S., Tauber, J. A., Tavagnacco, D., Tenti, M., Toffolatti, L., Tomasi, M., Trombetti, T., Valenziano, L., Valiviita, J., Van Tent, B., Vibert, L., Vielva, P., Villa, F., Vittorio, N., Wandelt, B. D., Wehus, I. K., White, M., White, S. D. M., Zacchei, A., and Zonca, A. (2018). Planck 2018 Results. VI. Cosmological parameters. *arXiv e-prints: 1807.06209*.

Price, S. H., Kriek, M., Shapley, A. E., Reddy, N. A., Freeman, W. R., Coil, A. L., de Groot, L., Shivaei, I., Siana, B., Azadi, M., Barro, G., Mobasher, B., Sanders, R. L., and Zick, T. (2016). The MOSDEF Survey: Dynamical and Baryonic Masses and Kinematic Structures of Star-forming Galaxies at $1.4 \leq z \leq 2.6$. *The Astrophysical Journal*, 819:80–107.

Puech, M., Hammer, F., Lehnert, M. D., and Flores, H. (2007). 3D Spectroscopy with VLT/GIRAFFE. IV. Angular Momentum and Dynamical Support of Intermediate Redshift

Galaxies. *Astronomy & Astrophysics*, 466:83–92.

Rauch, M., Becker, G. D., Haehnelt, M. G., Gauthier, J.-R., Ravindranath, S., and Sargent, W. L. W. (2011). Filamentary Infall of Cold Gas and Escape of Lyα and Hydrogen Ionizing Radiation From an Interacting High-Redshift Galaxy. *Monthly Notices of the Royal Astronomical Society*, 418:1115–1126.

Reiprich, T. H. and Böhringer, H. (2002). The Mass Function of an X-Ray Flux-limited Sample of Galaxy Clusters. *The Astrophysical Journal*, 567:716–740.

Rettura, A., Rosati, P., Nonino, M., Fosbury, R. A. E., Gobat, R., Menci, N., Strazzullo, V., Mei, S., Demarco, R., and Ford, H. C. (2010). Formation Epochs, Star Formation Histories, and Sizes of Massive Early-Type Galaxies in Cluster and Field Environments at z = 1.2: Insights from the Rest-Frame Ultraviolet. *The Astrophysical Journal*, 709:512–524.

Reyes, R., Mandelbaum, R., Gunn, J. E., Pizagno, J., and Lackner, C. N. (2011). Calibrated Tully-Fisher Relations for Improved Estimates of Disc Rotation Velocities. *Monthly Notices of the Royal Astronomical Society*, 417:2347–2386.

Rodriguez-Gomez, V., Sales, L. V., Genel, S., Pillepich, A., Zjupa, J., Nelson, D., Griffen, B., Torrey, P., Snyder, G. F., Vogelsberger, M., Springel, V., Ma, C.-P., and Hernquist, L. (2017). The Role of Mergers and Halo Spin in Shaping Galaxy Morphology. *Monthly Notices of the Royal Astronomical Society*, 467:3083–3098.

Romanowsky, A. J. and Fall, S. M. (2012). Angular Momentum and Galaxy Formation Revisited. *The Astrophysical Journal Supplements*, 203:17–69.

Sales, L. V., Navarro, J. F., Theuns, T., Schaye, J., White, S. D. M., Frenk, C. S., Crain, R. A., and Dalla Vecchia, C. (2012). The Origin of Discs and Spheroids in Simulated Galaxies. *Monthly Notices of the Royal Astronomical Society*, 423:1544–1555.

Sanders, R. L., Shapley, A. E., Kriek, M., Freeman, W. R., Reddy, N. A., Siana, B., Coil, A. L., Mobasher, B., Davé, R., Shivaei, I., Azadi, M., Price, S. H., Leung, G., Fetherolf, T., de Groot, L., Zick, T., Fornasini, F. M., and Barro, G. (2018). The MOSDEF Survey:

A Stellar Mass-SFR-Metallicity Relation Exists at z $\sim$ 2.3. *The Astrophysical Journal*, 858:99–117.

Santos, J. S., Altieri, B., Tanaka, M., Valtchanov, I., Saintonge, A., Dickinson, M., Foucaud, S., Kodama, T., Rawle, T. D., and Tadaki, K. (2014). Star Formation in the Cluster CLG0218.3-0510 at z = 1.62 and Its Large-Scale Environment: The Infrared erspective. *Monthly Notices of the Royal Astronomical Society*, 438:2565–2577.

Shapley, A. E., Reddy, N. A., Kriek, M., Freeman, W. R., Sanders, R. L., Siana, B., Coil, A. L., Mobasher, B., Shivaei, I., Price, S. H., and de Groot, L. (2015). The MOSDEF Survey: Excitation Properties of z $\sim$ 2.3 Star-forming Galaxies. *The Astrophysical Journal*, 801:88–101.

Simons, R. C., Kassin, S. A., Trump, J. R., Weiner, B. J., Heckman, T. M., Barro, G., Koo, D. C., Guo, Y., Pacifici, C., Koekemoer, A., and Stephens, A. W. (2016). Kinematic Downsizing at z $\sim$ 2. *The Astrophysical Journal*, 830:14–34.

Simons, R. C., Kassin, S. A., Weiner, B. J., Faber, S. M., Trump, J. R., Heckman, T. M., Koo, D. C., Pacifici, C., Primack, J. R., Snyder, G. F., and de la Vega, A. (2017). z $\sim$ 2: An Epoch of Disk Assembly. *The Astrophysical Journal*, 843:46–57.

Skelton, R. E., Whitaker, K. E., Momcheva, I. G., Brammer, G. B., van Dokkum, P. G., Labbé, I., Franx, M., van der Wel, A., Bezanson, R., Da Cunha, E., Fumagalli, M., Förster Schreiber, N., Kriek, M., Leja, J., Lundgren, B. F., Magee, D., Marchesini, D., Maseda, M. V., Nelson, E. J., Oesch, P., Pacifici, C., Patel, S. G., Price, S., Rix, H.-W., Tal, T., Wake, D. A., and Wuyts, S. (2014). 3D-HST WFC3-selected Photometric Catalogs in the Five CANDELS/3D-HST Fields: Photometry, Photometric Redshifts, and Stellar Masses. *The Astrophysical Journal Supplements*, 214:24–73.

Spitler, L. R., Labbé, I., Glazebrook, K., Persson, S. E., Monson, A., Papovich, C., Tran, K.-V. H., Poole, G. B., Quadri, R., van Dokkum, P., Kelson, D. D., Kacprzak, G. G., McCarthy, P. J., Murphy, D., Straatman, C. M. S., and Tilvi, V. (2012). First Results from Z-FOURGE: Discovery of a Candidate Cluster at z = 2.2 in COSMOS. *The Astrophysical*

Journal Letters, 748:L21–L27.

Spitler, L. R., Straatman, C. M. S., Labbé, I., Glazebrook, K., Tran, K.-V. H., Kacprzak, G. G., Quadri, R. F., Papovich, C., Persson, S. E., van Dokkum, P., Allen, R., Kawinwanichakij, L., Kelson, D. D., McCarthy, P. J., Mehrtens, N., Monson, A. J., Nanayakkara, T., Rees, G., Tilvi, V., and Tomczak, A. R. (2014). Exploring the z = 3-4 Massive Galaxy Population with ZFOURGE: The Prevalence of Dusty and Quiescent Galaxies. *The Astrophysical Journal Letters*, 787:L36–L42.

Stewart, K. R., Brooks, A. M., Bullock, J. S., Maller, A. H., Diemand, J., Wadsley, J., and Moustakas, L. A. (2013). Angular Momentum Acquisition in Galaxy Halos. *The Astrophysical Journal*, 769:74–86.

Stott, J. P., Swinbank, A. M., Johnson, H. L., Tiley, A., Magdis, G., Bower, R., Bunker, A. J., Bureau, M., Harrison, C. M., Jarvis, M. J., Sharples, R., Smail, I., Sobral, D., Best, P., and Cirasuolo, M. (2016). The KMOS Redshift One Spectroscopic Survey (KROSS): Dynamical Properties, Gas and Dark Matter Fractions of Typical z $\sim$ 1 Star-forming Galaxies. *Monthly Notices of the Royal Astronomical Society*, 457:1888–1904.

Straatman, C. M. S., Glazebrook, K., Kacprzak, G. G., Labbé, I., Nanayakkara, T., Alcorn, L., Cowley, M., Kewley, L. J., Spitler, L. R., Tran, K.-V. H., and Yuan, T. (2017). ZFIRE: The Evolution of the Stellar Mass Tully-Fisher Relation to Redshift $\sim$2.2. *The Astrophysical Journal*, 839:57–77.

Straatman, C. M. S., Labbé, I., Spitler, L. R., Allen, R., Altieri, B., Brammer, G. B., Dickinson, M., van Dokkum, P., Inami, H., Glazebrook, K., Kacprzak, G. G., Kawinwanichakij, L., Kelson, D. D., McCarthy, P. J., Mehrtens, N., Monson, A., Murphy, D., Papovich, C., Persson, S. E., Quadri, R., Rees, G., Tomczak, A., Tran, K.-V. H., and Tilvi, V. (2014). A Substantial Population of Massive Quiescent Galaxies at z $\sim$ 4 from ZFOURGE. *The Astrophysical Journal Letters*, 783:L14–L21.

Straatman, C. M. S., Labbé, I., Spitler, L. R., Glazebrook, K., Tomczak, A., Allen, R., Brammer, G. B., Cowley, M., van Dokkum, P., Kacprzak, G. G., Kawinwanichakij, L., Mehrtens, N., Nanayakkara, T., Papovich, C., Persson, S. E., Quadri, R. F., Rees, G., Tilvi, V., Tran, K.-V. H., and Whitaker, K. E. (2015). The Sizes of Massive Quiescent and Star-forming Galaxies at z $\sim$ 4 with ZFOURGE and CANDELS. *The Astrophysical Journal Letters*, 808:L29–L37.

Straatman, C. M. S., Spitler, L. R., Quadri, R. F., Labbé, I., Glazebrook, K., Persson, S. E., Papovich, C., Tran, K.-V. H., Brammer, G. B., Cowley, M., Tomczak, A., Nanayakkara, T., Alcorn, L., Allen, R., Broussard, A., van Dokkum, P., Forrest, B., van Houdt, J., Kacprzak, G. G., Kawinwanichakij, L., Kelson, D. D., Lee, J., McCarthy, P. J., Mehrtens, N., Monson, A., Murphy, D., Rees, G., Tilvi, V., and Whitaker, K. E. (2016). The FourStar Galaxy Evolution Survey (ZFOURGE): Ultraviolet to Far-infrared Catalogs, Medium-bandwidth Photometric Redshifts with Improved Accuracy, Stellar Masses, and Confirmation of Quiescent Galaxies to z $\sim$ 3.5. *The Astrophysical Journal*, 830:51–85.

Swinbank, A. M., Smail, I., Sobral, D., Theuns, T., Best, P. N., and Geach, J. E. (2012). The Properties of the Star-forming Interstellar Medium at z = 0.8-2.2 from HiZELS: Star Formation and Clump Scaling Laws in Gas-rich, Turbulent Disks. *The Astrophysical Journal*, 760:130–140.

Tacconi, L. J., Genzel, R., Neri, R., Cox, P., Cooper, M. C., Shapiro, K., Bolatto, A., Bouché, N., Bournaud, F., Burkert, A., Combes, F., Comerford, J., Davis, M., Schreiber, N. M. F., Garcia-Burillo, S., Gracia-Carpio, J., Lutz, D., Naab, T., Omont, A., Shapley, A., Sternberg, A., and Weiner, B. (2010). High Molecular Gas Fractions in Normal Massive Star-Forming Galaxies in the Young Universe. *Nature*, 463:781–784.

Tacconi, L. J., Neri, R., Genzel, R., Combes, F., Bolatto, A., Cooper, M. C., Wuyts, S., Bournaud, F., Burkert, A., Comerford, J., Cox, P., Davis, M., Förster Schreiber, N. M., García-Burillo, S., Gracia-Carpio, J., Lutz, D., Naab, T., Newman, S., Omont, A., Saintonge, A., Shapiro Griffin, K., Shapley, A., Sternberg, A., and Weiner, B. (2013). Phibss: Molecular Gas Content and Scaling Relations in z $\sim$ 1-3 Massive, Main-sequence Star-forming Galaxies. *The Astrophysical Journal*, 768:74–96.

Tanaka, M., Finoguenov, A., and Ueda, Y. (2010). A Spectroscopically Confirmed X-ray Cluster at z = 1.62 with a Possible Companion in the Subaru/XMM-Newton Deep Field. *The Astrophysical Journal Letters*, 716:L152–L156.

Tomczak, A. R., Quadri, R. F., Tran, K.-V. H., Labbé, I., Straatman, C. M. S., Papovich, C., Glazebrook, K., Allen, R., Brammer, G. B., Cowley, M., Dickinson, M., Elbaz, D., Inami, H., Kacprzak, G. G., Morrison, G. E., Nanayakkara, T., Persson, S. E., Rees, G. A., Salmon, B., Schreiber, C., Spitler, L. R., and Whitaker, K. E. (2016). The SFR-M* Relation and Empirical Star-Formation Histories from ZFOURGE* at $0.5 < z < 4$. *The Astrophysical Journal*, 817:118–134.

Tomczak, A. R., Quadri, R. F., Tran, K.-V. H., Labbé, I., Straatman, C. M. S., Papovich, C., Glazebrook, K., Allen, R., Brammer, G. B., Kacprzak, G. G., Kawinwanichakij, L., Kelson, D. D., McCarthy, P. J., Mehrtens, N., Monson, A. J., Persson, S. E., Spitler, L. R., Tilvi, V., and van Dokkum, P. (2014). Galaxy Stellar Mass Functions from ZFOURGE/CANDELS: An Excess of Low-mass Galaxies since z = 2 and the Rapid Buildup of Quiescent Galaxies. *The Astrophysical Journal*, 783:85–100.

Torrey, P., Vogelsberger, M., Hernquist, L., McKinnon, R., Marinacci, F., Simcoe, R. A., Springel, V., Pillepich, A., Naiman, J., Pakmor, R., Weinberger, R., Nelson, D., and Genel, S. (2018). Similar Star Formation Rate and Metallicity Variability Time-Scales Drive the Fundamental Metallicity Relation. *Monthly Notices of the Royal Astronomical Society*, 477:L16–L20.

Tran, K.-V. H., Alcorn, L. Y., Kacprzak, G. G., Nanayakkara, T., Straatman, C., Yuan, T., Cowley, M., Davé, R., Glazebrook, K., Kewley, L. J., Labbé, I., Martizzi, D., Papovich, C., Quadri, R., Spitler, L. R., and Tomczak, A. (2017). ZFIRE: Similar Stellar Growth in Hα-emitting Cluster and Field Galaxies at $z \sim 2$. *The Astrophysical Journal*, 834:101–115.

Tran, K.-V. H., Nanayakkara, T., Yuan, T., Kacprzak, G. G., Glazebrook, K., Kewley, L. J., Momcheva, I., Papovich, C. J., Quadri, R., Rudnick, G., Saintonge, A., Spitler, L. R., Straatman, C., and Tomczak, A. (2015). ZFIRE: Galaxy Cluster Kinematics, Hα Star Formation Rates, and Gas Phase Metallicities of XMM-LSS J02182-05102 at zcl = 1.6232. *The Astrophysical Journal*, 811:28–44.

Tran, K.-V. H., Papovich, C., Saintonge, A., Brodwin, M., Dunlop, J. S., Farrah, D., Finkelstein, K. D., Finkelstein, S. L., Lotz, J., McLure, R. J., Momcheva, I., and Willmer, C. N. A. (2010). Reversal of Fortune: Confirmation of an Increasing Star Formation-Density Relation in a Cluster at z = 1.62. *The Astrophysical Journal Letters*, 719:L126–L129.

Tran, K.-V. H., Simard, L., Illingworth, G., and Franx, M. (2003). Cl 1358+62: Characterizing the Physical Properties of Cluster Galaxies at z = 0.33. *The Astrophysical Journal*, 590:238–255.

Tully, R. B. and Fisher, J. R. (1977). A New Method of Determining Distances to Galaxies. *Astronomy & Astrophysics*, 54:661–673.

Turner, O. J., Harrison, C. M., Cirasuolo, M., McLure, R. J., Dunlop, J., Swinbank, A. M., and Tiley, A. L. (2017). The KMOS Deep Survey (KDS) II: The Evolution of the Stellar-Mass Tully-Fisher Relation Since z $\sim$ 4. *arXiv e-prints: 1711.03604*.

van de Voort, F., Bahé, Y. M., Bower, R. G., Correa, C. A., Crain, R. A., Schaye, J., and Theuns, T. (2017). The Environmental Dependence of Gas Accretion on to Galaxies: Quenching Satellites Through Starvation. *Monthly Notices of the Royal Astronomical Society*, 466:3460–3471.

van der Wel, A., Bell, E. F., Häussler, B., McGrath, E. J., Chang, Y.-Y., Guo, Y., McIntosh, D. H., Rix, H.-W., Barden, M., Cheung, E., Faber, S. M., Ferguson, H. C., Galametz, A., Grogin, N. A., Hartley, W., Kartaltepe, J. S., Kocevski, D. D., Koekemoer, A. M., Lotz, J., Mozena, M., Peth, M. A., and Peng, C. Y. (2012). Structural Parameters of Galaxies in CANDELS. *The Astrophysical Journal Supplements*, 203:24–36.

van der Wel, A., Franx, M., van Dokkum, P. G., Skelton, R. E., Momcheva, I. G., Whitaker, K. E., Brammer, G. B., Bell, E. F., Rix, H.-W., Wuyts, S., Ferguson, H. C., Holden,

B. P., Barro, G., Koekemoer, A. M., Chang, Y.-Y., McGrath, E. J., Häussler, B., Dekel, A., Behroozi, P., Fumagalli, M., Leja, J., Lundgren, B. F., Maseda, M. V., Nelson, E. J., Wake, D. A., Patel, S. G., Labbé, I., Faber, S. M., Grogin, N. A., and Kocevski, D. D. (2014). 3D-HST+CANDELS: The Evolution of the Galaxy Size-Mass Distribution since z = 3. *The Astrophysical Journal*, 788:28–47.

Vitvitska, M., Klypin, A. A., Kravtsov, A. V., Wechsler, R. H., Primack, J. R., and Bullock, J. S. (2002). The Origin of Angular Momentum in Dark Matter Halos. *The Astrophysical Journal*, 581:799–809.

Weiner, B. J., Willmer, C. N. A., Faber, S. M., Harker, J., Kassin, S. A., Phillips, A. C., Melbourne, J., Metevier, A. J., Vogt, N. P., and Koo, D. C. (2006). A Survey of Galaxy Kinematics to z$\sim$1 in the TKRS/GOODS-N Field. II. Evolution in the Tully-Fisher Relation. *The Astrophysical Journal*, 653:1049–1069.

Wellons, S., Torrey, P., Ma, C.-P., Rodriguez-Gomez, V., Pillepich, A., Nelson, D., Genel, S., Vogelsberger, M., and Hernquist, L. (2016). The Diverse Evolutionary Paths of Simulated High-z Massive, Compact Galaxies to z = 0. *Monthly Notices of the Royal Astronomical Society*, 456:1030–1048.

White, S. D. M. (1984). Angular Momentum Growth in Protogalaxies. *The Astrophysical Journal*, 286:38–41.

White, S. D. M. and Rees, M. J. (1978). Core Condensation in Heavy Halos - A Two-Stage Theory for Galaxy Formation and Clustering. *Monthly Notices of the Royal Astronomical Society*, 183:341–358.

Williams, R. J., Quadri, R. F., Franx, M., van Dokkum, P., and Labbé, I. (2009). Detection of Quiescent Galaxies in a Bicolor Sequence from Z = 0-2. *The Astrophysical Journal*, 691:1879–1895.

Wisnioski, E., Förster Schreiber, N. M., Wuyts, S., Wuyts, E., Bandara, K., Wilman, D., Genzel, R., Bender, R., Davies, R., Fossati, M., Lang, P., Mendel, J. T., Beifiori, A., Brammer, G., Chan, J., Fabricius, M., Fudamoto, Y., Kulkarni, S., Kurk, J., Lutz, D., Nelson, E. J., Momcheva, I., Rosario, D., Saglia, R., Seitz, S., Tacconi, L. J., and van Dokkum, P. G. (2015). The KMOS^{3D} Survey: Design, First Results, and the Evolution of Galaxy Kinematics from 0.7 <= z <= 2.7. *The Astrophysical Journal*, 799:209–236.

Yuan, T., Nanayakkara, T., Kacprzak, G. G., Tran, K.-V. H., Glazebrook, K., Kewley, L. J., Spitler, L. R., Poole, G. B., Labbé, I., Straatman, C. M. S., and Tomczak, A. R. (2014). Keck/MOSFIRE Spectroscopic Confirmation of a Virgo-like Cluster Ancestor at z = 2.095. *The Astrophysical Journal Letters*, 795:L20–L26.

APPENDIX A

HELA MODELING

Here we describe our method of fitting our emission lines, using HELA (Heidelberg Emission Line Algorithm), provided by its developer, C.M. Straatman, which uses the prescription of Price et al. (2016).

The emission line fit is generated from a 3D data-cube. This data cube is generated given an input inclination, slit offset, redshift, emission line wavelength, and an estimated scale radius, turnover radius, asymptotic velocity, and σ_g. Given bounds in spatial and wavelength space (x_{init} and y_{init}), we create an x-y grid of velocity space, face-on with a galaxy, or at $i = 0^o$. With our input $\Delta\alpha$, we transform our model using

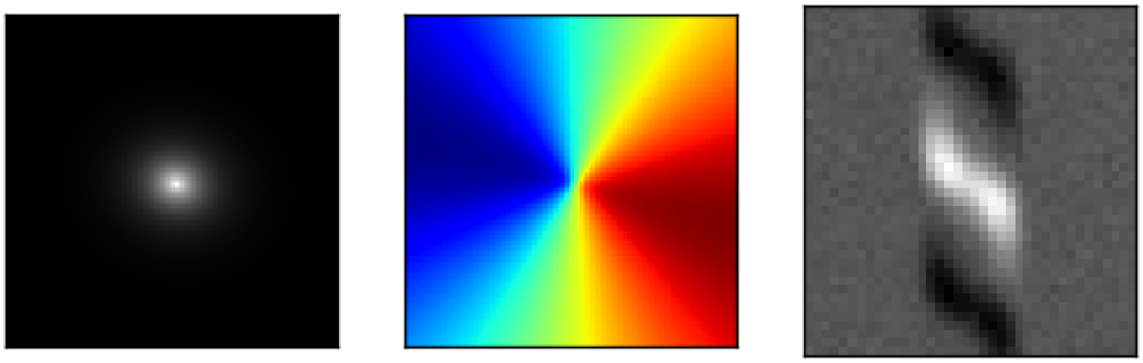

Figure A.1: An example of our models created in HELA. Left: Spatial intensity profile of an infinitely thin disk galaxy, with $V_t = 300$ km s^{-1}, $r_s = 0.5''$, $r_t = 0.15''$, σ_g= 25 km s^{-1}, $i = 30^o$, and $\Delta\alpha = 15^o$. Center: The line of sight velocity field of the galaxy to the left. Right: Emission line of the galaxy described, convolved with a 2D Moffat profile at 0.7$''$ seeing. Reproduced by permission of the AAS.

Reprinted with permission from "ZFIRE: 3D Modeling of Rotation, Dispersion, and Angular Momentum of Star-Forming Galaxies at $z \sim 2$" by Alcorn, L., et al., 2018, *The Astrophysical Journal*, Volume 858, Article 47, Copyright 2018 American Astronomical Society.

$$x_0 = x_{init} \cos \Delta\alpha - y_{init} \sin \Delta\alpha \tag{A.1}$$

$$y_0 = x_{init} \sin \Delta\alpha + y_{init} \cos \Delta\alpha, \tag{A.2}$$

to account for our offset between the galaxy major axis and our slit PA. We transform our values using our input inclination with

$$x_i = x_p / \cos i, \tag{A.3}$$

rotating our galaxy into its correct inclination. We define a variable r, the distance from the center of the galaxy, as,

$$r^2 = \sqrt{x_i^2 + y_0^2}, \tag{A.4}$$

and the angle ψ as,

$$\cos \psi = y_p / r. \tag{A.5}$$

An example of the disk is seen in Figure A.1, left panel.

A velocity profile is created assuming an infinitely thin disk, an arctangent rotation curve

$$V_{rot}(r) = \frac{2}{\pi} V_t \, arctan \frac{r}{r_t}, \tag{A.6}$$

where V_t is the asymptotic velocity and r_t is the turnover radius. This equation is then used to determine the line-of-sight velocity (V_{LOS})

$$V_{LOS} = V_{rot}(r) \sin i \cos \psi. \tag{A.7}$$

The resultant line-of-sight velocity map is seen in Figure A.1, middle panel.

To map our kinematic components into a 2D emission-line observation, as would be seen from slit spectroscopy, we create a spatial exponential intensity profile,

$$I(r) = I_0 \exp \frac{-(r)}{r_s}, \tag{A.8}$$

where r_s is the intensity scale radius. The intensity profile is then mapped onto V_{LOS} using

$$I(r, \lambda) = \frac{I(r)}{\sqrt{2\pi}\sigma_g} \exp(-\frac{(\lambda - \lambda_{LOS})^2}{2\sigma_g^2}), \tag{A.9}$$

where σ_g is the intrinsic gas velocity dispersion.

We convolve this intensity profile with a Moffat 2D PSF if Moffat parameters α and β are provided, as in the Moffat PSF profile:

$$PSF(r) = \frac{\beta - 1}{\pi\alpha^2} \left[1 + \left(\frac{r}{\alpha}\right)^2\right]^{-\beta}. \tag{A.10}$$

If Moffat parameters are not provided, then a Gaussian profile of given seeing can be used in place of a Moffat profile. Then we collapse the model over a slit width of $0.7''$, and scale to our preferred intensity signal (see Figure A.1, right panel, for an example of the collapsed emission line). During fitting to MOSFIRE data or simulated observations, this scaling is determined from a weighted least-squares fit of the model to the data or simulation, weighted by the measurement errors from the weight images.

Our best-fit models for our sample can be seen in Figure A.2.

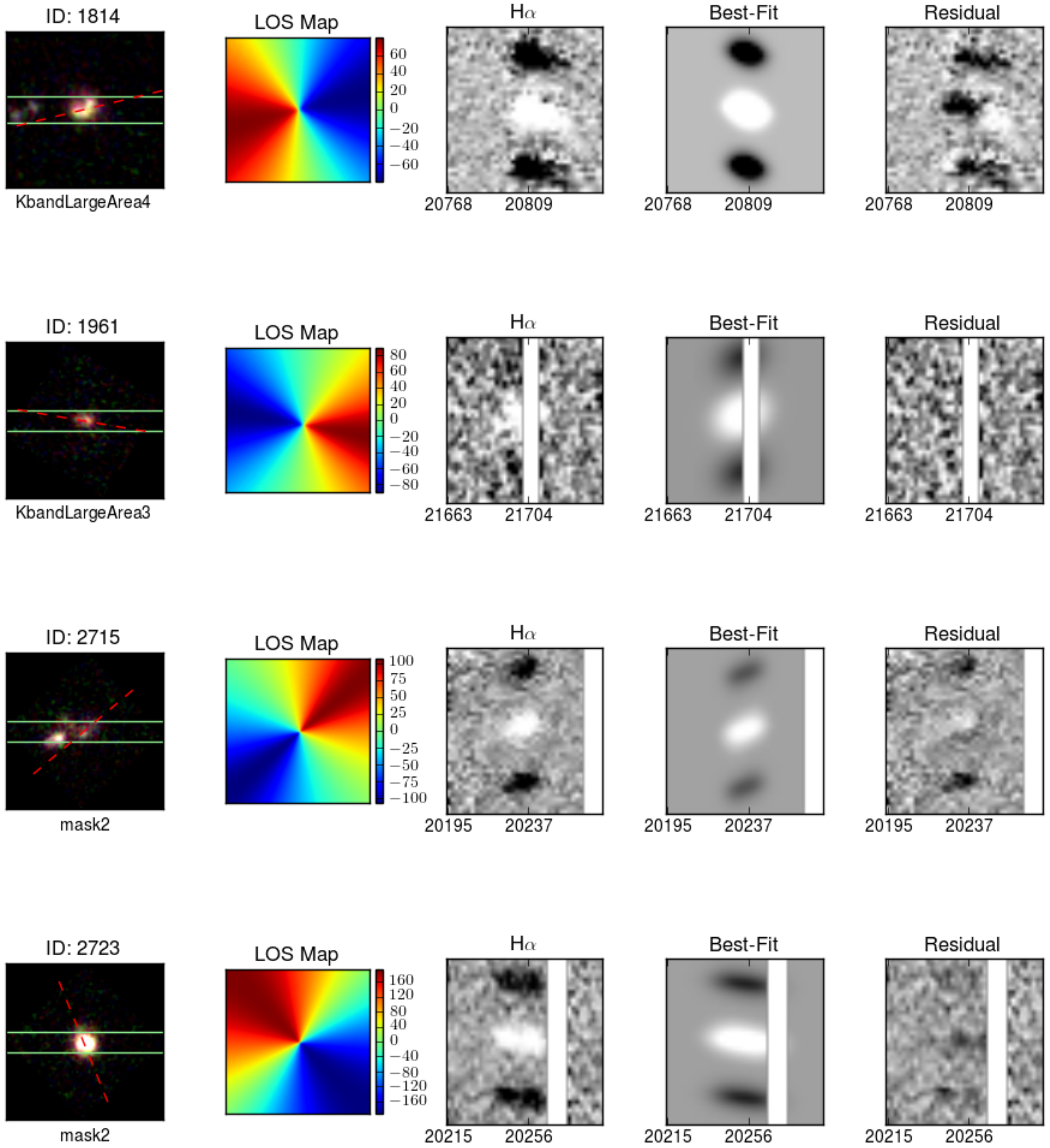

Figure A.2: Imaging and best fits of galaxies in our sample. From Left: RGB images are from F160W (red), F140W (green), and F125W (blue). The slit overlay is shown in green and the major axis of the galaxy is shown in red. Second from left: The LOS map is aligned with the RGB image. Center: The Hα emission line with sky emission masked in white and continuum removed, if present. Second from right: Best-fit emission line from HELA modeling, characterized by the LOS map. Right: Residual from the best-fit line. Reproduced by permission of the AAS.

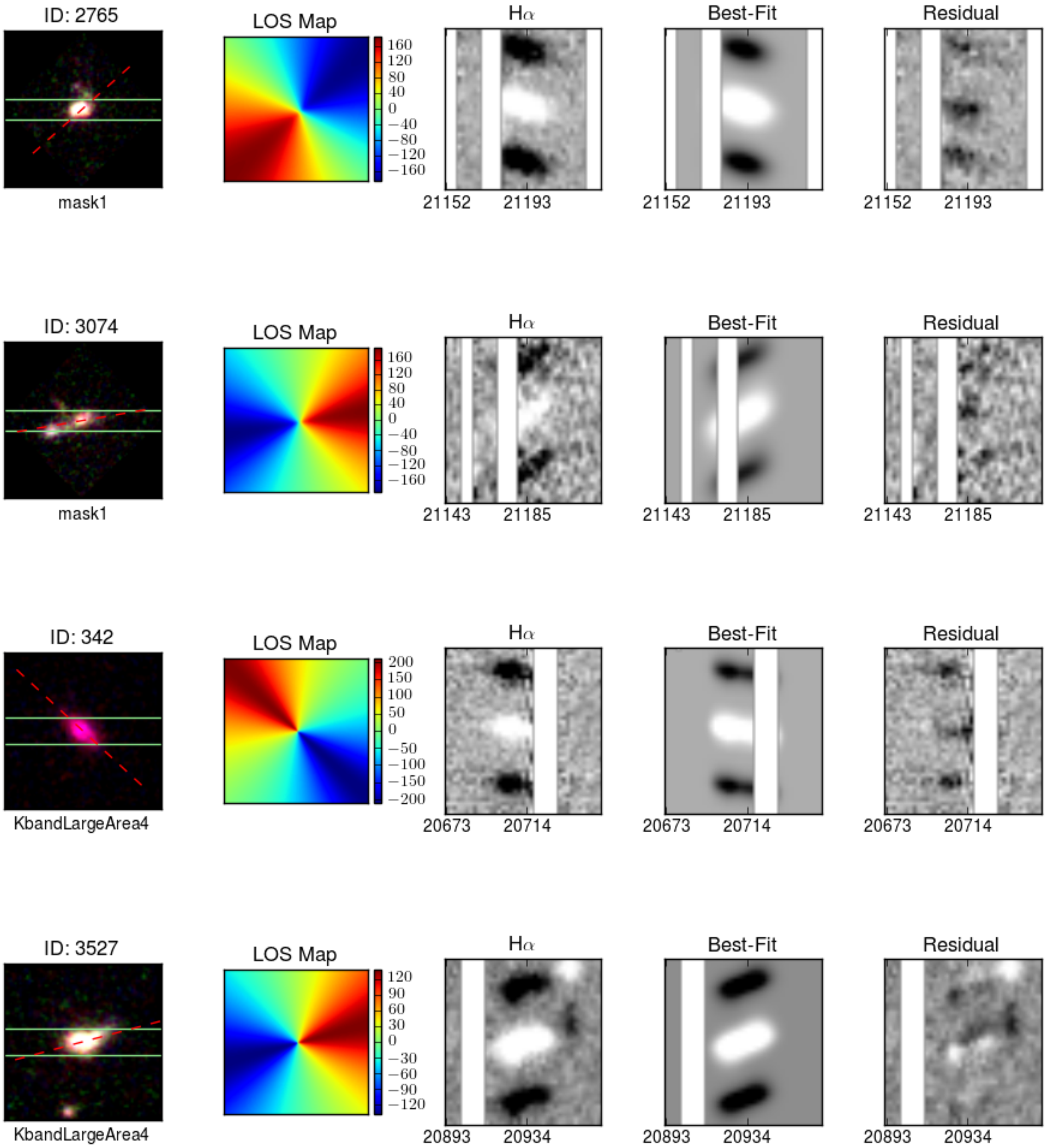

Figure A.2 Continued. Reproduced by permission of the AAS.

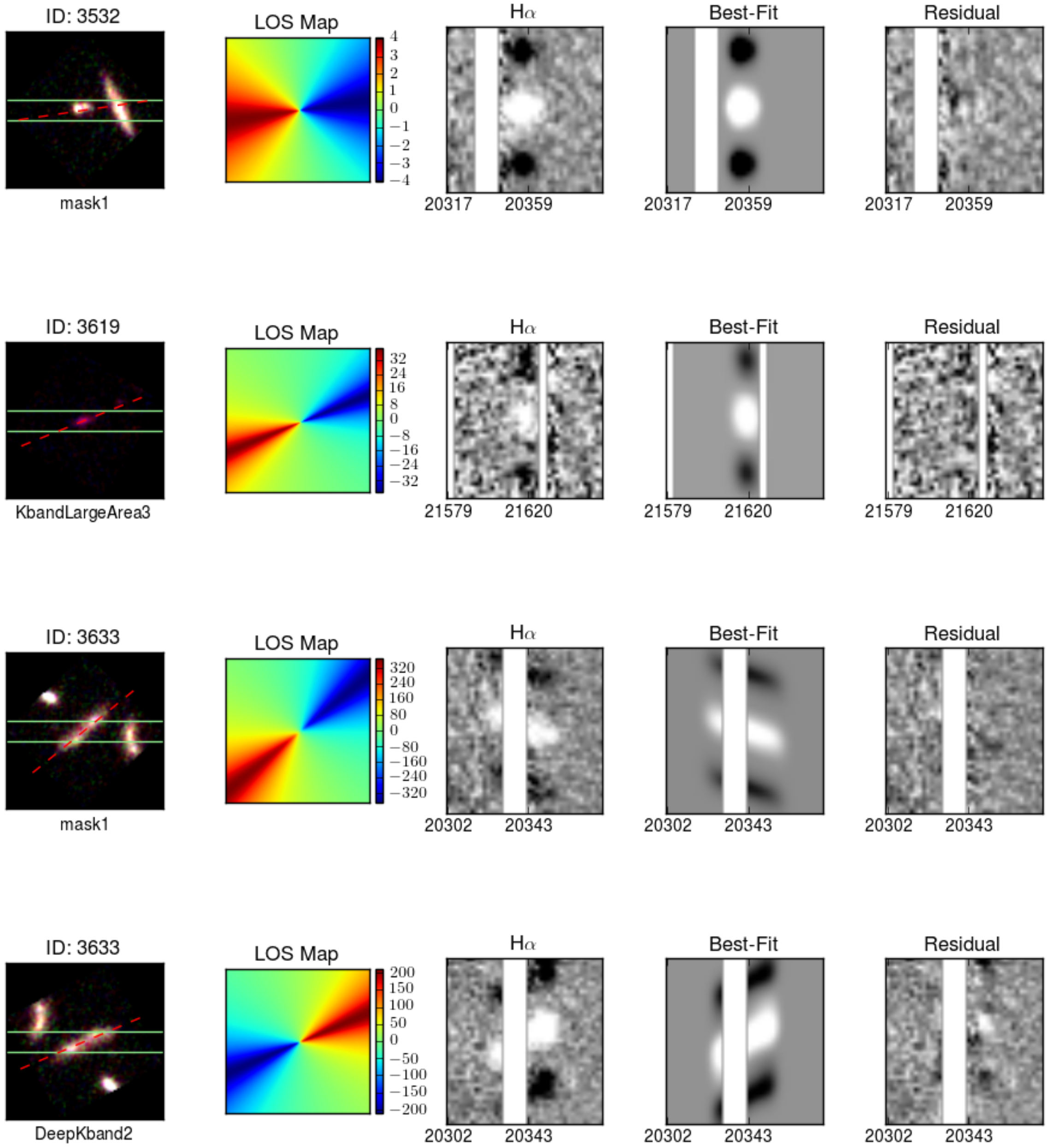

Figure A.2 Continued. Reproduced by permission of the AAS.

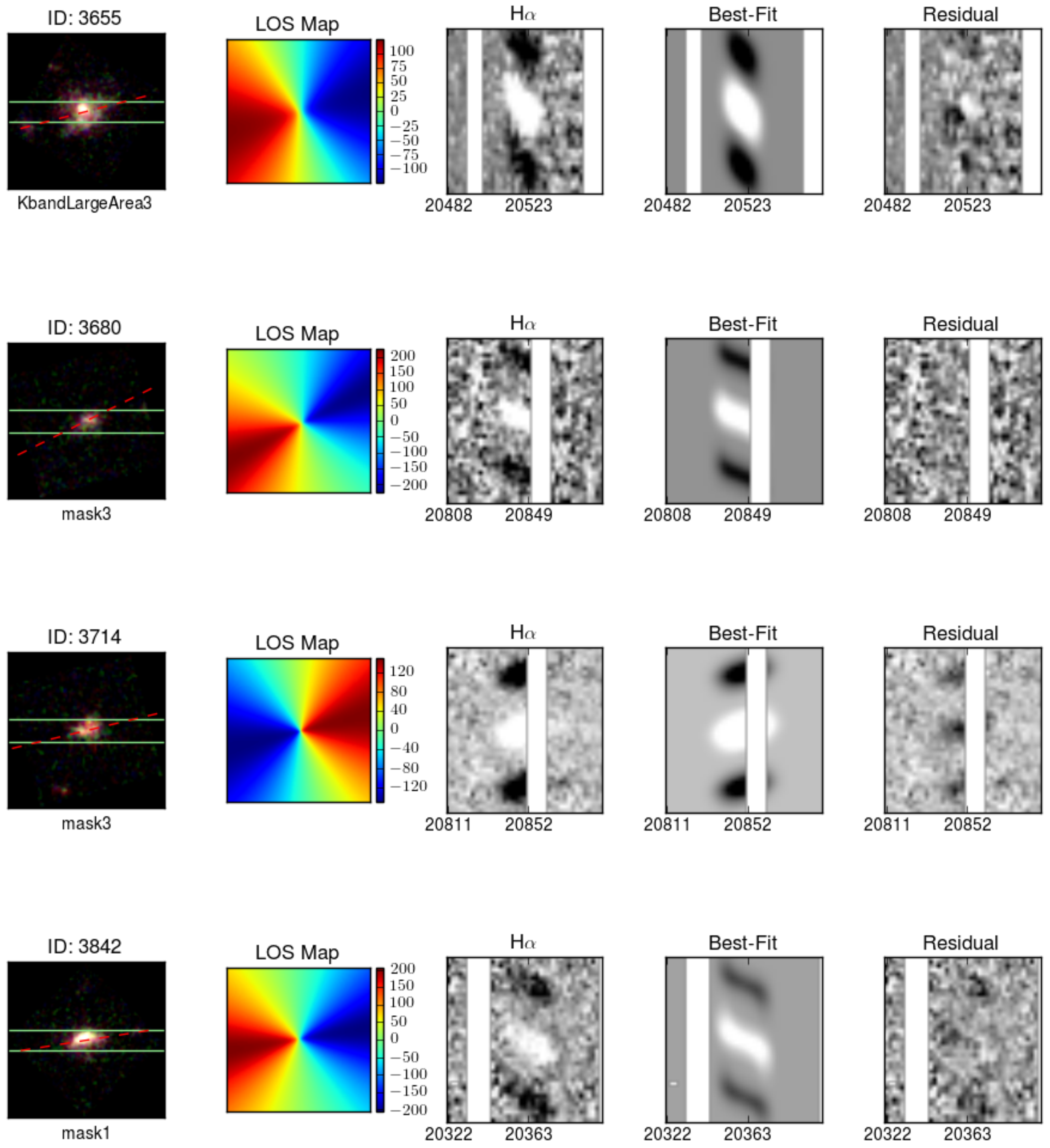

Figure A.2 Continued. Reproduced by permission of the AAS.

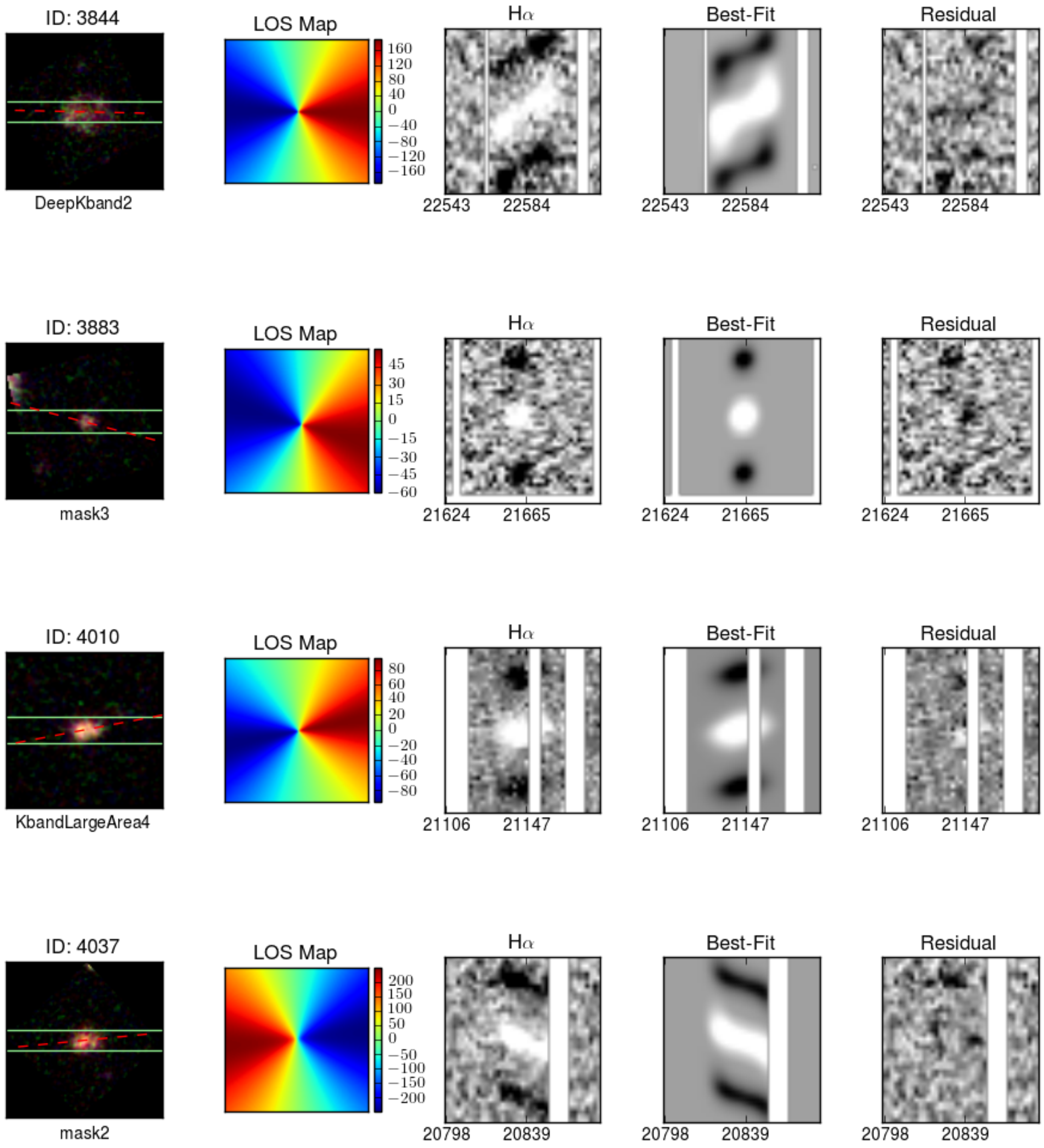

Figure A.2 Continued. Reproduced by permission of the AAS.

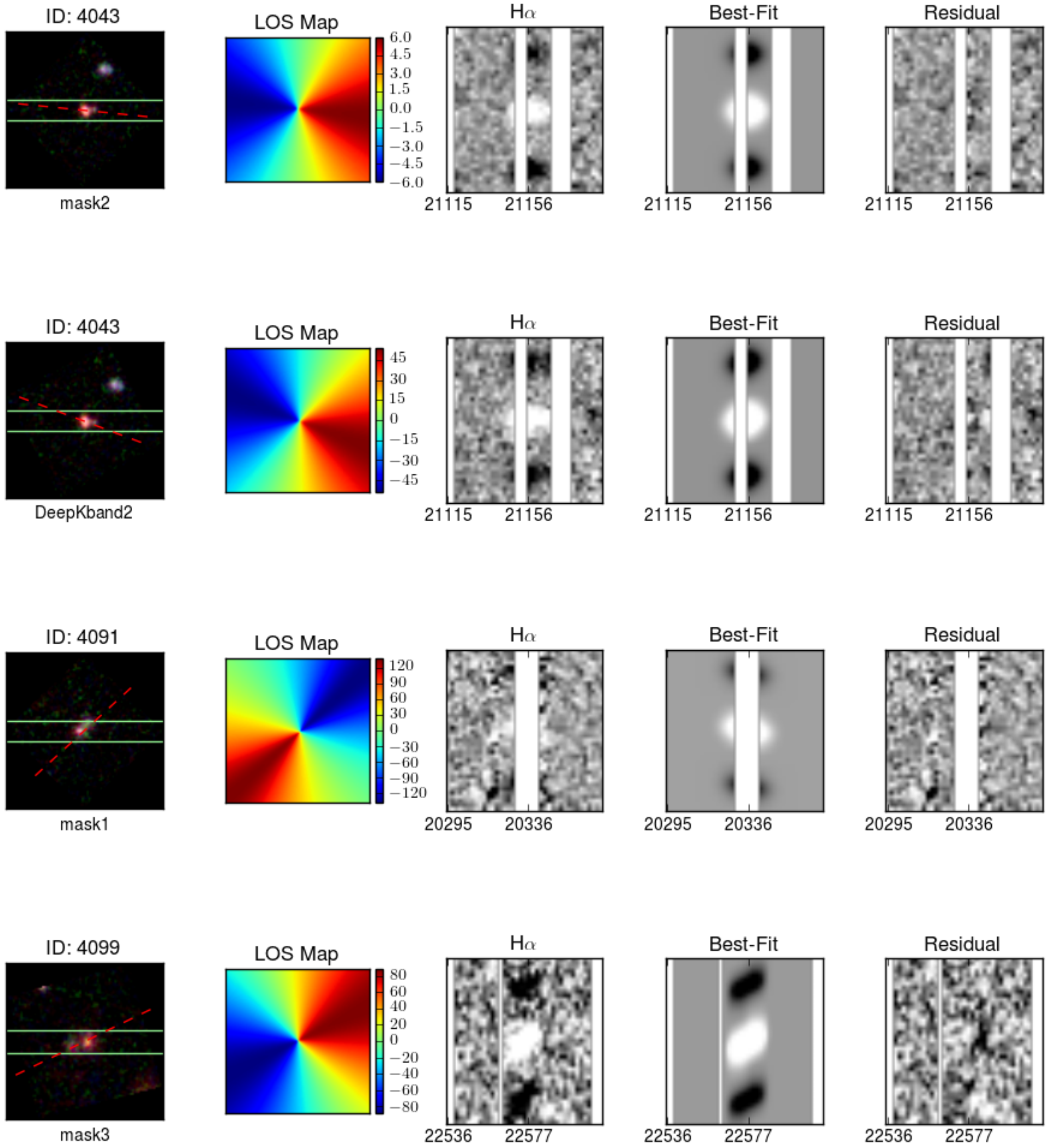

Figure A.2 Continued. Reproduced by permission of the AAS.

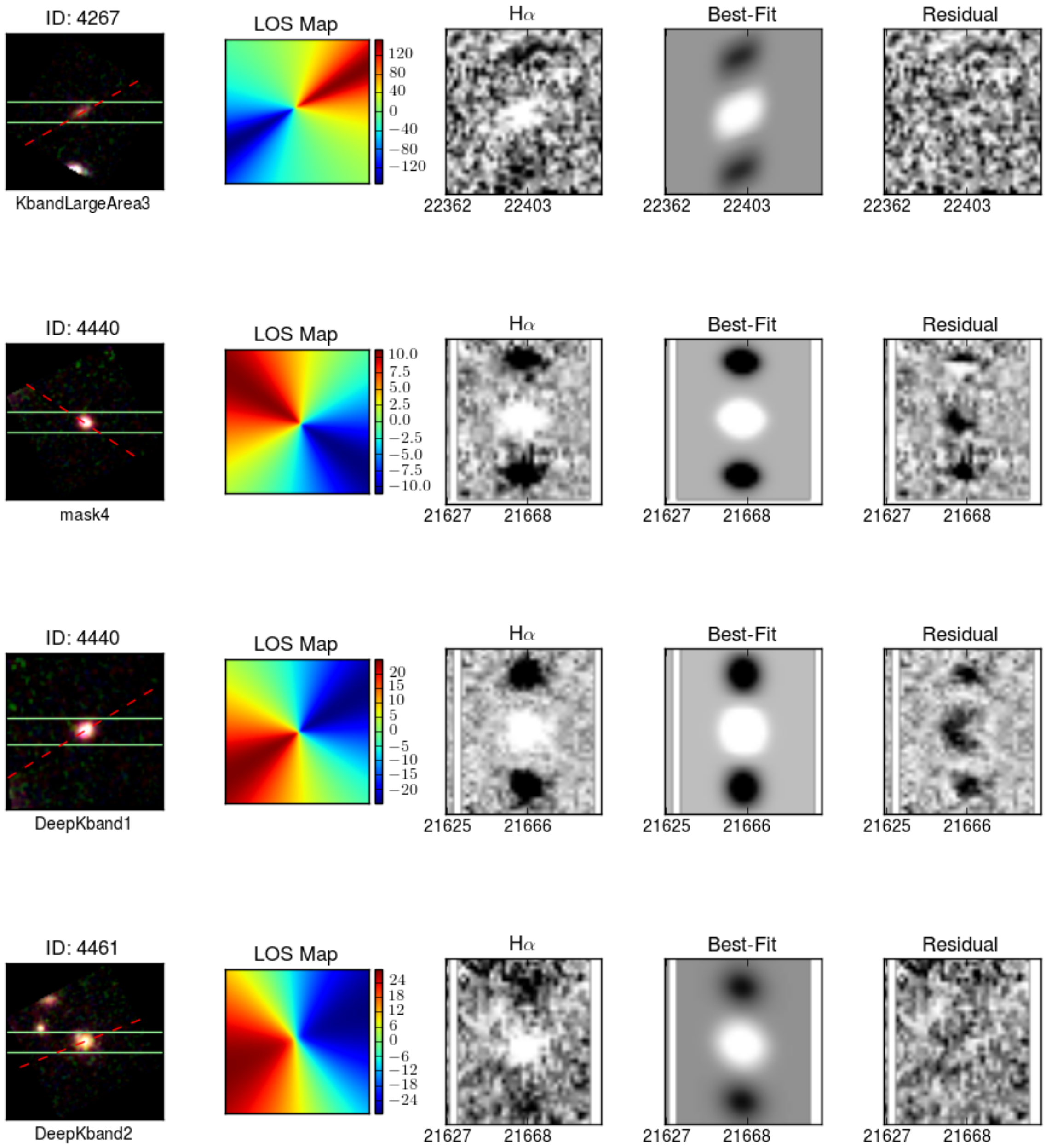

Figure A.2 Continued. Reproduced by permission of the AAS.

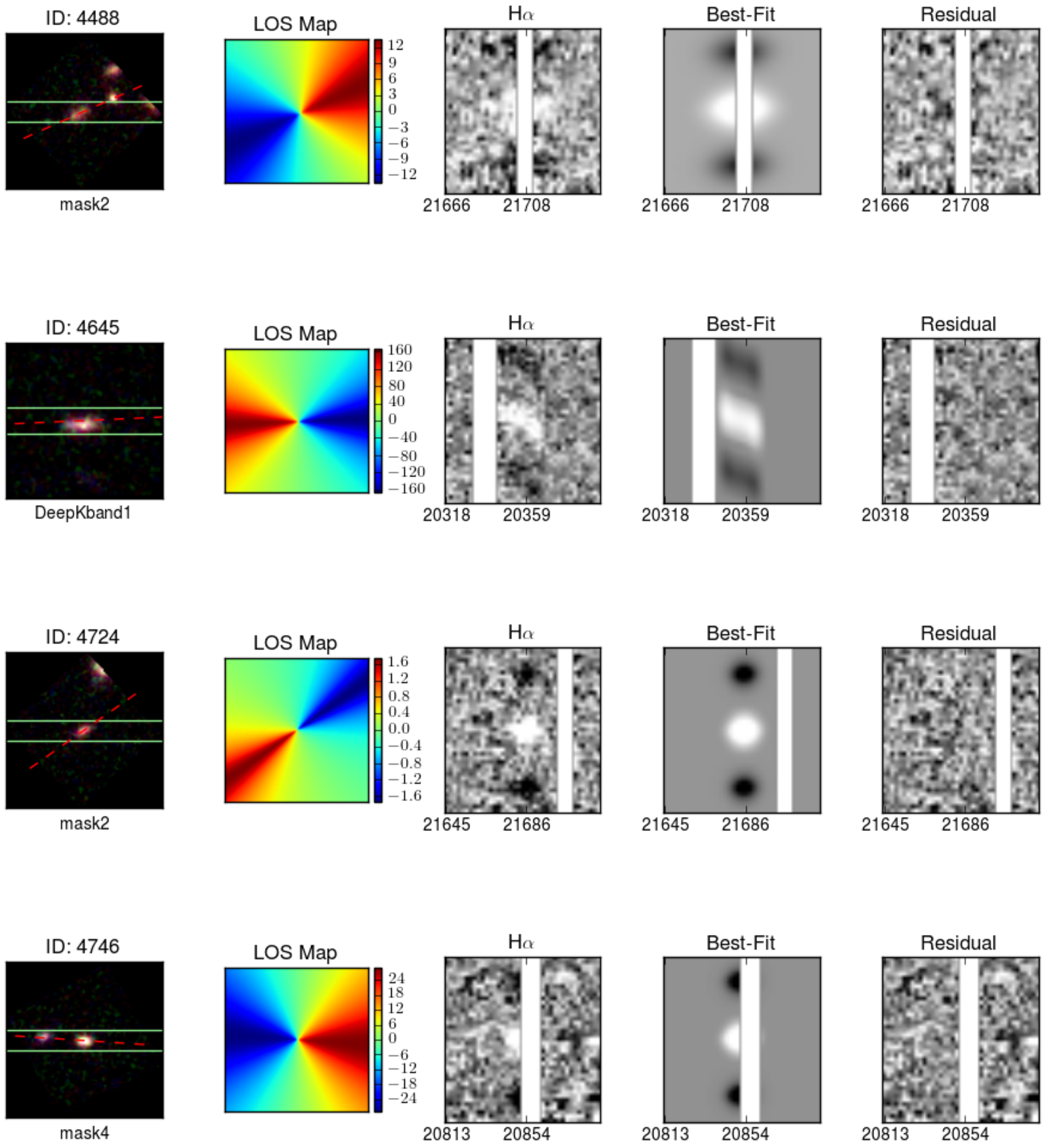

Figure A.2 Continued. Reproduced by permission of the AAS.

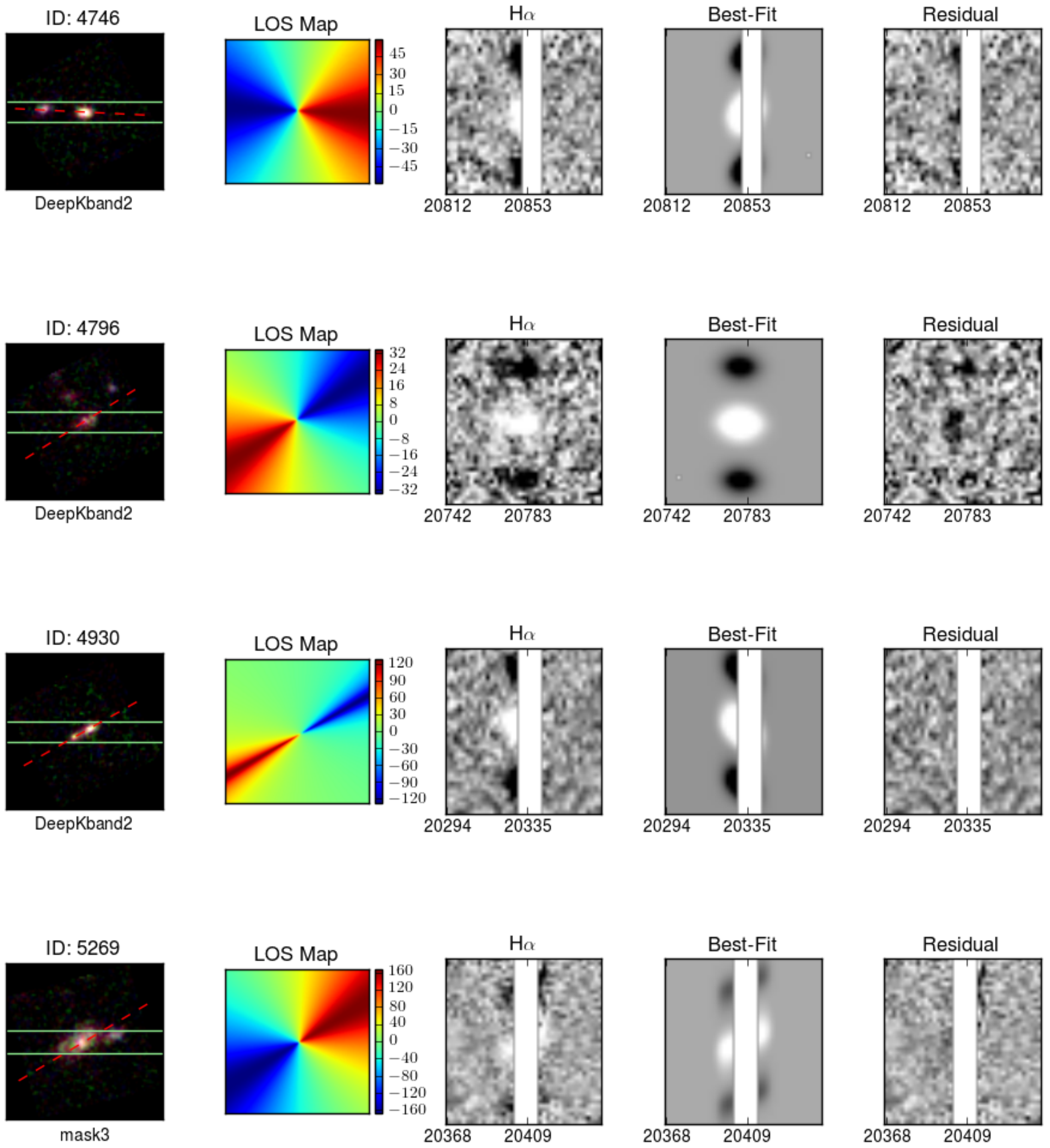

Figure A.2 Continued. Reproduced by permission of the AAS.

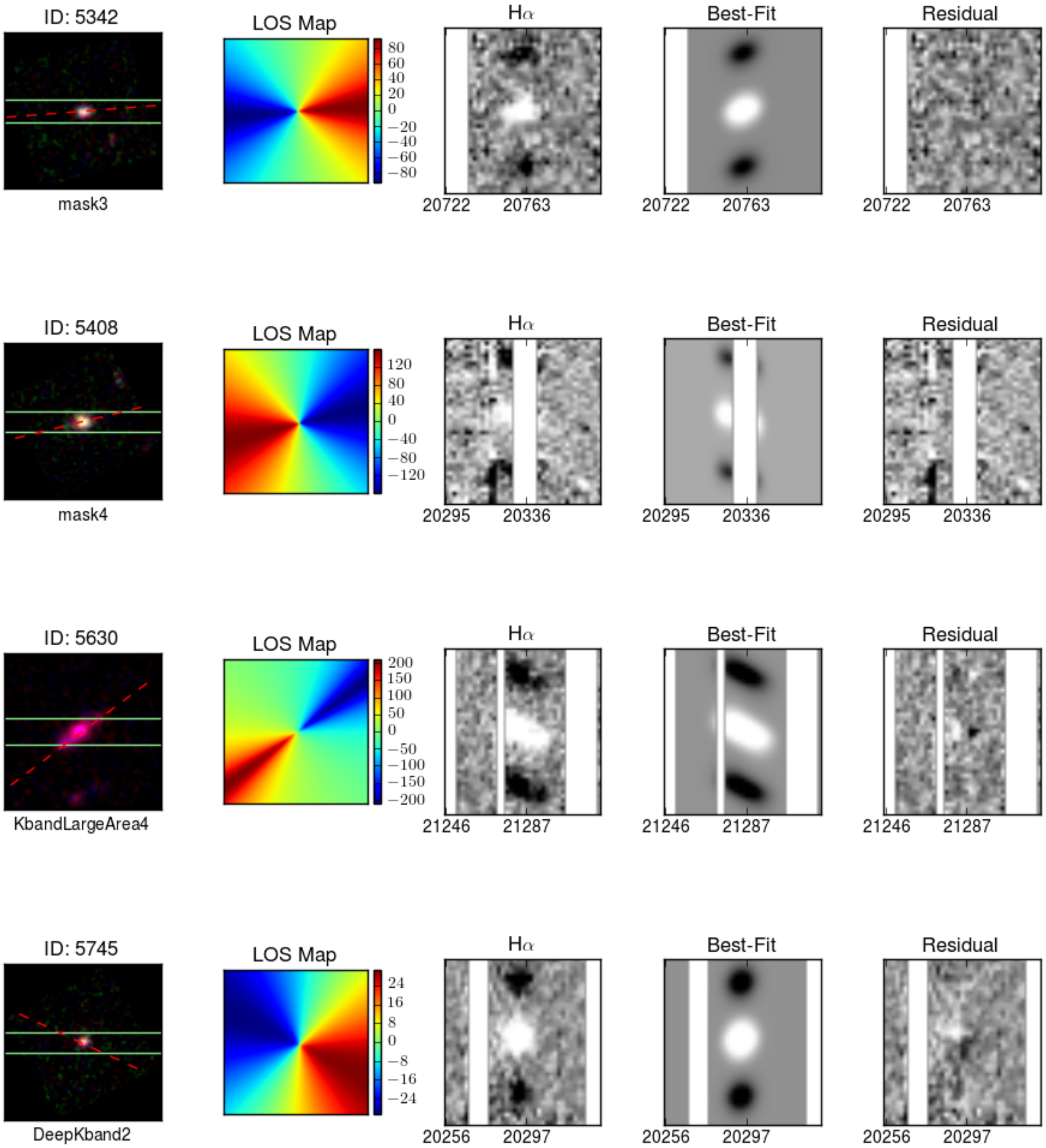

Figure A.2 Continued. Reproduced by permission of the AAS.

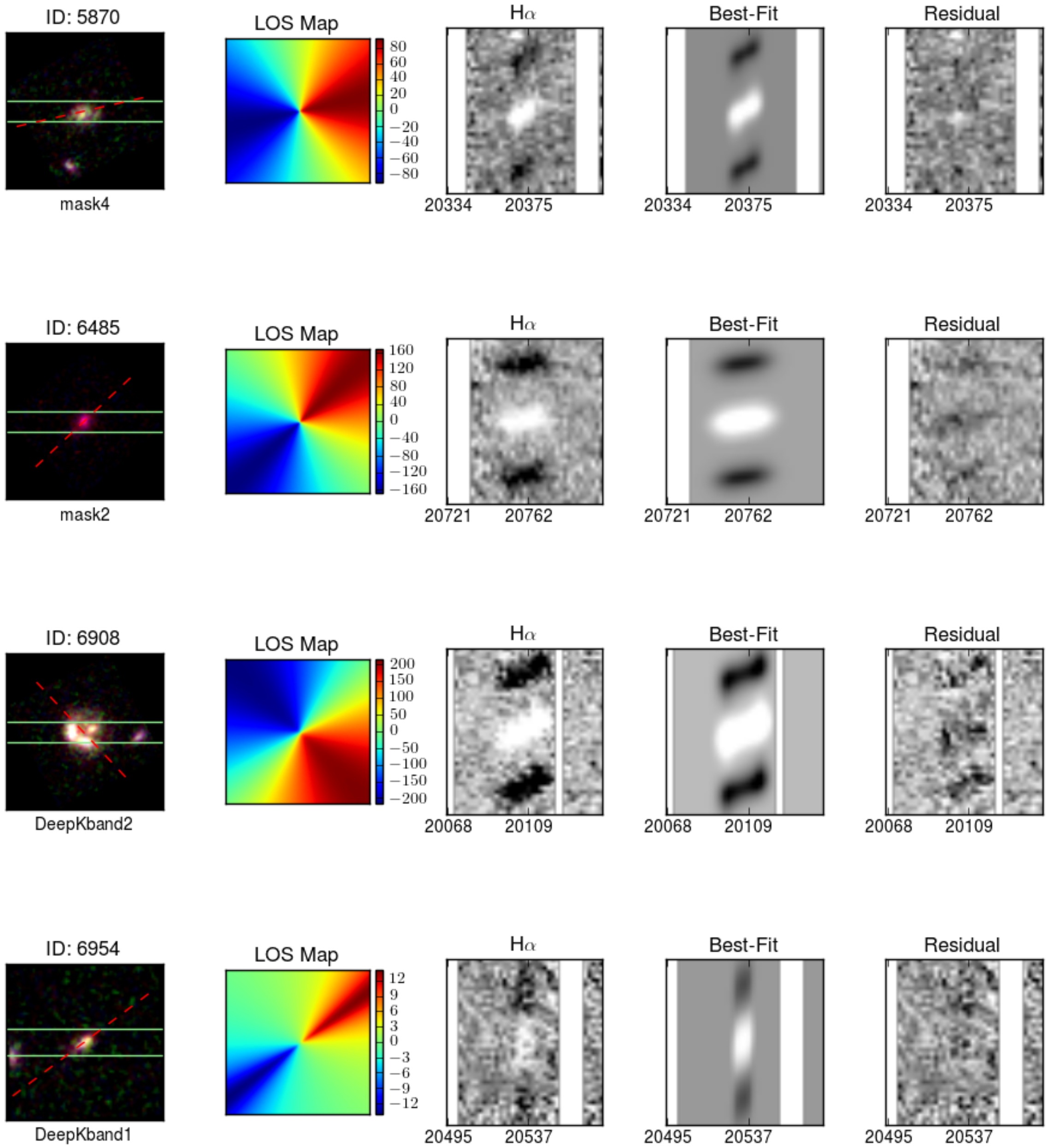

Figure A.2 Continued. Reproduced by permission of the AAS.

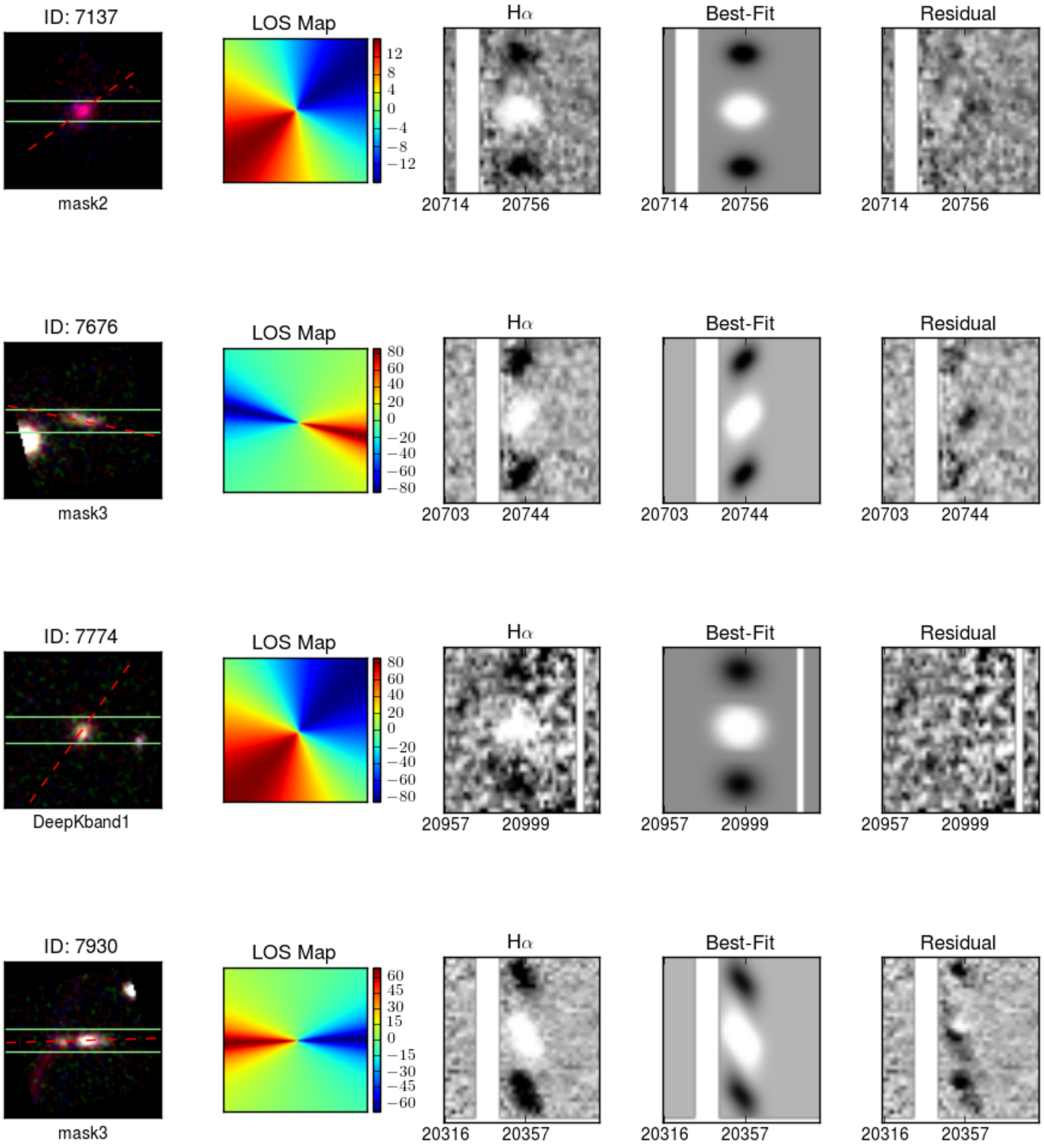

Figure A.2 Continued. Reproduced by permission of the AAS.

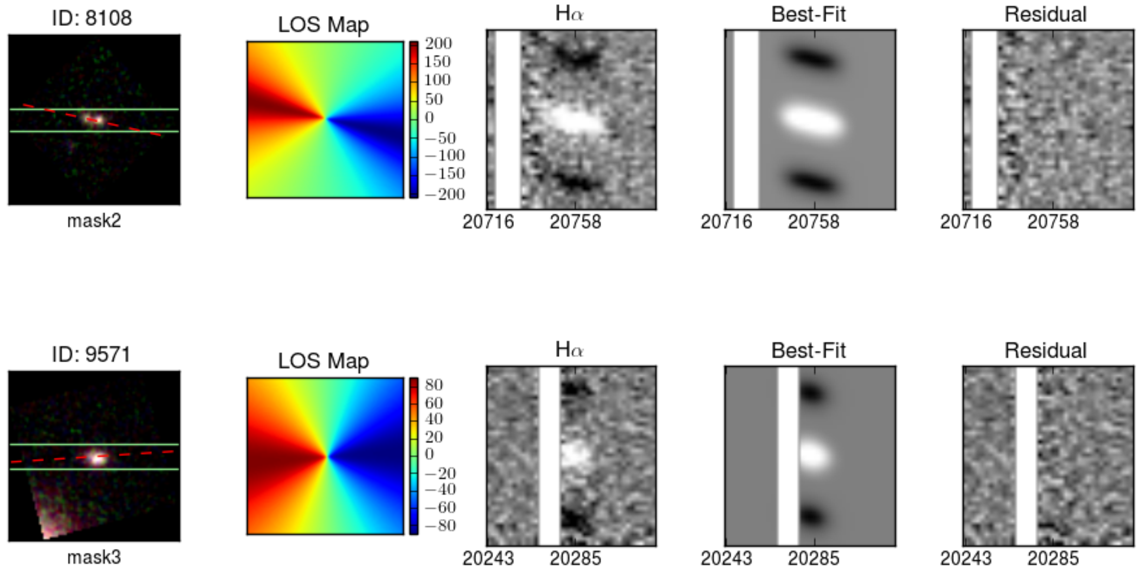

Figure A.2 Continued. Reproduced by permission of the AAS.

APPENDIX B

FITTING SIMULATED EMISSION LINES

We test our fitting procedure on a sample set of simulated MOSFIRE observations. We use 1000 simulated emission lines of galaxies created from the GBKFIT program Bekiaris et al. (2016). Three examples of these simulated emission lines are in Figure B.1.

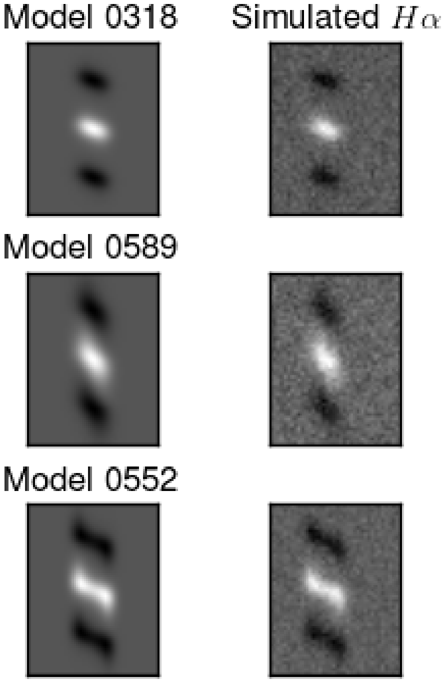

Figure B.1: Examples of models used in our model library. Left column: Models from GBKFIT with 1.25″ dither patter. Right column: Models with low MOSFIRE-level sky noise added, with no sky emission. These are examples of our simulated observations, used to test the effectiveness of our method. Reproduced by permission of the AAS.

GBKFIT creates simulated 3D data cubes of galaxies given initial properties such as

---

Reprinted with permission from "ZFIRE: 3D Modeling of Rotation, Dispersion, and Angular Momentum of Star-Forming Galaxies at $z \sim 2$" by Alcorn, L., et al., 2018, *The Astrophysical Journal*, Volume 858, Article 47, Copyright 2018 American Astronomical Society.

galaxy redshift (z), scale length r_s (1-5 kpc), turnover radius r_t ($\frac{r_s}{3}$), turnover velocity V_t (100-400 km s^{-1}), gas sigma σ_g (20-100 km s^{-1}), inclination i (0-90^o), and offset from the PA of the slit $\Delta\alpha$ (-45-45^o). Galaxies are all infinitely thin exponential disks with arctangent rotation curves,

$$V_{rot}(r) = \frac{2}{\pi} V_t \, arctan \frac{r}{r_t}. \tag{B.1}$$

All objects have a constant intrinsic gas velocity dispersion. These models are convolved with the desired seeing and projected through a 0.7$''$ wide slit. In this case, we used 2D Moffat at 0.7$''$ seeing and $\beta = 2.5$. The values of these properties in our sample span the range of possible values in all cases, providing a diverse sample of disk galaxies, with $\frac{v}{\sigma} = 1 - 20$.

We measure pixel-to-pixel RMS from 2D MOSFIRE K-band observations and add simulated sky noise to each model (Figure B.1). We do not simulate a continuum. Scale models to the sky noise to create mock observations at varying signal-to-noise (SNR) values (from SNR=5-60). If part of the line is masked from simulated sky emission, the SNR drops depending on the amount of line coverage. The SNR was calculated by summing all pixels of the spectrum within defined limits and dividing by the summed squares of the equivalent pixels in the corresponding noise spectrum. This region was defined as within $5r_s$ and 1.26$''$ of the center of the object, and within $3FWHM$ of the emission line.

B.1 The Effects of SNR and Masking Sky Emission

When masking sky emission, we do not perform any operations on masked pixels. The fraction of pixels masked does affect recovery rates of our input models, and through our simulations we have found that if more than half of the emission line is masked at any SNR, we underestimate our input $V_{2.2}$ by 12% at half masked to 83% at 80 - 100% masked (Figure B.2, Row 2, far right). Similar results are found in σ_g recovery: at 50% masked, we tend to overestimate σ_g by 20%, increasing to up to 70% overestimated at 80 - 100% masked (Figure B.2, Row 4, far right). SNR correlates with recovery as well, although less significantly. At

SNR > 10, we overestimate $V_{2.2}$ by $\sim 10\%$ at a 20% scatter, and at lower SNR we find the scatter to increase to $\sim 70\%$ (Figure B.2, Row 1, far right). For σ_g recovery, we find at SNR > 10, we tend to underestimate σ_g by 10% at a scatter of 15%, and at lower SNR the scatter can increase to $\sim$70% (Figure B.2, Row 3, far right).

B.2 Fixed and Free Turnover Radius

The recovery of r_t is significant in the recovery of rotational velocity, as V_t is correlated with r_t. However, $V_{2.2}$ is a more reliable measurement due to a smaller offset from predicted. Similar surveys fix r_t in comparison to r_s e.g. $r_t = 0.4r_s$ Price et al. (2016). We have decided our final sample will not hold r_t fixed, and instead will allow r_t to free values where $r_t < r_s$. However we include results if we fix $r_t = 0.33r_s$ and $r_t = 0.4r_s$ in our analysis.

In the case where we allow r_t to vary freely at any length below r_s, we find we overestimate r_t by around 30% of the input with a large scatter, while recovering our input r_s to a median offset of -20% of the input, and within a 1σ scatter of 15% of the input value. However we tend to overestimate our velocity at $r = 2.2r_s$, to within $\sim$10%. We recover σ_g to a small bias ($\sim$10% underestimated from the input), at a 1σ scatter of 15%, increasing to 70% scatter at high line coverage and low SNR. Therefore, if we have bias in our results, we are overestimating the velocities in the M$_\star$-TFR and in $V_{2.2}/\sigma_g$. We also determine our ability to recover specific angular momentum, j_{disk} (underestimated by only $\sim$5% at low line coverage) and $V_{2.2}/\sigma_g$ (overestimated by 25% at low line coverage). Interestingly, the rotational velocity and the velocity dispersion are both recovered well below $r_s < 0.2''$. The size (both r_s and r_t) of the modeled galaxy seems to be uncorrelated with the recovery rate, possibly because all our modeled galaxies are smaller than the seeing they are convolved to.

In our simulated observations from GBKFIT, r_t is constantly held to be $r_s = 3r_t$. To determine our ability to recover the velocity, we try holding r_t to be at this fixed distance relative to r_s. When we recover our kinematic parameters while holding $r_t = 1/3r_s$, we find that we underestimate both r_t and r_s, but $V_{2.2}$ is recovered with only minor offsets (overestimated by $\sim$5% with a scatter of $\sim$20% at low line coverage). σ_g is still recovered

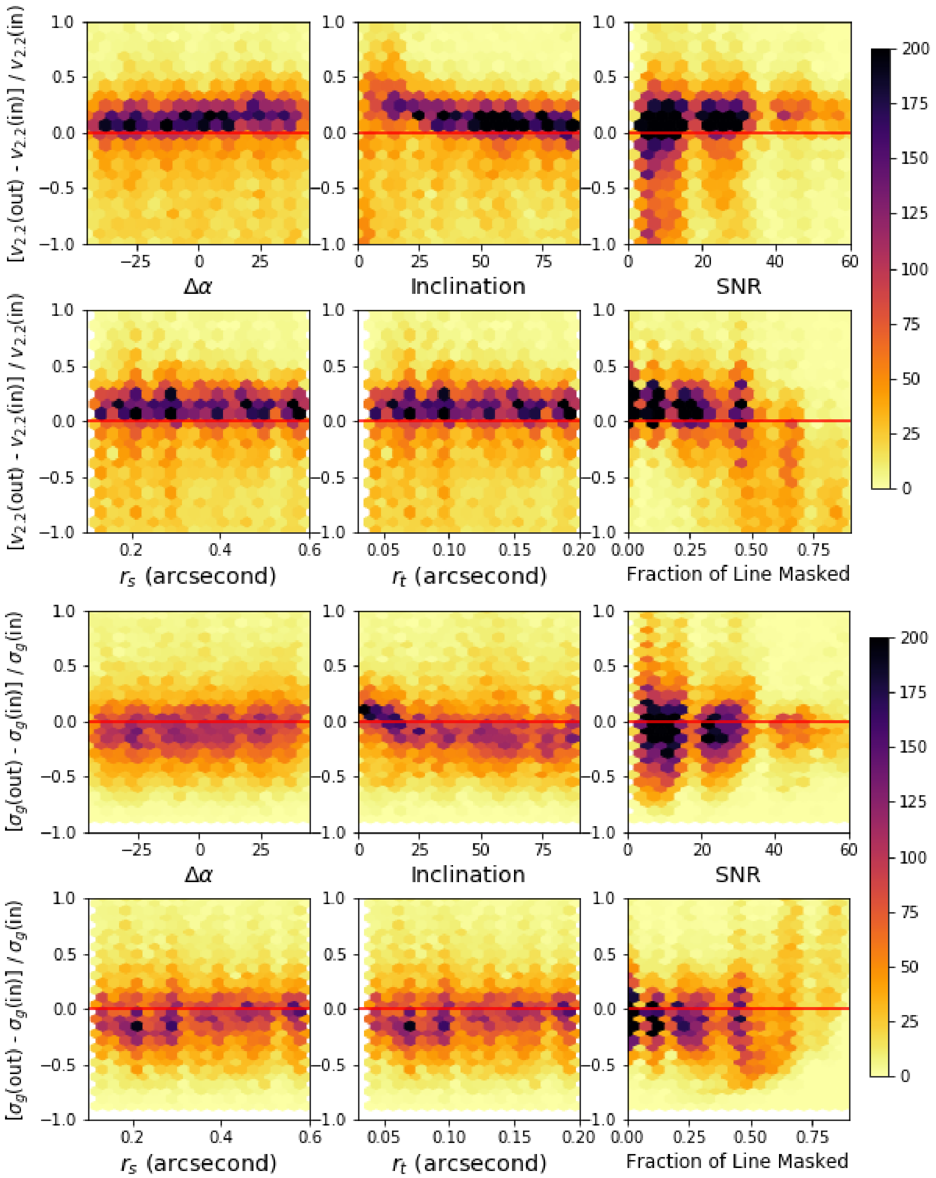

Figure B.2: Recovery rates of $V_{2.2}$ and σ_g for simulated MOSFIRE observations at varying SNR and portion of the emission line masked (due to sky emission). Simulations are emission line models generated by GBKFIT, and embedded in MOSFIRE-level sky noise. Using HELA modeling, we test our recovery rate against (from left, top row) $\Delta\alpha$ (slit and morphological PA offset), inclination, SNR, (from left, bottom row) r_s (disk scale radius), r_t (turnover radius), and emission line masked fraction. All 2D histograms are plotted on the same color scale. We tend to overestimate $V_{2.2}$ by $\sim$10%, and underestimate σ_g by 10%. Inclination tends to have an effect at an inclination of 30^o, where we begin overestimating our $V_{2.2}$ by up to 30%. At more than half the emission line masked, our recovery is unreliable. Reproduced by permission of the AAS.

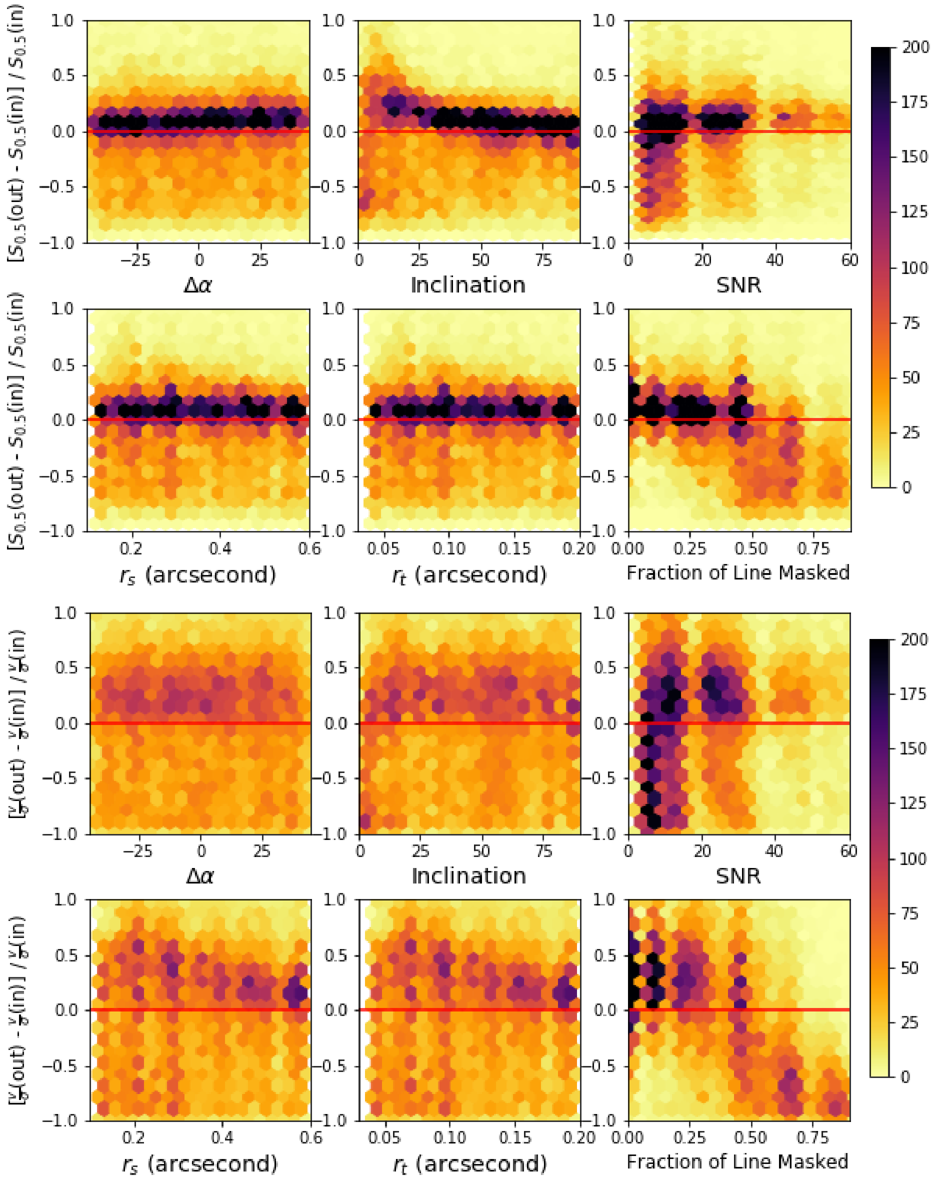

Figure B.3: Recovery rates of $S_{0.5}$ and $V_{2.2}/\sigma_g$ for simulated MOSFIRE observations. Top: We overestimate $S_{0.5}$ by within 10% of the input values. Inclination affects recovery starting at around 30^o, where we begin overestimating $S_{0.5}$ by 20%. Bottom: $V_{2.2}/\sigma_g$ recovery is less reliable, where we tend to overestimate our values at around 25% of our input value with significant scatter. These results indicate that the $S_{0.5}$ parameter is by far the more reliable method of measuring kinematics, and $V_{2.2}/\sigma_g$ values are possibly biased too high and at high scatter. Reproduced by permission of the AAS.

at minor offsets (underestimated by 5%). j_{disk} is underestimated by 10% and $V_{2.2}/\sigma_g$ is overestimated by 25%. We find that we can reliably recover $V_{2.2}$ and σ_g at small offsets, as

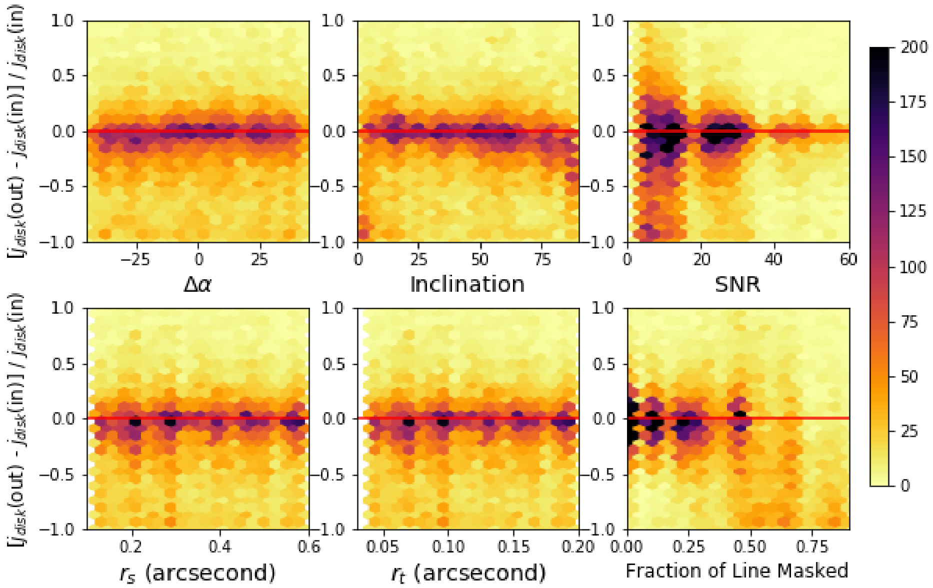

Figure B.4: Recovery rate of j_{disk} for simulated MOSFIRE observations. We can reliably recover input j_{disk} for objects with less than 50% of the line masked, or with SNR>10. Reproduced by permission of the AAS.

well as $S_{0.5}$ and j_{disk}. However, due to the small scatter in the recovered values for $V_{2.2}$ and σ_g, our $V_{2.2}/\sigma_g$ values have high scatter and are overestimated, and are thus likely unreliable.